FRACTURE TOUGHENING AND SELF-HEALING OF COMPOSITE LAMINATES BY NANOFIBROUS MATS INTERLEAVING

Presentata da: **Tommaso Maria Brugo**

Coordinatore Dottorato

Prof. Nicolò Cavina

Relatore

Prof. Andrea Zucchelli

Correlatore

Prof. Giangiacomo Minak

Dot. Chiara Gualandi

Contents

Contents

1 Introduction to composite materials

1.1 Composite materials

The earliest man-made concept of composite material dates back to the Neolithic era, when clay reinforced by straw was used for making walls and bricks. The individual constituents were not useful by themselves but they did when put together. It is argued that the straw helps to keep the clay together and contrast the crack propagation, by reducing the tension at the crack tip [1]. Moreover, the cyclic changes of the ambient humidity induce the subsequent dissolution and re-precipitation of the clay in the micro-cracks, which promote the healing process of the clay-straw composite.

Currently, a composite material refers to a system made of two or more materials combined at a macroscopic level and not soluble in each other's, whose resulting mechanical and physical properties are designed to be superior to those of their individual constituents. A specific class of composite materials, traditionally used in aerospace applications, are fiber-reinforced plastics (FRP). They are, obtained by combining high stiff and strong fibers (∅ = 7-20 μm) called reinforcement, with a weaker polymeric matrix (Fig 1-1). The matrix surrounding the fibers bind them together and allow to transmit the load between them, while the reinforcement imparts its superior and physical properties to the matrix. Fibers are usually made of carbon, Kevlar or glass and can be short or continuous. The matrix can be a thermoset resin or thermoplastic such as epoxy and PEEK. When the application requires maximum performance, fibers are continuous and oriented in specific directions to constitute a lamina or ply (0.1-1 mm thick). The laminas are then stacked one above the other and oriented in different directions as a function of the load that it has to carry, to form a laminated structure.
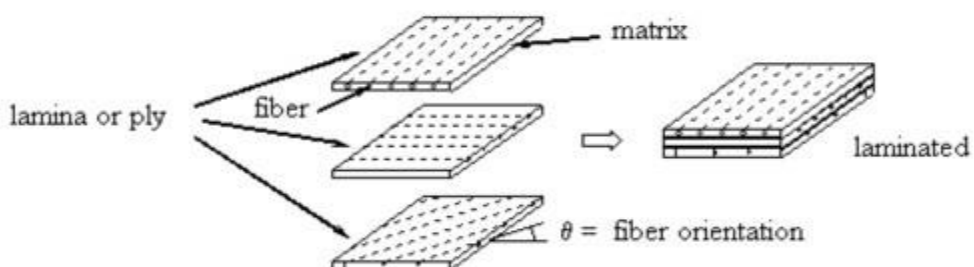
Fig 1-1 Hierarchical structure of a composite laminates. Adapted from ref. [2].

In the analysis of fiber reinforced laminates, when one is analyzing the single lamina, the fibers and the matrix are considered as individual constituents; then when analyzing the entire laminate, the lamina is considered as a continuous constituent. Hence according to Lakes [3], FRP laminates have two structural hierarchical levels: the fiber and the matrix defined at the micron length scale and the laminas defined at the sub-millimeter one.

In nature too, several examples of composite materials can be found, with high order of structural hierarchy that increase their mechanical performance. For example, wood is a composite material with four levels of hierarchical structures: molecular, fibrillar, cellular and macroscopic structure (see Fig 1-2). The fundamental constituent of wood is cellulose, a high molecular weight polysaccharide with linear chain, characterized by high stiffness and strength. Cellulose molecules are combined into an elementary microfibril ($\emptyset \approx$ 10-20 ηm) that are then bundled to form a macrofibril ($\emptyset \approx$ 0.4 µm). The stiff cellulose macrofibrill embedded into a soft matrix of hemicellulose and lignin constitute the fiber composite wall of the wood cell ($\emptyset \approx$ 10-20 µm); which has an hallow tube shape with the axis parallel to the trunk one [4]. The cell wall consists of several layers (S1, S2, ...) with different macrofibril angle orientations; where S2 is the thickest one and has the fiber almost parallel to the trunk axis. Groups of alternate layers of thin-thick walled cells are alternated in the radial direction of the trunk to form the growth rings. The hierarchical structure and the optimized reinforcement orientation of cellulose molecules fibrils, confer to the wood an incredible high specific strength (comparable to the medium carbon steel one) [5], despite the low mechanical properties of its basic biological constituent phase (polysaccharide).
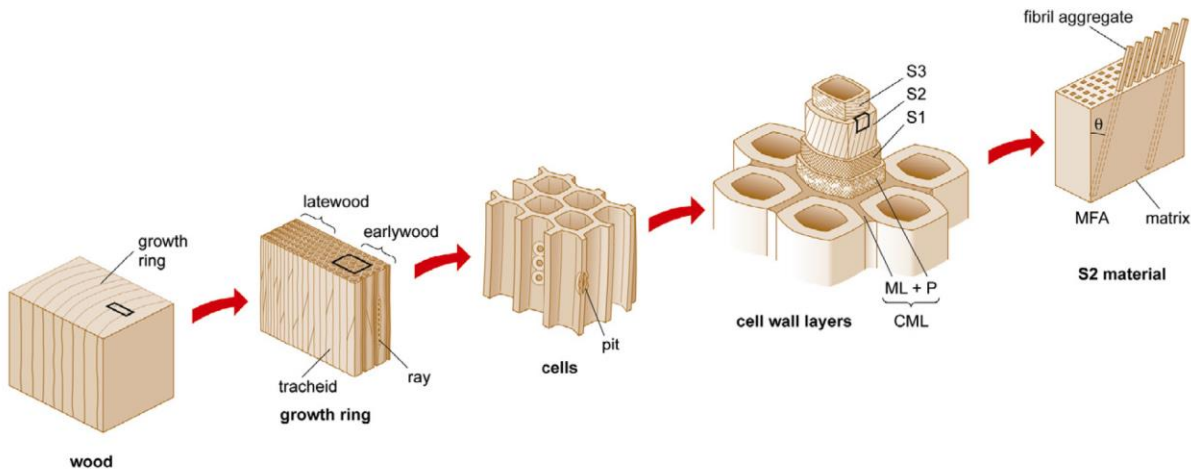
Fig 1-2 Hierarchical structure of spruce wood, reproduced from Ref. [6], with permission from Elsevier.

1.1.1 Mechanical advantages of composite materials

Monolithic materials cannot always satisfy the demands of today's advanced technologies. Only by combining several materials at different length scales, as nature does, the requested performances can be met. In wind turbines, the power that can be captured is proportional to the area of the rotor. Glass fiber reinforced plastic (GFRP) with high strength to mass ratio can enable larger rotors diameter (to date of 150 m) and at the same time be cost-effective. Lighter blades require less robust turbine and tower components, saving so the cascading costs on the wind turbine and therefore on the energy produced. In the highly competitive airline market, fuel represents the 25% of the overall operating costs [7] and is the leading cause of the carbon emission. Reducing 1 kg of mass can save up to 2600 liters of fuel per year. The use 80% in volume of carbon fiber plastic (CFRP) in the Boeing 787 Dreamliner has made it 20 % more fuel-efficient than its previous version.

In the Ashby diagram of Fig 1-3 the yield strength is plotted against the density for common engineering materials, where dotted parallel guidelines link materials that have the same specific strength (σ/ρ). It is interesting to note that a natural material such as wood can have a specific strength (along the grain) comparable to medium strength aluminum alloys or medium carbon steels. Moreover, carbon fibers reinforced plastic (event with a quasi-isotropic lay-up) are endowed of superior specific strength compared to any other material.
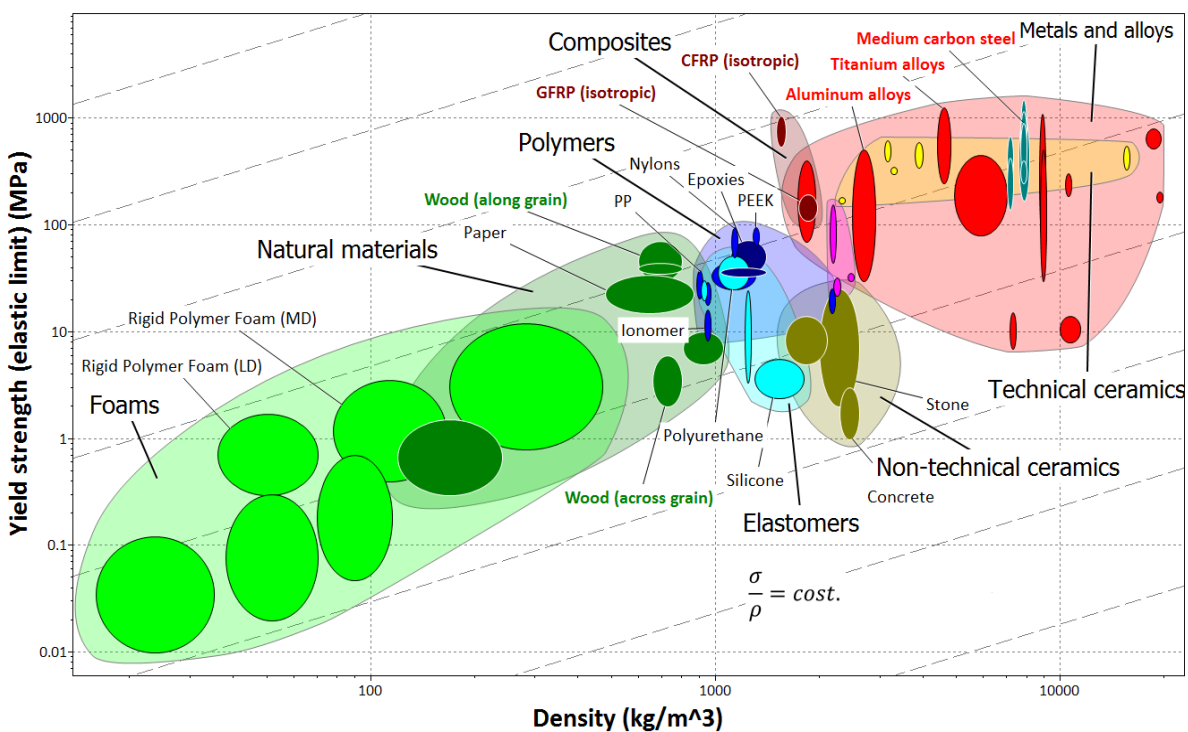
Fig 1-3 Ashby diagram Yield strength vs Density

Values of specific modulus, strength and toughness are given in Table 1-1 for common fiber reinforced plastics and bulk metals. The reported strength refers to yield strength for metals and compression to failure along fiber direction for FRP (the hardest in-plane load condition for composite laminates).

Table 1-1 Specific modulus strength and toughness for common fiber reinforced composite [8] and bulk metals.

Material	Density (kg/m^3)	Young modulus (GPa)	Tensile strength (MPa)	KIC (MPa* m0.5)	Specific modulus (GPa/ (kg/m3))	Specific strength ((MPa/ (kg/m3))	Specific KIC (MPa *m0.5/ (kg/m3))
Steel (40 NiCrMo 6)	7800	205	1100	100	0.026	0.14	0.013
Aluminum (7075-T6)	2600	72	500	30	0.028	0.19	0.012
Titanium (T6-Al-4V)	4400	120	900	70	0.027	0.20	0.016
Epoxy	1200	4	80	1.5	0.003	0.07	0.001
Glass fiber (E-glass)	2500	72	3500		0.029	1.40	
UD glass/epoxy	1800	42	900	10	0.023	0.50	0.006
Cross-ply glass/epoxy	1800	20	550	10	0.011	0.31	0.006
Aramid fiber (Kevlar 49)	1500	130	3800		0.087	2.53	
UD aramid/epoxy	1400	75	350	10	0.054	0.25	0.006
Cross-ply aramid/epoxy	1400	31	250	10	0.022	0.18	0.006
Graphite fiber (PAN)	1800	230	3400		0.128	1.89	
UD graphite/epoxy	1600	140	1600	10	0.088	1.00	0.006
Cross-ply graph/epoxy	1600	75	800	10	0.047	0.50	0.006

A visual representation of the listed features is given in the graph specific strength vs specific modulus of Fig 1-4. Glass, Kevlar and carbon fibers have a specific modulus and strength that is an order of magnitude higher than metals. The major reason of their high strength is their thin diameter (e.g. 7 μm for carbon fibers). Thinner is the diameter and lower are the chance of an inherent flaw in the material and therefore higher is the strength, which is sensible to the flaws [9] . Note how also in this case the structural dimension play a major rule on the strength of the material. However, fibers are not able to carry compressive or bending loads by themselves, while a bulk version of them would be less strength and too fragile. For this reason, fibers are embedded in a polymeric matrix such as epoxy which allows to transmit the load between them.

As consequence, the resulting elastic modulus and strength of the UD composite, along fiber direction, are roughly a weighted average (on volume) of its constituents. These properties are then halved when equal amounts of fibers are disposed at right angle to each other (cross-ply), in order to have a laminate with equal strength in both principal directions. Looking at the table, a structure in CFRP that has to carry loads mostly in one direction can weight up to a forth of a metal equivalent one, while a structure that has to carry loads on different directions can weight up to half of the metal equivalent one.
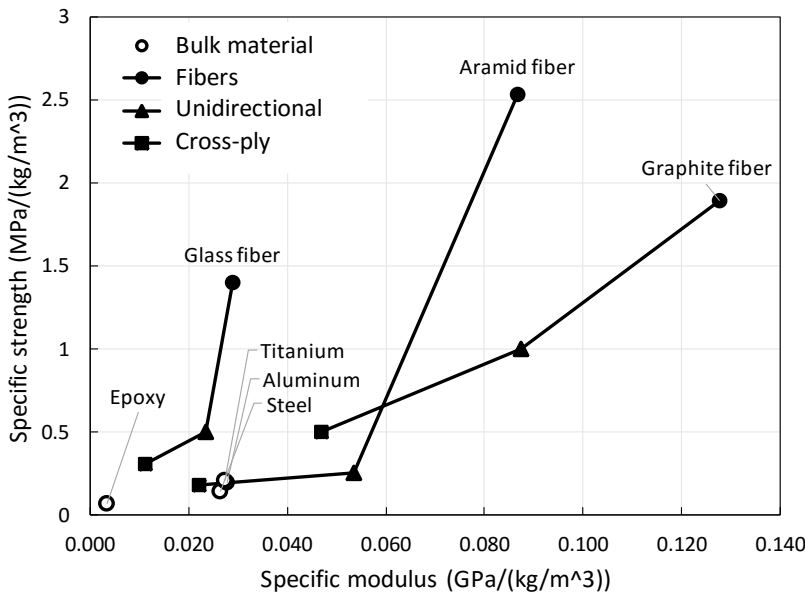
Fig 1-4 Specific Strength vs specific modulus for common FRP laminates and bulk metals.

1.1.2 Drawback of composite materials (Achilles' heel)

In the design of a safety-critical structure, as car chassis and airframes, the strength is not the only key parameter in the choose of a material. Fracture toughness often is more important than strength, to avoid problems of a premature failure of the structure. However, strength and toughness in most artificial common materials are two properties mutually exclusive [10]. Indeed, the ability of a material to undergo plastic deformation hence ductility, which is usually in contrast with its strength, confer to the material fracture toughness by local release of the stress field around the crack tip, that would otherwise cause the failure of the material. For this reason, airframes are manufactured from relative low strength versions of available alloys.

In the Ashby diagram of Fig 1-5 the mode I fracture toughness (G_{IC}) is plotted against the yield strength for composites and metals. It is noted that G_{IC} was estimated from the critical stress intensity factor, $K_{IC}^2 = E \ G_{IC} \ / \ (1-v^2)$ [11] [12], based on the linear elastic fracture mechanics (LEFM) theory. This is an approximate simplification, but the goal here is to have an indicative value for each material in order to be able to compare them.

Clearly the fracture toughness for composite laminates is low compared to metals and to their high strength (especially for CFRP can be an order of magnitude lower). The major cause is the brittleness of the high crosslinked epoxy resin. It can be noticed that the thermoplastic polymers (not crosslinked) can have a fracture toughness up to one order of magnitude higher than the epoxy thermoset ones (crosslinked). Elastomer can even have a higher fracture toughness than thermoplastics. However, for the use as matrix in composites, thermoplastic polymers and elastomers present some disadvantages, compared to thermoset one, as low stiffness, strength, processibility and hygro-thermal stability (which will be elucidated in paragraph 1.3.1).

The low fracture toughness of composite materials, force to keep a high safety factor and over-dimensioning the structure, thus limiting their full weight-reduction potential. Therefore, in the development of composite materials, it is crucial to increase the fracture toughness which limit the full exploitation of its extremely high specific strength. But, to improve this feature, it is first necessary understanding the complex mechanism of fracture which induces these special materials to failure.

The author wishes to point out that the scope of the following paragraph is to give only a general overview on the damage mechanisms in composite materials and highlight the critical issues in which effort should be put to increase their service life.
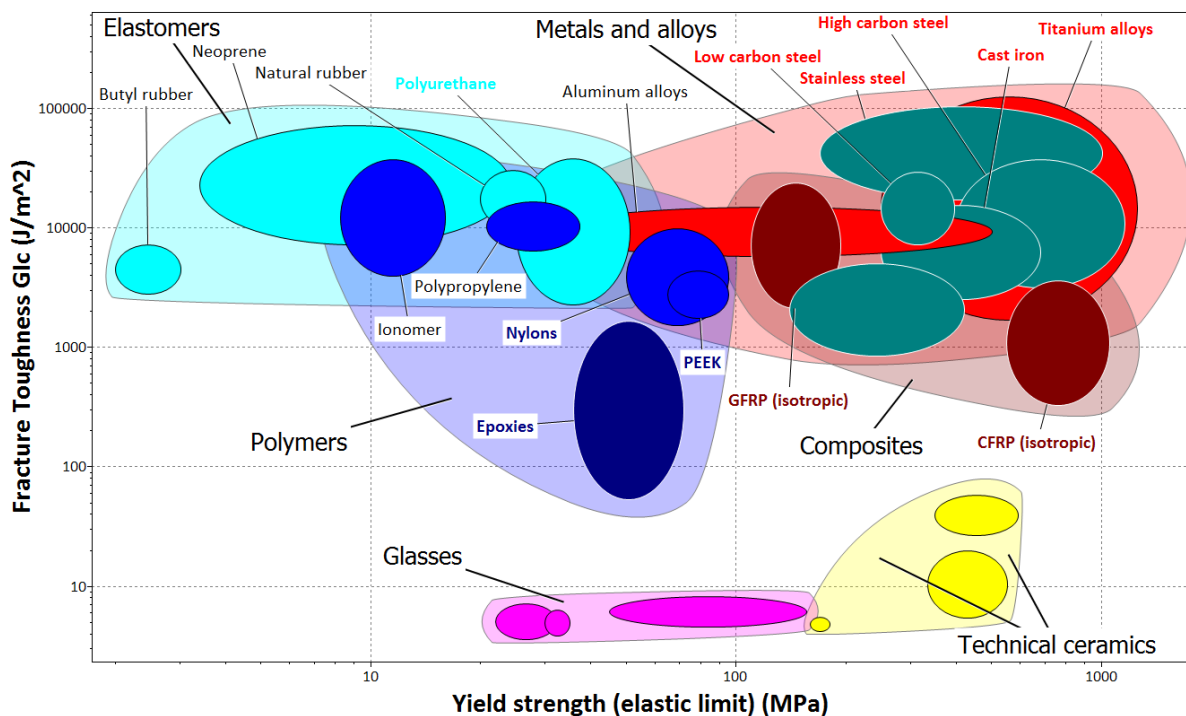
Fig 1-5 Ashby diagram Fracture toughness (GIc) vs Yield strength.

1.2   Damage mechanism in composite laminates

Final failure of composite laminates is generally preceded by unstable delamination propagation. Delamination is the separation of laminas (or plies), caused by the stress state developed between one ply and the adjacent one (interlaminar stress) and it may be induced by different mechanism/load conditions during service life of composite structures:

- free-edge effect
- fatigue loading
- impact (out-of-plane load)

1.2.1   Free edge effect

Composite laminates which are made of anisotropic plies that terminate at common edges, locally generate highly tree-dimensional stress states which induce interlaminar stresses that are sufficiently high to cause interlaminar failure (delamination) at those locations [13].

Consider the following specific problem in which a prismatic [±45°]s laminate having free edges at y=±b is loaded by uniaxial strain ε_x on its x ends. In Fig 1-6 it's plotted the stress state at ±45° interface as a function of the normalized distance from the laminate centerline, evaluated by finite difference analysis by Pipes et al [14].

Note that the planar stress distribution (σ_x, σ_x, τ_{xy}) predicted by classical lamination theory is distorted by the presence of free edges (not constant). But more important, note how the interlaminar shear stress τ_{xz} from zero at y/b=0.5 grows asymptotically and becomes singular at the free edge. This stress singularity is responsible of the delamination onset at the free edge and will load the growing crack in mode III. Different stacking sequences can cause different stress states at the free edges plies interfaces and load the induced cracks in different modes. As in the case of a [±25°/90°]s laminate where the normal stress σ_z singularity at the mid-plane loads the crack in mode I.

Edge delamination is common in engineering structure, not only at the termination of the geometry of a given component but also in many different design discontinues such as holes, tapered laminates and bonded joints (see Fig 1-7).
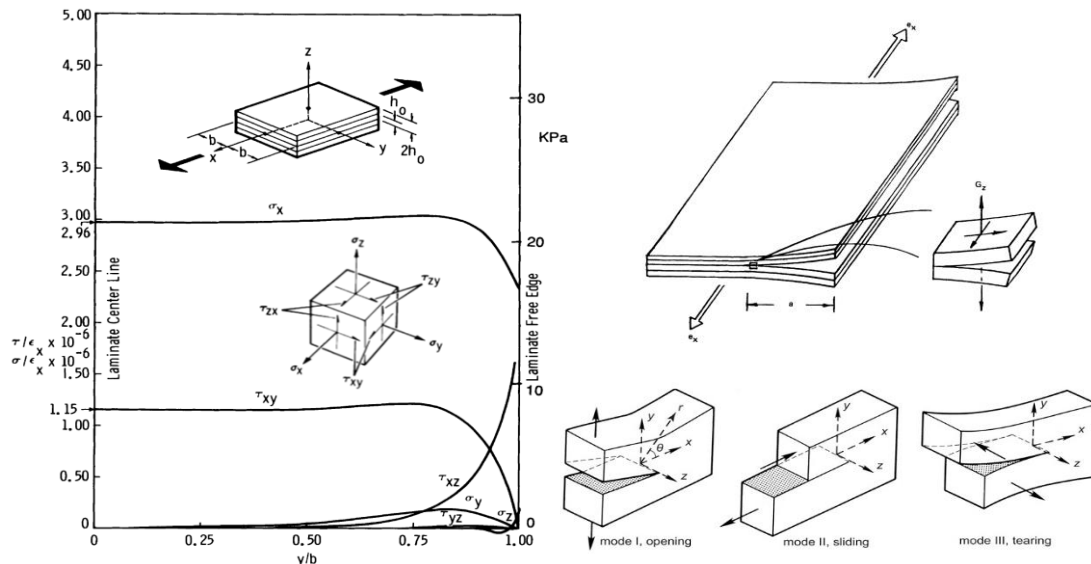
Fig 1-6 a) distribution of the interlaminar stress state at the ±45 interface, as function of the normalized distance from the centerline of a [±45°]s laminate, reproduced from Ref. [14]. b) Mode of delamination.
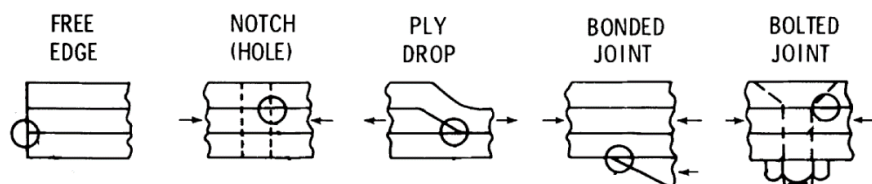
Fig 1-7 Design discontinuities source of delamination. Reprinted from Ref. [15], with permission from Elsevier.

7

1.2.2 Fatigue loading

The damage degradation in composite laminates under fatigue loading is a complex process that evolves on different length scales. It can be overviewed with the aid of Fig 1-8, which traces the damage process as a function of percentage of life (relative to the number of cycles to failure) for a composite which contains 0 plies (fibers oriented with the loading axis) and off-axis loading plies, subjected to tensile cyclic loading. It must be mentioned that, if free-edge effect is not predominant, similar damage development mechanism can also occur on multi-axis laminates subjected to monotonic tensile load.
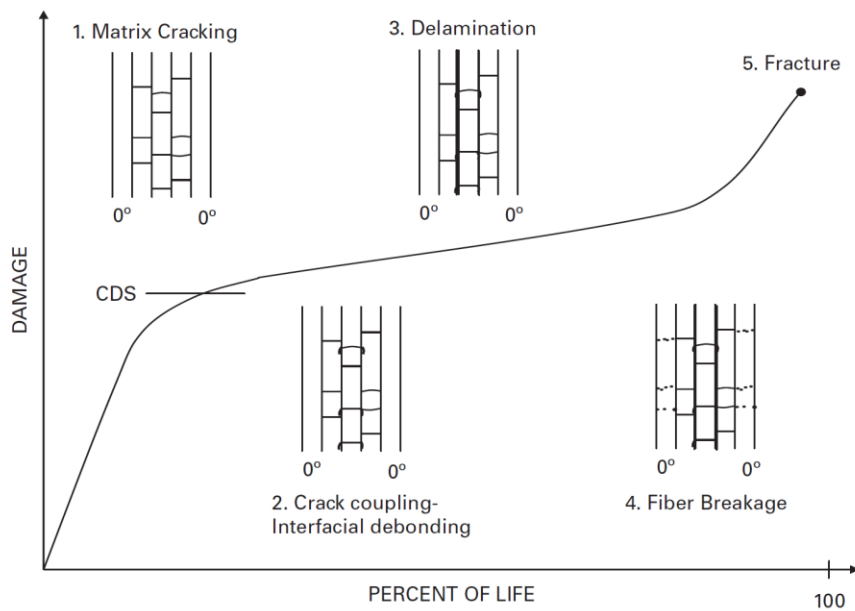
Fig 1-8 Progressive damage development for composite laminates subjected to fatigue loading. Reproduced from Ref.[16], with permission from Cambridge University Press.

The damage process can be subdivided in three stages [17]:

Stage I occurs during the first 10-15% of life, during which damage develops at a very rapid rate. The major damage mode during Stage I is matrix cracking. Primary cracks usually form through the thickness of the off-axis load plies in a direction parallel to the fibers (marked in figure), when the global laminate strain exceed the strain sufficient to cause failure of the matrix phase or separation between fiber and the matrix at the interface (Fig 1-9a).

Throughout stage I, number and density of matrix cracks increases until a uniform saturation spacing is reached. Further onset (initiation) of matrix cracks is inhibited by the local stress release, caused by the existing cracks, which avoid the formation of other cracks in their proximity. While, the grows of the single matrix cracks (propagation) throw the thickness of the laminate stops at the interfaces between plies with different fiber orientation. Although the ply is damaged locally, it does remain effective in the laminate by providing strength and stiffness in the direction of the fibers [18].

8

The reduction in laminate stiffness caused by primary matrix crack formation in common laminates is usually small, about 10% and is generally tolerated in the design of an engineering structure.

Stage II represents most of the entire fatigue life time (70-80%), during which damage initiate and grows at slower rate. Matrix cracks, which in the previous stage were stopped at the plies interfaces, start to turn and growing along them (Fig 1-9 b). Crack coupling produce debonding of adjacent plies, hence delamination, which at this stage is still confined near the edges of the laminate or at a design discontinuity (e.g. hole), see Fig 1-7a & c. The onset of the delamination can also occur internally where primary cracks (in 90° plies) crosses secondary cracks (in 0° plies), the latter generated by the stress field developed at the primary matrix crack tip (see Fig 1-10). The remainder of the Stage 2 consists of the initiation and growth of delamination, but it is still localized.

Stage III represents the final 10-15 % of life and is characterized by an exponential increase of the damage rate caused by delamination growth, coalescence and consistent fiber brakeage. Under cyclic tensile loads, laminate failure is coincident with the catastrophic fracture of the major loadbearing plies. While under cyclic compressive loads, failure is usually due to local buckling of the delaminated plies.

It has to be mentioned, that under cyclic loading, fibers fracture occurs during all three stages of fatigue life. However, during stage I and II the amount of fractured fibers is still limited and localized.
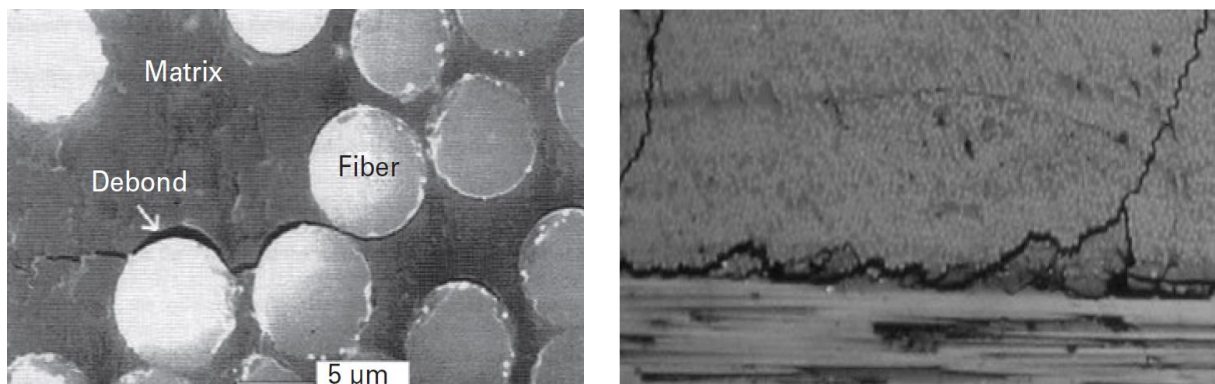
Fig 1-9 Matrix crack initiation from fiber debonds (a) and Interlaminar delamination crack formed due to joining of two adjacent matrix cracks in a fiber-reinforced composite laminate. Reproduced from Ref.[16], with permission from Cambridge University Press.
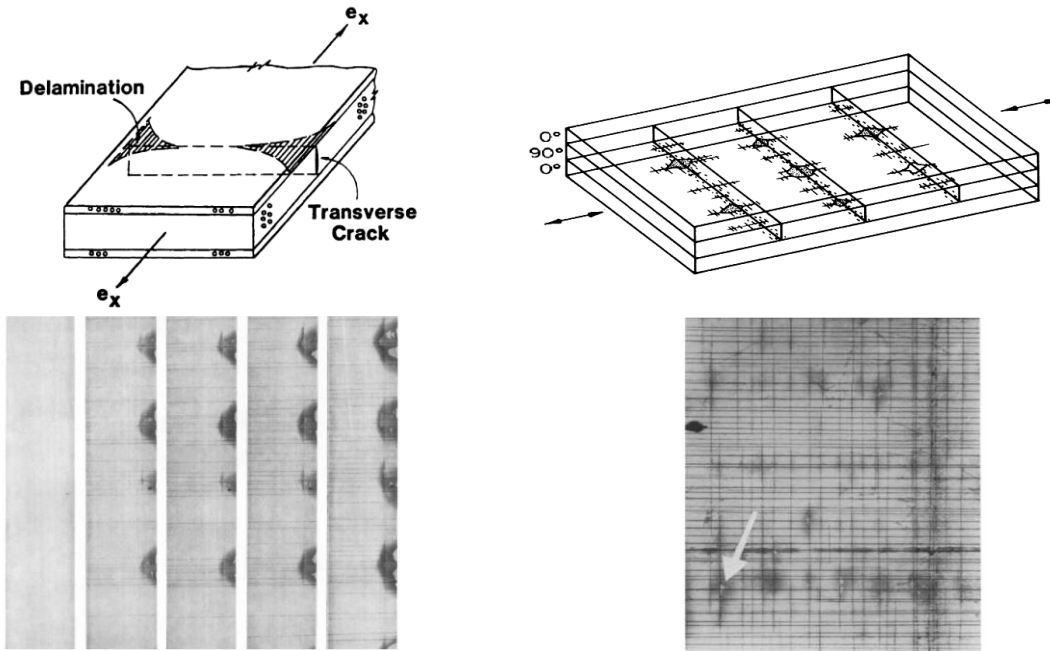
Fig 1-10 Delamination onset at free edges caused by growing transverse (primary) matrix cracks in a [02/903]s laminate under progressive quasi static tensile load: illustrative sketch (fig a) and plane view x-radiography (fig. c) Delamination onset at primary and secondary matrix crossing under tensile fatigue loading : illustrative sketch in a (fig. b) and x-radiography (fig. d). Reprinted from Ref. [17], [13], with permission from Elsevier.

1.2.3   Low velocity impact (out-of-plane load)

Composite structures, in addition to conventional in-plane loads (whose damage mechanism has been described above), may be subjected to out-of-plane loads, as impact. This section deals with the damage caused by low-velocity impacts, in which the projectile is rigid and the velocity are in the range of few tens m/s. Low velocity impact, on multiaxial UD laminate, induces in the composite three types of damage: matrix crack, fiber fracture and delamination. The damage development in the composite depends on its thickness. In Fig 1-11 it is described the damage mechanism, for thick laminates, in which the bending stresses are low relative to the contact stress.
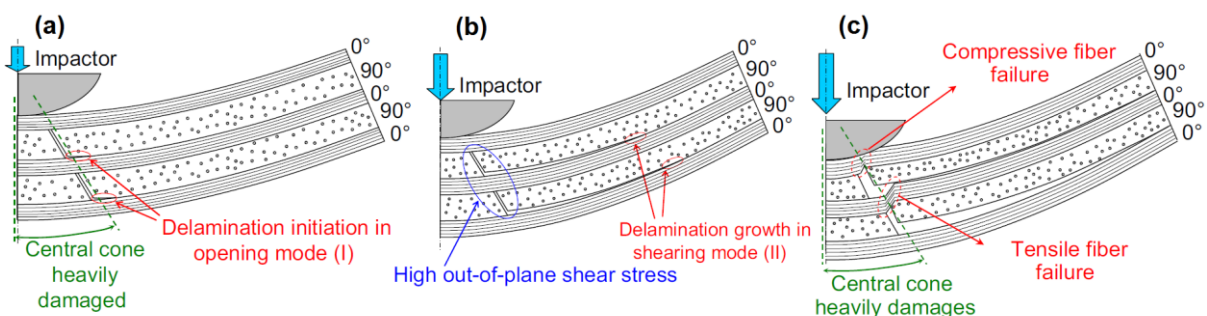
Fig 1-11 Evolution of the damage caused by low-velocity impact as a function of the growing impact energy level, for thick laminates. Adapted from ref. [19].

10

Each figure represents the evolving of the damage as a function of the growing impact energy [19]:

(a) At low energy first matrix cracks are created (with 45°slope) under the impactor due to the high out-of-plane shear stress developed in this zone. Once the cracks reach the lower interface induce opening, shearing and tearing forces (mode I, II and III respectively) which causes delamination. Delamination in turns induce matrix cracking in the adjacent plies with a pine tree shape [20].

(b) Once created, delamination propagates at the plies interfaces due to the interlaminar out-of-plane shear stress, especially along the fibers directions of the lower plies.

(c) When the impact energy level increases, fiber fails due to the compressive force (under the impactor) and tensile one (in the mid or lower thickness). Generally, the lowest ply does not brake due to fiber breakage because the high delamination in this zone tends to unload it.

For thin laminates the damage development is different. Bending stresses are predominant and cause tensile failure of the bottom plies in transverse direction respect to the fiber one. The damaged ply induces then delamination of the first interface, which then induce matrix cracking of the next ply. The matrix cracking-delamination mechanism propagates from the bottom to the top with a reversed pine-tree pattern [21].

Note that after impactor unloading, matrix cracks and delamination remains partially open due to the resin and fiber debris, which prevent their closure.

1.2.4   Dichotomic role of the hierarchical structure on the toughness of composite materials

It must be emphasized, how in the complex damage mechanism of composite laminates described above, the hierarchical structure plays a dichotomic role [18]. Inhomogeneity (namely the fiber and matrix phases) and anisotropy (namely the orthotropic ply structure) are the cause of the initiation of the damage at different length scales. The Inhomogeneity is the cause of the onset of the damage at micrometer scale, caused by the non-uniform stress localization and concentration, which are caused by the mismatch of the mechanical proprieties of the two phases. Examples can be found in fiber matrix debonding end matrix cracking during cyclic loading or impact (Fig 1-9). While the anisotropy of different plies induces interlaminar stresses at the sub-millimeter-scale, which cause the onset of the delamination (i.e. free edge effect).

However, at the same time the hierarchical structure constitute a barrier for the growth of the cracks. The inhomogeneity, hence the fibers oriented in different direction in each ply, stop the matrix cracks propagation from one ply to the adjacent one. Moreover, the anisotropy, hence the different orientation of the plies help to keep them together even if they are cracked. This behavior is observed in laminate cross sections of composites stressed by cyclic loading or impact, where cracks are stopped or divert at the interfaces (Fig 1-9 b).

Hence, it can be concluded that the hierarchical structure in composite laminate is the greatest contributor factor of damage onset: crack initiation and delamination at micro and submillimeter scale, respectively. But at the same time, it is the key factor of the superior resistance to crack grow (matrix cracks), which is the main contributor to fatigue resistance of composite materials [18].

Similar crack anisotropic behavior can be found in wood. Where, shear cracks can easily propagate parallel to the wood cell, without being broken through; while its perpendicular propagation is very difficult as the braking of the wood cell is stopped by the cellulose microfibril in the secondary wall cell (S2) [5],[22].

On the contrary, homogeneous materials are more resistant to crack initiation, which is caused by stress concentration, because of the absence of two separated phases with mismatching mechanical properties. But are relatively less resistant to crack propagation because they do not have barriers (different phases) to confine its propagation. Therefore, their fatigue failure can occur by the initiation of a single crack.

1.2.5 Damage intolerance vs damage tolerance:

Usually in the design of a safety structure, the presence of defects is not tolerated and the structure is considered no longer reliable when the first crack onset occurs (damage intolerance). This force to keep a high safety factor during the design which leads to a dramatic increase of the weight of the structure.

Another approach in the design of a safety structure, is based on the assumption that flaws can exist in the structure and can propagate with usage (damage tolerant). This design method, commonly used in aerospace engineering, is based on fracture mechanics principles (e.g Paris law) in which a crack can onset. Then under cyclic loading slowly grows up it reaches a critical size for then propagate unstably. Therefore, the life span of the structure can be limited by the critical size that the flaws can reach and not by their onset. This allows to keep a lower safety factor and therefore reduce the weight of the structure. It should be noted that in order to keep a high safety standard the structure must be subjected to maintenance programs to detect and measure the dimensions of the defects and repair them if necessary.

The damage tolerance approach suits perfectly for composite structures in which, as seen previously, matrix cracks arise in the early life stage, but then its propagation is hindered by the hierarchical structure for most of its life span. The damage size reaches a critical size when the matrix cracks turn in delamination and its propagation ca not be hindered anymore. For this reason, in the last decades, many attempts were done in order to reduce and hinder the delamination propagation.

1.3   Critical issues and routes to increase service life of composite materials

The damage type in composite materials, whether is it caused by free edges, fatigue or impact can be classified in three main categories: matrix cracking, delamination and fiber failure. Each one affects a different phase or structural level, but they are strongly interconnected by cause and consequence. Below, the damage types are listed by growing order of severity and time event in the damage evolution of composite laminates:

Matrix cracks parallel to the fiber direction and fiber-matrix debonding are often the first damage to occur (except if free edge effect is predominant). It initiates, propagates and multiplies in number, through the thickness of the single plies (*intralaminar damage*). Usually matrix cracks are tolerated during the service life of a composite structure because they are confined by the hierarchical ply structure of the laminate. Indeed, a composite stressed by cyclic loading sustain up to 90% of its entire service life with matrix cracks already formed. However, matrix cracks, which at the beginning are confined in the single plies, beyond a certain level of static in/out-of-plane load or number of cycles, start to turn and to propagate through the interfaces, triggering the debonding of the plies.

Debonding of the plies, hence **delamination** (*interlaminar damage*), which can be induced by matrix cracks or free edges stress concentration, can easily propagate through the matrix interfaces because there are no other phases or structural hierarchical levels to hinder its propagation. Local and isolated delamination, stressed by static o cyclic loading, can grow and marge, leading to a local separation of the single plies. Once plies are separated the laminate can fails (despite the fibers are undamaged) because it cannot bear anymore bending loads (due to the reduction of the moment of inertia) or compressive loads (due to the local buckling of the plies).

Fiber failure occurs during the entire service life of the composite, but usually at the beginning its number is irrelevant for the integrity of the laminate. Some failures are random fractures of statistically weak fibers. Some others fiber breakage are caused by the stress concentration at the matrix crack tips, which are highly localized in the high stress zone around the matrix crack tip [18]. While extensive fiber breakage occurs, for in plane loads, when large delamination's (which can be also induced by impact loads) reduce the integrity and increase instability of the laminate [16]. Extensive fiber breakage is the worst scenario because has a detrimental effect on the residual strength of the laminate and anticipate the imminent failure of the structure

Therefore, fiber breakage is the most detrimental effect for the service life of the composite and for this reason many attempts were made in the last few decades in order to increase their strength [23]. However extensive fiber breakage is only the last failure mode to occur and is often preceded and caused by delamination. Moreover, delamination is the direct cause of failure of composite laminates stressed by compressive and banding loads. While matrix cracks seem to be tolerated in the composite up to they do not propagate

towards the interfaces and induce delamination. Hence, delamination is a major cause for concern in composite laminates, since it is key factor of its damage evolution.

In order to solve the delamination issue and therefore increasing the service life of composites, two different approaches have been adopted by the scientific community:

- Interlaminar fracture toughening (preventive)
- Self-healing (curative)

The progress made on these two different routes are briefly described in the next two paragraphs.

1.3.1   Interlaminar fracture toughening (preventive):

Epoxy resin, is the main matrix material used for composite material in aerospace application, because offer high modulus, strength and low creeping, due to its high crosslinked structure. It also has excellent adhesion to glass and carbon fibers. Moreover, it is easy to be implemented in a lamination process (also with complex shapes), because during the process it is in the form of viscous liquid, while its hardening (crosslinking) can be triggered at the need by increasing temperature. Unfortunately, the high cross linking density leads to have a highly brittle material, which makes the composite laminate susceptible to delamination. This, as mentioned before, force to keep a high safety coefficient in the design of a composite structure, thus limiting the full exploitation of its extremely high specific strength. Therefore, since fiber reinforced epoxy laminates have found application, different techniques have been developed in order to increase their delamination resistance. Below are briefly described the main ones, with pros and cons.

Lay-up optimization:

Improvement of the damage tolerance of the composite laminate can be achieved by designing an optimal lay-up which minimize the out-of-plane stresses (see paragraph 1.2.1). Pagano [24] demonstrate that the effect of the interlaminar normal stress in a [±45°/0°/00°]s the effect of interlaminar stresses were reduced considerably by an interchange of the 90° and 0° ply position and increased of 70% the tensile strain to the onset of the delamination. However, the development of a toughened composite has far more potential for minimizing the susceptibility of the delamination and does not impose constrains to the design of the composite laminate.

Through the thickness reinforcement:

Stitching:

To reinforce the laminate through the thickness, the uncured prepreg or the dry fabric are sewed with a strong yarn as carbon, glass or Kevlar. Stitching can improve the fracture toughness in mode I and II up to 15 and 4 times. However, when the stitching needle penetrates in material can induces damage or misalignment of the fibers, which cause

reduction of the in-plane mechanical properties of the laminate (especially at compressive loads) [25].

Z-pinning:

In like manner, Z-pinning reinforce throw the thickness the laminate, by inserting metal pins or cured carbon fiber pins. Also in this case the improvement of interlaminar fracture toughness are quite high (up to 500%) but the in-plane mechanical properties are slightly reduced (in the range of 5-15 %) [26]. Here, the toughening mechanism is quite interesting because acts behind the crack tip by bridging the crack wedge and releasing so the stress at the crack tip. However, as consequence this kind of system can work only once the crack.

<u>*Matrix toughening:*</u>

As mentioned before, the high cross linking density in epoxy resin, unfortunately, leads to have a high brittle material, slightly tougher than inorganic glasses ($G_{IC} \sim 0.1 \div 1$ kJ/m^2), see Fig 1-5. Differently, thermoplastics can be up to an order of magnitude tougher then thermosets, due to the large free volume available between the polymer chains, which can absorb energy generated by the crack grow and blunt the crack tip ($G_{IC} \sim 1 \div 5$ kJ/m^2).

Thermoplastic:

Using thermoplastics as matrix, can increase up to one order of magnitude the interlaminar toughness of composites, compared to conventional epoxy (i.e. PEEK). The drawback, is the increase of complexity in the laminating forming of thermoplastic matrix composite with big dimension or complex shapes, because it needs to be heated (to flow) at high temperature and pressure. This polymers have not been considered in the industry in the past, due to low hygrothermal stability (moisture adsorption), creep problems, interfacial and wetting difficulties with the fibers and lower compressive strength [27]. However, manufacturer recently have made effort to overcome this problem for some special applications.

Rubber toughening:

Another option consists in modifying the epoxy based matrix system by dissolving rubber or a thermoplastic polymer to the uncured epoxy. During curing a phase separation occur which creates finely dispersed, rubber or thermoplastics particles, (~0.1-5 micron) chemically bonded to the epoxy matrix [28]. The result is an incredible improvement of fracture toughness of the bulk resin (up to 25 folds) and a good improvement of the interlaminar fracture energy of the laminate (up to 5 folds). It is found that the poor translation of the resin toughness to the composite is due to the constrain caused by the fibers [29], [30]. The major toughening mechanism was explained as increase of plastic deformation of the matrix, which blunts the crack tip and reduces the local stress concentration. Moreover, the cavitation ahead the crack tip of the rubber particles release the stress and promote higher plastic deformation, while the consequently separation of the epoxy-particles interface dissipates energy [31]. However, the drawbacks of increased fracture toughness are: reduction of the

in-plane mechanical properties due to the elastic modulus decrease (which compromises the stability of the fibers and their load transfer), decrease of Tg (hence maximum temperature use) and substantial increase of water absorption (which in turn degrade the mechanical properties) [28].

Interleaving:

The concept is to add between one ply and the other, of prepreg, a discrete partially cured (like prepreg) layer of very high toughness resin. The key of the interleaving is that the interleaved material has the required viscosity to don't mix with the prepreg resin during the co-curing, remaining a discrete layer. The result is an increase of interlaminar fracture toughness, without affecting the hot/wet compression properties of the laminate because despite the softening of the interleaved zone the resin around the fibers remains hard [28]. However, the tough interleaved layer has low stiffness and strength and is relatively thick (~ couple hundred of microns) and this proportionally reduces the global specific stiffness and strength of the laminate [28].

<u>*Nano-size reinforcements:*</u>

The use of nano particles as reinforcement for composite material has attracted tremendously the scientific community in the last two decades. Mainly because it seems that it does not affect the original in-plane mechanical properties of the laminate. By adding a nonreinforcement, the hierarchical structure of the composite laminate is increased from two to three hierarchical levels: the laminas defined at the sub-millimeter scale, the fiber and the matrix at the micron length scale and the nano-reinforcement at the nanoscale. For this reason, this special class of composite material are often called multiscale composites.

Graphene, Carbon nanotube (CNT) and MWCN:

Graphene has a two-dimensional atomic structure of carbon in which the atoms are bonded together in a sheet form, with a perfect hexagonal pattern. Single walled carbon nanotubes (SWCNTs) often abbreviated as CNTs consists of a single graphene rolled up in to a seamless cylinder with a diameter of 1 nm; whereas multi walled carbon nanotubes (MWCNT's) consist of two or more concentric cylindrical shells of graphene sheets. Graphene based nano-structures presents incredibly high mechanical performance of at least one order of magnitude higher then metals because of their perfect atomic arrangement free of flaws. Therefore, the addition of a so high strength nonreinforcement to the composite laminate is expected to increase its poor out-of-plane mechanical properties. Kim.et.al [32] in 2011 analyze the result on fiber reinforced CNT composites laminates from the available literature. They reported a wide variation on the increase of the interlaminar fracture toughness of CNT reinforced CFRP, ranging from 25 % to 150 % and from 27% to 200% on mode I and II respectively. The wide spread of the results was attributed to process issues in integrating CNT in the composites, caused by difficulty in dispersion of CNT in to the epoxy matrix because they tend to agglomerate due to the strong van der Waals interaction and low adhesion with

the matrix. They concluded that further effort is necessary to improve the process. Daniel R. Bortz et.al [33] tested at static and fatigue loading CNF matrix-reinforced carbon fiber biax ±45 laminates. The increase of static tensile strength was negligible, while the fatigue life for CNT composite was 150% higher than pristine ones. The improvement was attributed to the suppression, by CNT, of the delamination caused by the interlaminar stress concentration at the free-edges. A major concern for the use of CNT and MWCN, rather than the process, it is their still not clear impact on the human health [34]. In United States and Europe the safety and health institutions detailed the potential hazards and recommended an exposure limit for CNF and CNT.

Polymeric nanofiber interleaving:

A relative new approach for the delamination suppression consist in inserting, between one ply and the other one of the laminate a non-woven mat made of continuous polymeric nanofibers. The technique and the different benefits, compared to conventional methods, will be introduced and discussed in the next chapter. Moreover, the fracture toughening mechanism and how different nanofiber interleaving parameters can affect the results on different laminates types will be investigated and discussed in chapters 3,4,5 and 6.

1.3.2   Self-healing (curative)

A different approach to increase service life of composite laminate is to confer them the ability to self-repair in event that the delamination is already occurred but it is still localized.

This approach allows a further step in the design of a structure because the formation and growing of the damage (damage tolerance principle elucidated in paragraph 1.2.5) is not problematic as long as it can be autonomously healed (damage management) [35]. The concept and its potential effect on the service life of a structure can be represented in the diagram of figure S. Garcia in [36].

In the traditional material approach the service life of a structure can be extended by improving the initial mechanical properties of the material, see curve of the reference material (a) and traditional improved one (b). However, the traditional approach of increasing the initial material properties of the material leads to small improvement due to the big advances made so far. Moreover during the service life, loads higher than the limit for which the structure was designed can occur (e.g. impact). In this context, the healing approach offer a new strategy for increasing the service life of the materials and has already achieved significant results despite its young age (two decades).
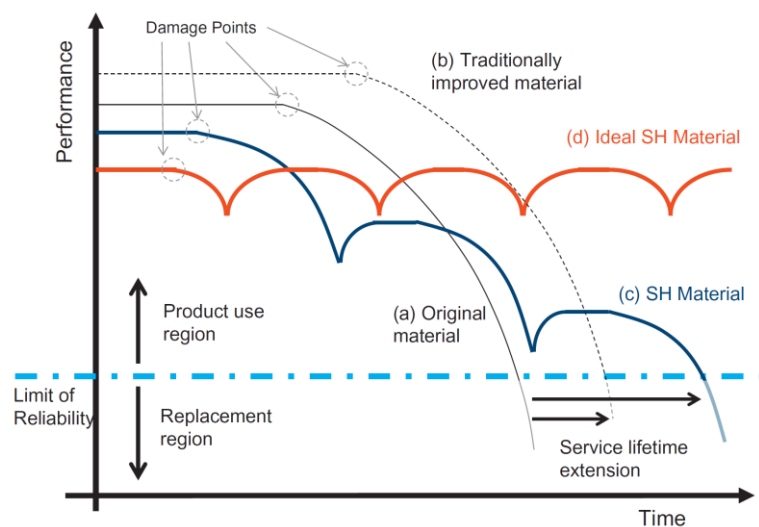
Fig 1-12 Service life of traditional and self-healing materials
Reproduced from Ref.[36]

Curve (c) represents the behavior of typical self-healing material in which the final failure of the material is postponed by the restore of the damage. However, the damaged zone has been partially repaired, therefore it is still weak and can fail another time. The degree of the healing of the second step is minimal and the failure of the material will be inevitable. The ideal self-healing material is the one capable of completely restoring the initial mechanical properties and do it multiple times, curve (d). The graph highlights another issue: the healing capability has to be conferred to the material without dramatically affecting its initial mechanical properties. Another essential requirement is that the material should heal autonomously without human intervention.

The rest of the paragraph will be focused on self-healing systems integrated in polymeric material, with special attention for the ones who can be suitable for composite laminate applications. Self-healing polymeric materials can be classified into two different groups, based on the approach to the self-healing mechanism: intrinsic or extrinsic.

Intrinsic self-healing systems:

Intrinsic self-healing polymers are materials capable of restoring a local damage by reformation of reversible bonds, via a temporary increase in the mobility of the polymeric chains. Healing can be obtained by physical interactions or can occur at chemical level by strong reversible covalent bonds or supramolecular interactions.

Among the *reversible covalent interactions*, retro Diels-Alder (DA) and disulfide reactions found a discrete interest for self-healing purpose [37]. Chen et. al. [38] developed a cross-linked material prepared through DA reactions, which have mechanical properties similar to epoxy (E=3.1 GPa and σ_R=68 MPa). DA reactions can be used to create different polymers, as dicyclopentadiene and epoxy with good mechanical properties [39], [40]. Mechanical failure leads breakage of the material covalent bonds, hence the retro-DA reactions, which can be reverted (DA) upon heating at 120-150 C to have healing (up to 50-70%). The thiol-based

polymers have disulfide bonds that can be reversibly cross-linked through oxidation and reduction. Disulfide-based epoxy resin containing chains with thiols as precursor can be used to produce healable thermoset rubbers [41]–[43]. After damage occur, the mechanical properties can be completely restored by applying a low temperature (60-70 C), but their low mechanical properties restrict their use in elastomer and coating applications (σ_R =0.2-0.4 MPa).

Supramolecular interactions allow for week and reversible non-covalent interactions between molecules which induces self-assembly capability [44]. Common interactions include hydrogen bonds and ionomers. Single monomers or molecules can by assembled via hydrogen bonds to form linear chains or high cross-linked polymers [45], [46]. The result is rubber polymers with high strain to break (400 % at 4 MPa), which can simply repaired by bringing together the fractured surface at room temperature [45]. Ionomers have ionized group covalent bonded to the backbone of the polymer chain which creates electrostatic interactions. Ionomers film have been proven to autonomously heal after ballistic puncture through the heat generated by the friction with the perforating bullet [47]. Also in this case, the low mechanical performance make restrict their application for elastomer and coatings.

Haling in thermoplastics can occur *physically* by molecular interfusion triggered by an external stimulus such as temperature (above Tg or melting point) or solvent (swelling) [48]. A physical and chemical hybrid option is to dissolve in the uncured epoxy resin a linear polymer with similar solubility parameters [49]. The linear polymer is bonded through reversible hydrogen bonding with the tri-dimensional epoxy matrix. Upon heating (140 °C for 6 hours) the hydrogen bond can be reverted and the linear polymer become mobile and flow to close the crack.

Generally, regardless of the chemistry employed, intrinsic healing requires a local reversibly of the bond interactions (covalent, supramolecular or entanglement) together with a local mobility of the constituents (molecules and polymer chains). The clearest advantage of intrinsic healing is that the reversible bonds interactions can be broken and reformed multiple times, thus giving to the material the possibility to heal infinite amount of times. The drawback is that to allow the bond reformations is necessary a certain mobility of the constituents which leads to generally lower mechanical properties. Furthermore, these materials generally needed an additional input of energy (e.g. temperature) to heal, since the reversible bonds have high activation energy. This makes intrinsic self-healing materials not completely autonomous. Comparing the results reported in literature on intrinsic self-healing materials it can be speculate that there is an opposite trend between the material strength and the ability to heal at low temperatures. For example, materials made of strong reversible covalent bonds such as DA needs high energy to be broken (which impart strength to the material) but also to be reformed (which means high healing temperatures). Instead, weak hydrogen bonds can be broken with low energy (which leads low material strength) but can be easily reformed (room temperature) which make the healing autonomous. Moreover, in

hard materials, the mobility of the chain is limited to few nanometers at most. The crack surfaces cannot come in to full contacts, due to plasticization and dendrites, making healing a significant challenge for intrinsic self-healing systems. These issues reduce the chance for a successful implementation of an intrinsic system in an autonomous self-healing composite laminate.

Extrinsic self-healing systems:

In extrinsic systems, the healing chemistry is separated from the surrounding not healable polymer matrix. The healing agent is encapsulated in discrete entities which can be broken upon damage/cracking and release it in the crack's meatus. Once the agent is released it should react and heal the crack. Extrinsic self-healing systems can be classified based on the employed encapsulation method: microcapsule, hallow fibers, vascular and core-shell.

Microcapsules:

Microcapsule is the simplest method to encapsulate and separate the healing agent from the surrounding matrix. A successful attempt was made by White et all in 2001 [50]. They mixed microcapsules (50-200 μm) filled with dicyclopentadiene monomer (DCPD), into the matrix with dispersed Grubbs catalyst (see Fig 1-13b). The healing capability was tested by mode I fracture test on tapered double cantilever beam (TDCB) specimens. Following the partial fracture of the sample, the capsules were ruptured and released the liquid DCPD into the crack (see Fig 1-13). The monomer, encountering the exposed catalyst on the crack surfaces, polymerized and healed the crack (see Fig 1-13a).

A significant restoration of the fracture toughness of the sample (75%) was achieved in 48 hours at room temperature with no manual intervention. Moreover, the recorded critical load to the crack onset, of the undamaged samples, was 20 % higher for the self-healing sample compared to the neat epoxy resin one. Therefore, the addition of the microcapsule and the catalyst can increase the inherent toughness of the neat epoxy resin.

Encouraged by the positive results, the research group studied the mode I fatigue behavior of TDCB specimens integrated with and without the same self-healing system. At moderate cyclic loading ratio (ΔK_I) the self-healing system had time to polymerize and extended the fatigue life of 200% [51]. The retardation of the crack propagation was ascribed to a crack tip shielding mechanism, generated by the polymerization of the released healing agent upon the crack propagation.

The next step was to integrate the self-healing system in composite laminates. The same research group evaluated the healing efficiency of CFRP woven laminates damaged by mode I loading [52]. The fracture toughness of the composite laminate was restored up to 45% by healing at room temperature. However, the percentage of weak microcapsules (20%) and catalyst's increased the thickness of the interlayer and decreased the initial fracture toughness of 20%, compared to the pristine composite laminate. Note that, the high

percentage amount of microcapsule was necessary to assure that adequate healing agent was available to heal the crack.
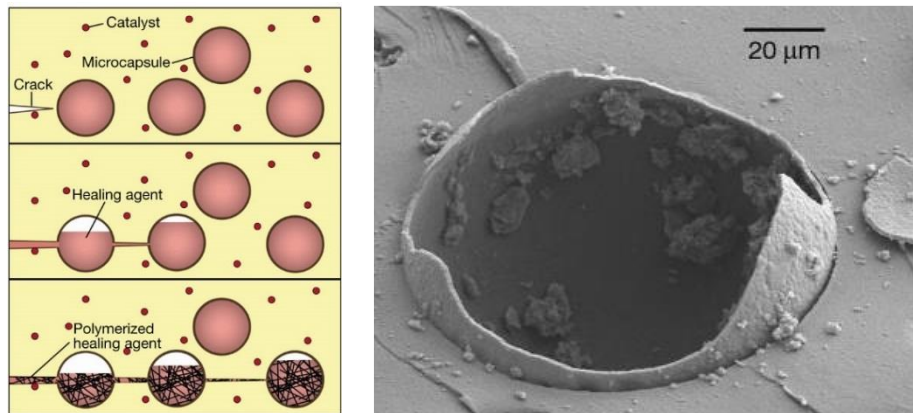
Fig 1-13 Self-healing microcapsule approach and SEM image showing rapture of the microcapsule. Reproduced from [50] with permission from Nature Publishing Group's.

GFRP woven laminates integrated with microcapsule healing system were tested at low velocity impact [53]. A reduction of 50% of the delamination length was observed after healing. However, despite the cracks have been repaired, the impact damage resistance (evaluated by compression after impact test, CAI) of the self-healing composites was lower than the pristine ones (-20%). The decrease of the residual strength after impact was linked to the detrimental effect of the microcapsule and the wax catalyst on the damage resistance of the composite laminate. Hence, the service life (see diagram of fig 1) of the self-healing composite laminate is lower than the pristine one, because the gain obtained by healing was lower than the decrease of initial mechanical properties caused by the introduction of self-healing system.

Vascular:

The main advantage of using hollow fibers, instead of microcapsule, is that they can theoretically provide an infinite amount of healing agent to fill the crack, taking it from the non-damaged zone A very early example of vascular self-healing system is the work of C. Dry et. al. in 1993 [20], which is also in general one of the first intentional manmade self-healing attempt. They filled millimeter-diameter glass pipettes with either cyanoacrylate [54] or a separated two part epoxy system [55] and they embedded them in a polymeric matrix. After crack propagation, they observed the release of the healing agent and they qualitatively verified the healing of crack by three-point bending test.

However, the diameter of the millimeter glass pipettes was too large to be implemented in the thin plies (0.2÷0.6 mm thick) of the composite laminates. Bond and coworkers filled micrometric hollow glass fibers (HGFs) with external diameter of 60 μm (Fig 1-14 a) with a pre mixed two-component epoxy resin [56] or each individual component separated [57], [58].

Quasi-isotropic $[0°/\pm45°/90°]_S$ GFRP laminates where integrated with the HGFs at the ($-45°/0°$) interfaces (Fig 1-14b). The damaged was initiated by three-point bending indentation

test and the residual strength was evaluated by four-point banding flexural test. The pre-damage flexural strength of self-healing sample was 16% lower than the flexural strength of the baseline one. However, the residual flexural strength of the self-healed laminates was completely recovered [58]. In the florescent micrograph of Fig 1-14c can be observed the "bleeding mechanism" of the healing agent mixed with a UV dye.
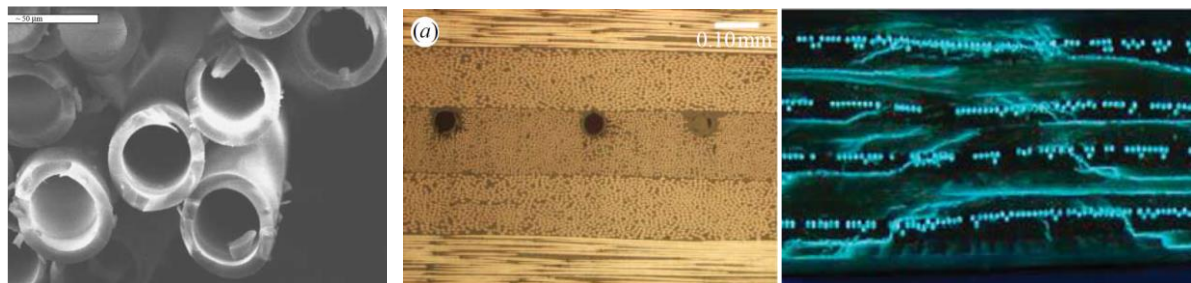
Fig 1-14 Hallow glass fibers (HGFs) (a); HGFs embedded in the composite laminate (b); Impact damage cross section of the laminate with HGFs contained healing agent mixed with florescent dye (c). Reproduced from Ref. [57] by permission of the Royal Society.

In the last decade, different variations of the vascular self-healing system were investigated. R.S Trask et al. [59] developed an automated system for the vascular network, in which the delivery of the healing agent is operated by a pump triggered by the damage. The system was integrated in composite laminate and the heling efficiently evaluated by compression after impact test. The self-healing automated system recovered more the 90% of the residual strength. A.M. Coppola [60] integrated a 3-D vascular network in woven laminate in order to increase the chance of deliver the healing agent upon damage, but the healing capability has yet to be verified.

Regardless the encapsulation architecture, extrinsic self-healing systems can heal the damage autonomously: they do not need of an external stimulus (such as temperature), and can fill small crack gaps. They can be implemented in polymer with high performance such as the epoxy of composite materials and often are able to restore the initial pre-damage properties. The drawback is that the damage can be healed only one time, especially if the second time it occurs in the previously healed location. Another important limitation is that microcapsules and microchannel require a large amount of damage to be raptured and so release the healing agent. Moreover, the introduction of the healing system in composite laminates tends to decrease the initial mechanical properties, due to the dimension of the encapsulant system compared to the thin interlayer.

An alternative extrinsic encapsulation method is the use of electrospun core-shell nanofibers filled with a healing agent. The main advantage, compared to micrometric encapsulation methods, is that the thin core-shell nanofibers should not affect the inherent properties of the baseline material, or even increase as has been already prove for monolithic nanofibers in chapters 2, 3, 4 and 5. Therefore, in the last chapter of this dissertation will be explored the development of a self-healing system for composite laminates based on core-shell nanofibers filled with epoxy resin as curing agent.

Interlaminar fracture toughening by nanofiber interleaving

2.1 Nanofibers

Fibrous hierarchical structures at the nanometer scale are the fundamentals building blocks of natural materials. For instance, in bones the collagen molecules are bundled to form fibrils with a diameter of ~ 1.5 nm; wood is composed of cellulose molecules that are combined to form elementary microfibrils with a diameter of ~ 10 nm, which then are bundled to form a microfibril with a diameter of 400 nm (see section 1.1).

Man-made nanofibers are defined as fibers with a diameter less than 100 nm. But in general, all the fibers with a diameter below 1 μm (=1000 nm) are recognized as nanofibers. They have special features that cannot be found in common bulk materials, as tremendously high specific surface area (SSA) and strength. By reducing the diameter of the fibers, the specific surface area (defined as the ratio of the area of a solid and its volume) grows proportionally ($SSA = 2\pi d/\pi r^2 \sim 1/r$). This leads to tremendously high values of SSA for nanofibers up to levels of 10^8 m^2/m^{3}The dimension reduction and the increase of the surface ratio greatly affect the chemical reactivity, the capacity of absorb or release molecules, the bonding with a surrounding matrix and so on. If the fibers diameter decreases, the strength increases due to the reduction of the chance of an inherent flaw in the material (as it happens for carbon fibers [9]). As the diameter becomes even smaller, as in the case of CNT, the perfect atomic range and the lack of defects in the material can confer to it a strength up to 30 GPa.

Although the effect of fiber diameter on the performance has been long recognized, the scientific community has found interest on polymeric nanofibers only in the last two decades with the rediscovery by Raneker et. al. of the electrospinning technology [61].

2.1.1 Electrospinning

Electrospinning is a fiber production method for ultra-fine polymeric fibers, patented by Cooley [62] and Morton [63] in 1902. Electrospinning process concerns the application of a high electric field between the tip of a capillary, in which a polymeric solution is pumped, and a ground collector (see Fig 2-1 a and b). The polymeric solution is a mixture of the polymer dissolved in one or more solvents. When sufficient voltage is applied, the liquid drop at the tip of the capillary (needle) becomes charged and the electrostatic forces oppose to the

surface tensions of the drop stretching it. Reached a critical voltage level the electrostatic forces overcome the surface tension and the liquid erupt from the drop surface forming what is named the Taylor cone. If the entanglement of the polymer chains is sufficient high, the solution stretches without breaking and forms a jet (otherwise fine drops erupt and electrospray occur). During the flight the solution jet dries and the charges migrates to the surface of the forming fiber. The jet is then elongated in whipped cone shape caused by the bending instabilities, induced by the electrostatic repulsion of the charges on the surface of the fiber, until finally it settles on the grounded collector forming a non-woven mat. The elongation and as consequence the thinning of the fiber, caused by whipping, leads to the formation of nanometer scale fibers.
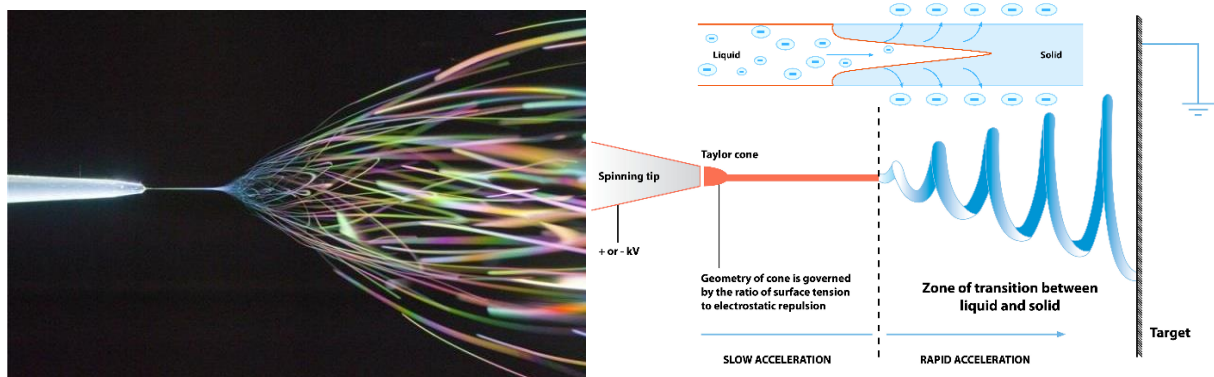
Fig 2-1 Fiber formation during electrospinning: high speed shot and diagram [64].

A lab-scale electrospinning setup consists of four major components (see Fig 2-2a): a high DC voltage power supply, a syringe with a metal needle (the capillary), a syringe pump end a grounded collector. Despite the electrospun instrumentation is quite simple, the process behind this technology is based on highly complex phenomena that involves different physics fields: electrostatic, chemistry, material mechanics and so on.
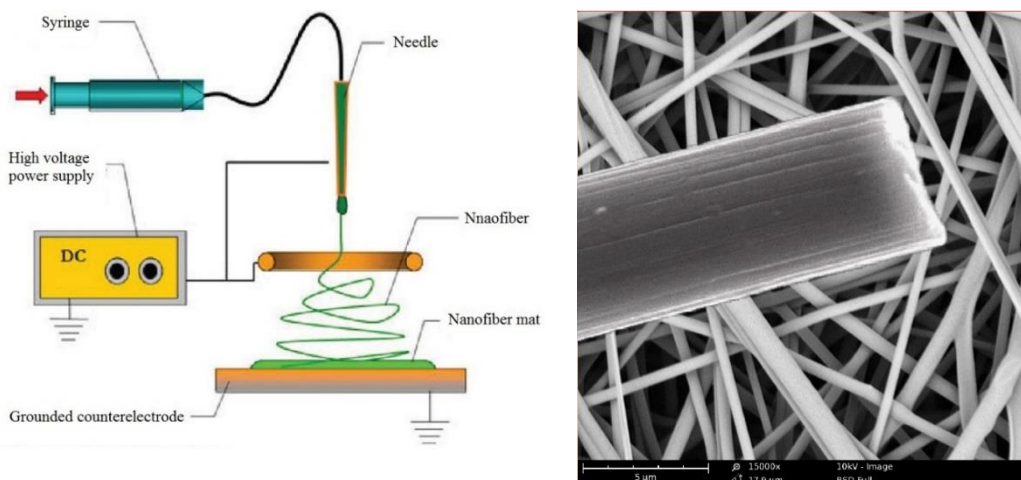
Fig 2-2 (a) Basic lab-scale electrospinning setup [65] and (b) Morphology of Nylon 6.6 nanofibers (on the background) compared with a carbon fiber (on the top).

2.1.2 Electrospinning process parameters

The proper control of the electrospinning parameters can lead to the fabrication of the electrospun nanofibers with the desired morphology and diameter (see Fig 2-2b). There are several parameters that can be tuned, below are listed those parameters and their effects on the process is briefly described [66], [67]:

Solution parameters:

- **Molecular weight** affects the entanglement of the polymer chains. Hence for a fixed concentration, lowering the molecular weight of the polymer leads to the formation of beads, while increasing makes smooth fibers and further increasing micro-ribbon will be obtained [68].
- **Concentration** of the polymer solution is a key parameter in the fiber formation. Based on the effect on the morphology, the concentration can be classified in four levels from low to high [66]:
    - when the concentration is very low electrospray occurs instead of electrospinning because of the low polymer chain entanglement compared to the surface tension;
    - increasing the concentration, a mix of fiber and beads are obtained;
    - when the concentration is proper smooth fibers can be obtained;
    - further increasing the concentration microfibers or ribbons are obtained.
- **Viscosity** of the solution is tuned by varying the polymer concentration. For low solution viscosity, surface tension overcome the entanglement and bead fibers are generated. When it is proper, continuous free-bead fibers are obtained. It is important to note that molecular weight, polymer concentration and viscosity are closely related and are dependent each other.
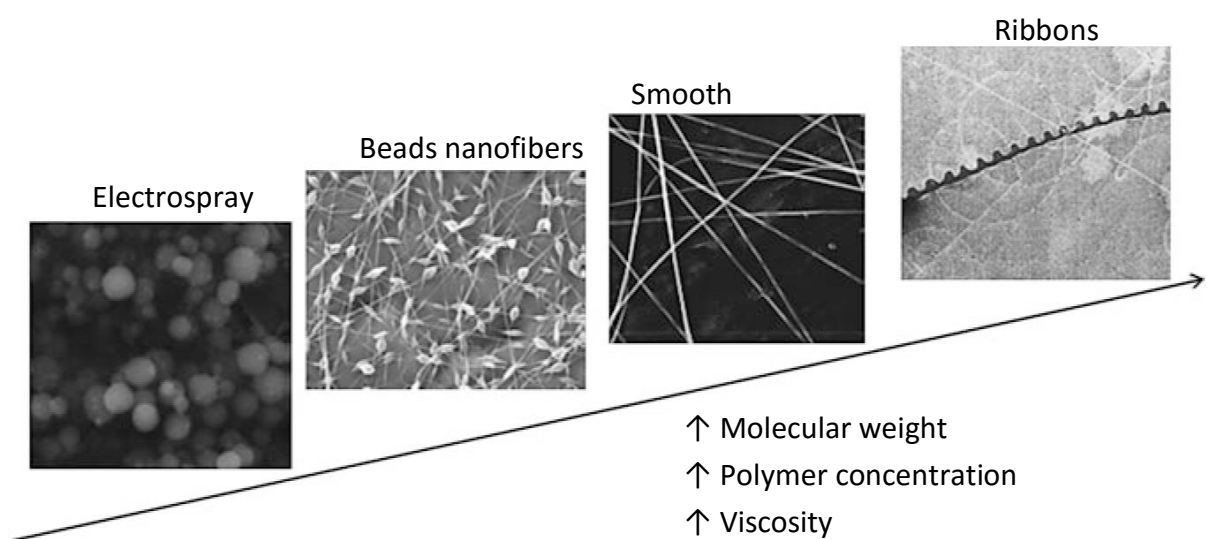
Fig 2-3 Effect of the molecular weight, polymer concentration and viscosity on nanofiber morphology (SEM images), adapted from Ref.[69], with permission of Springer.

- **Surface tension** can be reduced using a surfactant or a solvent/solvent mixture with lower surface tension. By reducing it, beaded fibers can be converted in smooth fibers.
- **Boiling point** effects how fast the spinned polymeric solution evaporates during the flight. If it is too low, wet fibers will deposit on the collector with the risk to melt each other creating a film instead of a nanofibrous mat. If it is too high, the capillary needle may become clogged.
- **Dielectric constant** affect the charge carrying ability of the polymer jet subjected to the electric field. Higher it is and stronger the polymer jet is attracted to the collector and thinner will be the electrospun nanofibers [67]. It is a constant which depends by polymer and the solvent. It can be tuned using organic solvents or salts.

Process parameters:

- **Applied voltage** threshold is the lower limit to have the charged polymer solution ejected from the Taylor cone. Below this threshold no electrospinning occur. The effect of the applied voltage on the fiber morphology is controversial in literature.
- **Distance between the capillary tip and the collector**. If the distance is too short, the solvent, contained in the spinned polymer solution, will not have enough time to evaporate and a melted nanofibrous mat will be produced. If it is too long, bead fibers may be obtained [67].
- **Flow rate**. By increasing it, the productiveness of the process rises. However, if it is too high, thick fibers will be formed because the amount of the solvent in the jet does not have time to evaporate and so low stretching and bending occur. In the worst case the capillary needle will split little dots on the nanofibrous mat.
- **Temperature and humidity** can affect the stability of the process and the quality of the nanofibers. Low humidity and high temperature may dry to fast the solvent before it gets spinned clogging the capillary. A too high humidity will lead to thick fibers because the electrostatic charge on the jet can be neutralized and as consequences the stretching and bending forces are reduced.

Each parameter described above could be tuned and controlled based on its governing physical equations. However, because the effects of a single parameter on the process depends on the others and because each parameter is related to a different physical phenomenon, it's difficult to have the full knowledge on the global governing equations of the multi physic electrospinning process. Therefore, it is difficult to know a priori the optimum process parameters. Often the electrospinning process of a new polymer is set up with a heuristic approach based on the knowledge of the trend of each parameter (governed by physics equations) and its effect on the electrospinning process based on the previous acquired experience and available data in literature.

2.1.3 Electrospun nanofibers: process, morphology and mechanical properties

In the studies presented in chapters 3, 4, 5 and 6 composite laminates were interleaved with two types of nanofibers, made of two different polymers: Polyamide (Nylon 66) and Polyvinylidene fluoride (PVDF). The electrospinning process parameter are described in Table 2-1.

Table 2-1 Electrospinning process parameters.

	Polyamide	Polyvinylidene fluoride
Commercial Name	Nylon 66	PVDF
Grade name	Dupont Zytel E53 NC010	Solvay Solef 6008
Polymer conc. (% w/v = % g/ml)	20	15
Solvents	Formic Acid / Chloroform (50/50 v/v)	Dimethyl sulfoxide / Acetone (30/70 v/v)
Flow rate per nozzle (ml/h)	0.3	0.6
Dist. Tip - Collector (cm)	15	12
Applied Voltage (kV)	24	12
Temperature (°C)	20-23	20-23
Relative humidity (%RH)	40-45	35-40
Nanofiber diameter (nm)	470 ± 110	500 ± 150

The nanofibrous mats were fabricated using a Spinbow® electrospinning machine in-house designed (Fig. 1a), equipped with a four-needle firing system and a rotating drum collector covered with polythene paper, in which the fibers were collected and safely removed once the process was finished. The tangential rotating speed of drum was set to 0.2 m/s, in order to obtain a random oriented nanofiber mat. The electrospinning process time was set, on the basis of the desired nanofibrous mat thickness, from 200 to 800 minutes. The mat was kept in oven at 40 °C overnight, before integrating it into the laminate, in order to remove residual solvent and absorbed moisture.

Fig 2-4 Spinbow® electrospinning machine.

The morphology of the Nylon 66 and PVDF electrospun non-woven mat so obtained are shown in the SEM micrographs of Fig 2-5 (a) and (b) respectively. The average diameter of Nylon nanofibers is 470 nm with a standard deviation of 110 nm. While average diameter of PVDF nanofibers is 500 nm with a standard deviation of 150 nm.

Mechanical, thermal and physical properties of the bulk polymers used to electrospun the nanofibers are reported in Table 2-2, according to the supplier datasheets.
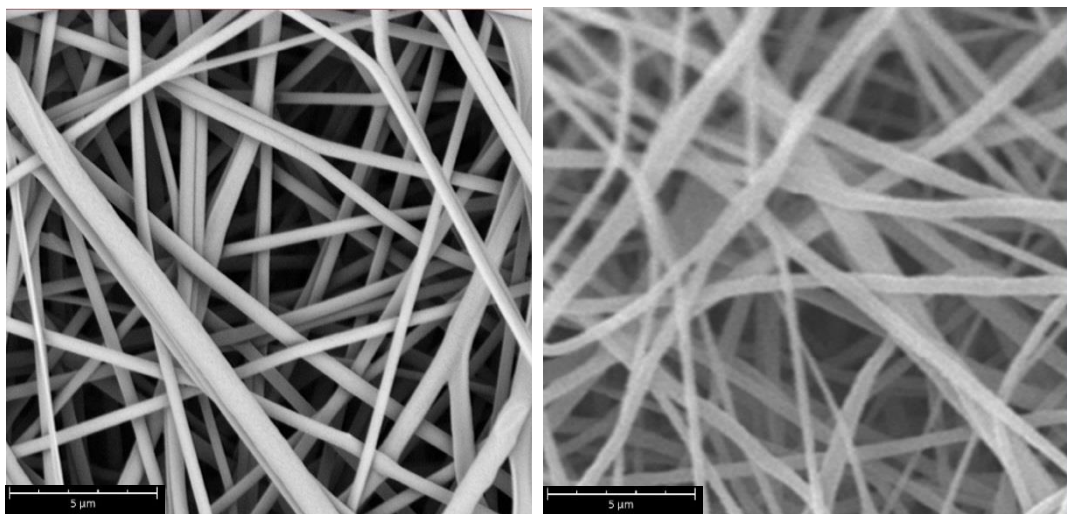
Fig 2-5 Morphology SEM analysis of (a) Nylon 66 and (b) PVDF nanofibers.

Table 2-2 Bulk material properties of electrospun polymers. Between brackets are reported the mechanical properties of the polymer moisture saturated at 50 % RH and 23 °C.

	Nylon 6.6	PVDF
Grade Name	DuPont Zytel E53N C010	Solvay Solef 6008
Specific gravity (Kg/m^3)	1140	1750
Tensile Modulus (GPa)	3.1(1.2)	1.8-2.5
Yield Stress (MPa)	85 (55)	50
Strain at Break (%)	>50	>100
Glass Transition Temp. (°C)	70	-40
Peek Crystallization DSC (°C)	220	140
Melting Temperature (°C)	262	175
Humidity absorption (%)	2.6	-
Water Absorption (%)	8.5	<0.04

The author want to point out that the mechanical properties of the resulting electrospun nanofiber may be different from the one of the bulk material. Indeed, during the electrospinning process the molecular chains of the polymer undergo to a tremendous stretching to get the nanometer diameter, which orient them (especially the amorphous phase) in the fiber direction. Arinstein Akadii et. al. [70] experimentally measured the elastic modulus of individual Nylon 66 nanofiber with different diameters, by the use of an atomic force microscope (AMF) cantilever beam. They found that the nanofiber elastic modulus, normalized to the one of the bulk material, grows inversely to its diameter, with an abrupt change around 500 nm (see Fig 2-6). Therefore, the elastic modulus of the nanofibers in the studies presented here (400-600 nm), is expected to be slightly higher than the raw bulk modulus.
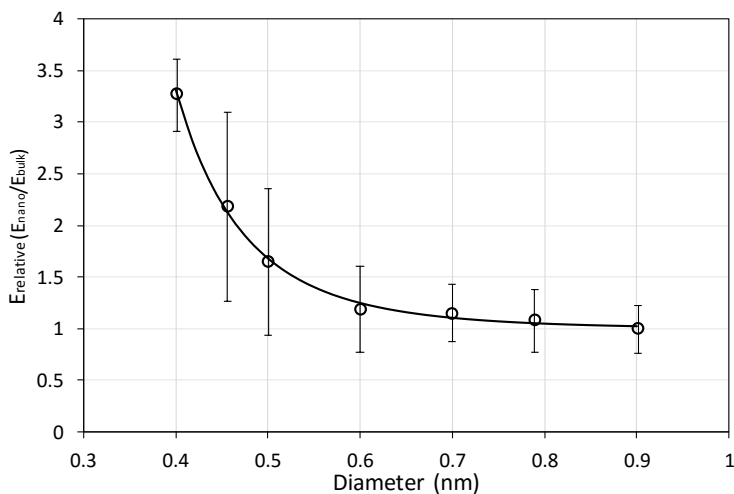
Fig 2-6 Relative elastic modulus of electrospun Nylon 6.6 nanofibers (normalized to the elastic modulus of the bulk material) as function of the diameter. Error bars show the standard deviation. Adapted from Ref. [70], by permission from Nature Publishing Group's.

2.2   Enhance of the interlaminar fracture toughness by nanofiber interleaving

2.2.1   Concept

As elucidated in the previous chapter, delamination is the most critical failure mode of composite laminates because, not being hindered at the ply interfaces, it can quickly propagate. A relative new approach for the delamination suppression consist in toughening the ply-ply interfaces of the laminate by using polymeric nanofibers, which was patent by Dzenis in 1999 [71]. However, despite the exhaustive amount of works available in literature on electrospinning since it was rediscovered by Raneker et. al. in 1995, research on the enhance of fracture toughness of composite material by using nanofibers is still in its infancy. The first scientific work, according to a research on Scopus (using "nanofiber" and "composite" keywords), is from 2006 [72]. In the last few years, probably due to the obtained positive results, the research on this field is growing exponentially.

This technique consists on inserting, between one ply and the other one of the laminate a non-woven mat made of continuous polymeric nanofibers (Fig 2-7). The diameter of the nanofibers (secondary reinforcement) usually range from 200 to 1000 nm; while the diameter of the carbon and glass fibers (primary reinforcement) are 5÷8 μm and 9÷25 nm, respectively (see for comparison Fig 2-2 b). Therefore, the diameter of the secondary reinforcement is an order of magnitude less to the diameter of the primary one. The nanofibrous mat (interlayer) is usually 30÷80 nm thick; while the plies (layer) of the base laminate are 0.2÷0.6 mm thick. Also in this case, the thickness of the nano interlayer is almost an order of magnitude less than the ply.
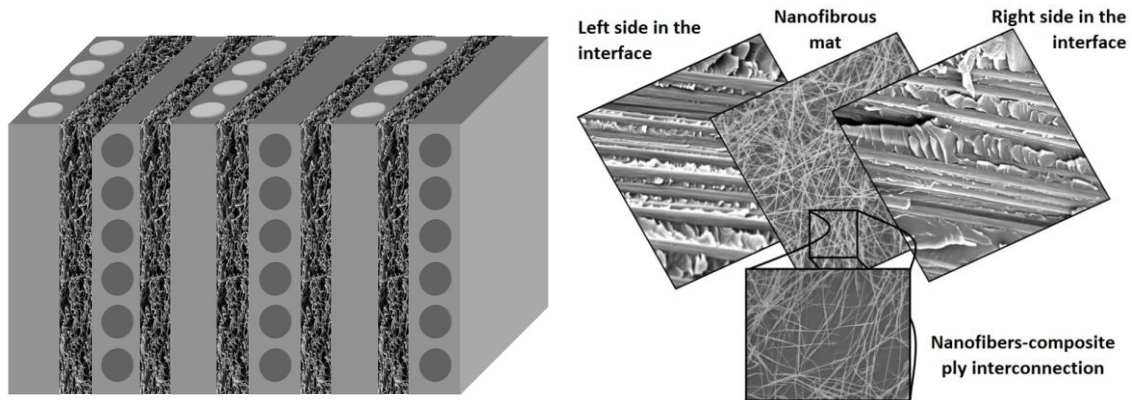
Fig 2-7 Diagram of the nano-interleaving concept: a) non-woven nanofibrous mats interleaved between microfiber plies; b) stacking sequence of the nano-reinforced laminates. Adapted from Ref. [73], with permission from John Wiley and Sons.

The background idea of toughening composite laminates by nanofiber interleaving, as nano-size reinforcements in general (e.g. CNT and MWCNT), is to increase the hierarchical structural complexity of the composite material. By adding a nano-reinforcement the hierarchical level is increased from two to three: the laminas defined at the sub-millimeter scale, the fiber and the matrix at the micron length scale and the nanofibers at the nanoscale.

From a more general view, nanofibers complete the missing ring of the hierarchical scale in composite materials, which starts from the laminate dimension and ends with the epoxide functional groups (see Fig 2-8).
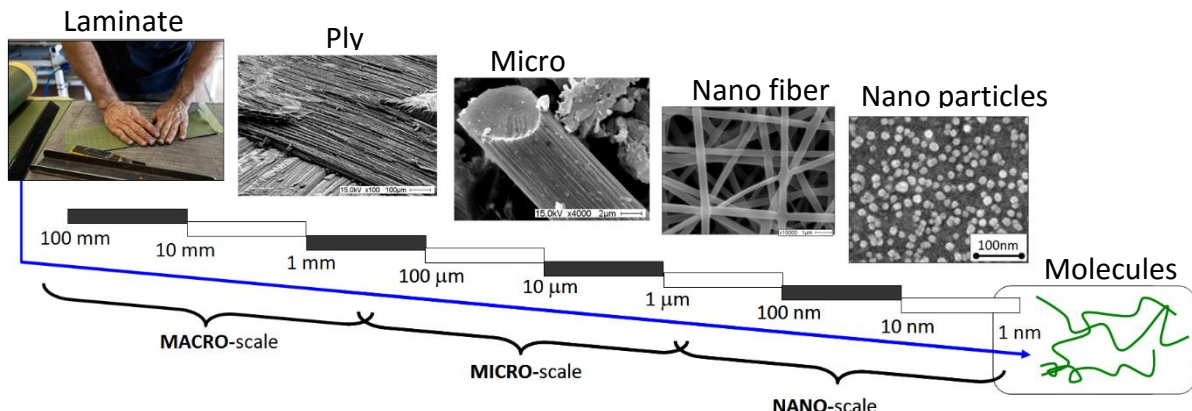
Fig 2-8 Hierarchical structure composite laminates completed by nanofibers

Compared to conventional interlaminar toughening techniques (see section 1.3.1), nanofibrous mat interleaving presents different advantages:

- The high porosity of the nanofibrous mat allow the resin to easily flow through it and impregnate it. Moreover, being porous its weight is relatively low and a negligible amount of weight is added to the laminate.
- The thickness of the nanofibrous mat is small enough that the resin already contained in the prepreg is enough to impregnate it. Hence no excess of matrix resin is added to the original laminate, which is the weak phase of the composite and is responsible for

the increase of weight without adding any strength to the laminate, as usually happen for classic interleaving techniques (see section 1.3.1).

- The fine polymeric nanofibers are flexible and are expected to conform the shape of the primary reinforcement architecture at the ply interfaces, eliminating so the resin rich zones (resin pockets) between one ply and the adjacent one and thus creating a solid bonding between two the adjacent plies.

- The polymeric nanofibrous mat usually does not dissolve in the epoxy matrix and is confined in the interlayer, hence does not affect the matrix-microfiber adhesion and the stiffness of the matrix within the fiber tow of the single plies (which is crucial to keep the microfibers in position and avoid micro buckling).

Moreover, this innovative technique can be scaled at industrial level, since medium volume electrospinning machines (based on needle less technology) are now available (see for instance the Elmarco's Nanospider).

2.2.2 State of art on Nylon nanofiber reinforced laminate

In the last decade, the number of publications on the interlaminar fracture toughening of composite laminates by nanofiber interleaving has increased exponentially, surpassing the threshold of 150 papers in 2017. One of the most used polymer for nanofibers is Nylon. Therefore, a specific literature survey on CFRP unidirectional and woven laminates interleaved with Nylon nanofibers was performed [46]–[54] and the obtained results were compared (see the bar chart of Fig 2-9). It was found a wide scatter in the results: some researcher reported an increase, by nanofiber interleaving, on the mode I interlaminar fracture toughness at initiation (GIc) of 242% while others have even recorded a decrease (-22%).
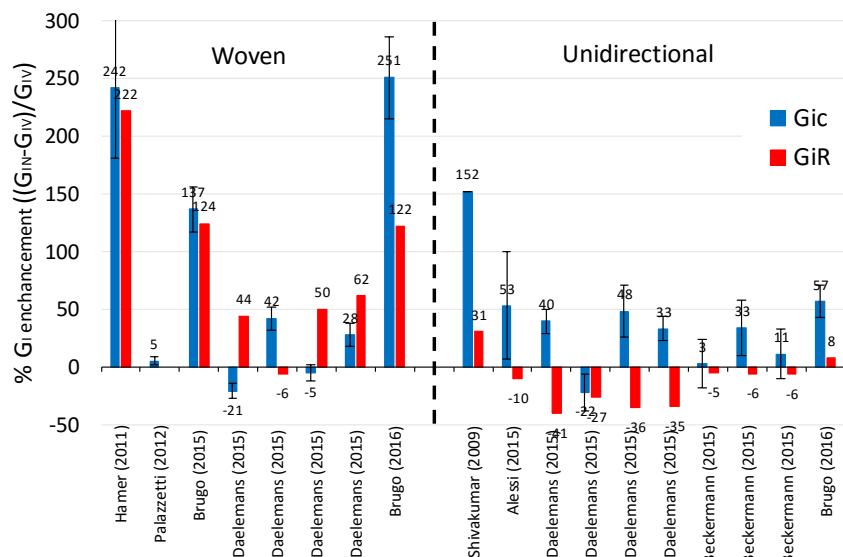
Fig 2-9 State of art on mode interlaminar fracture toughness enhancement for carbon woven and UD laminates interleaved with Nylon nanofibers.

2.2.3   Optimization of the nanofibrous mat interleaving process

The strong discrepancy on the results has been linked to issues in the integration process of the nanofibrous mat in the laminate. Hence, the fabrication process was optimized, working on the following key points:

- moisture absorption of the nanofibers
- nanofibrous mat transfer to the prepreg
- resin impregnation of the porous nanofibrous mat
- uniform pressure exerted on the interleaved prepreg

Moisture absorption of the nanofibers:

Nylon is a highly hygroscopic polymer. Moreover, the extremely high specific surface area (SSA) of the nanofibers tremendously accelerate the moisture absorption rate. Shoenmaker et. al. [74] studied the evolution of the moisture absorption for the Nylon 66 nanofibrous mat exposed at 50 % of relative humidity at 23 °C (see Fig 2-10). The curve shows that the nanofibrous mat can reach the saturation of 2.5 % in weight of water in less than 10 minutes, which is much shorter than the time necessary for the integration in the laminate. Moisture can reduce the mechanical properties of the polymer (see values between brackets in Table 2-2). Moreover, once the nano-mat is integrated in the composite, the absorbed moisture can diffuse in the epoxy matrix effecting the curing kinetic [74] and the final mechanical properties of the laminate [75]. Therefore, in order to avoid moisture inclusion and hence a decrease of the mechanical properties, the lamination process of the nano reinforced composite has to be made at low humidity ambient (40% RH at 20 °C).
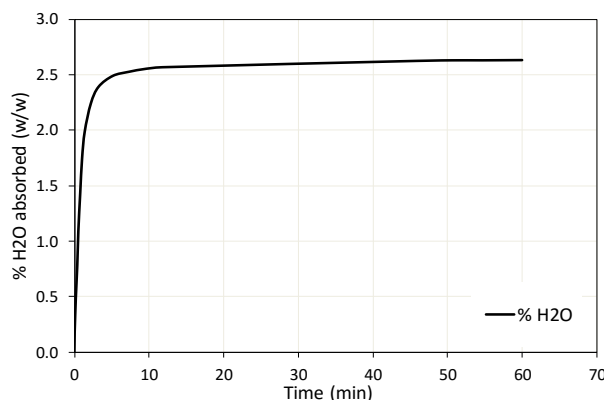
Fig 2-10 Evolution of moisture absorption for Nylon nanofibrous mat at 50 % RH at 23 °C. Adapted from Ref. [76], with permission from Elsevier.

Nanofibrous mat transfer to the prepreg:

The nanofibers were incorporated in the laminate, using a technique similar to the "Action Transfers" one: the electrospun mat, still with the polythene sheet (on which it was electrospun), was transferred to the prepreg, by rolling it softly; then, when it was completely absorbed by the resin, the polythene sheet was peeled off and the another prepreg ply was stacked on it. In this way, the electrospun mat was completely transferred to the prepreg avoiding so any delamination

32

Impregnation of the porous nanofibrous mat:

Prepregs are partially re-acted, by the supplier, to keep the fiber reinforcement together and to be handled during the lamination process. Hence the epoxy resin of the prepreg is very viscous at ambient temperature (>10^6 Pa s). While the porous nanofibrous mat (Fig 2-11 (a)) in order to be perfectly integrated in the laminate has to be completely impregnated by the resin. The viscosity of the resin and therefore its permeability, is closely linked to the temperature and its degree of crosslinking, which in turn depends on the temperature and time. In Fig 2-11 (b) the viscosity of the resin is plotted as a function of temperature for heating rate of 3 °C/min, according to the supplier data sheet of the prepreg used in the tests. By increasing the temperature, the viscosity decrease up to it reaches a minimum point to then increase again, due to the acceleration of the crosslinking reaction, which is caused by the temperature and hence the mobility of the epoxide groups and the curing agent.
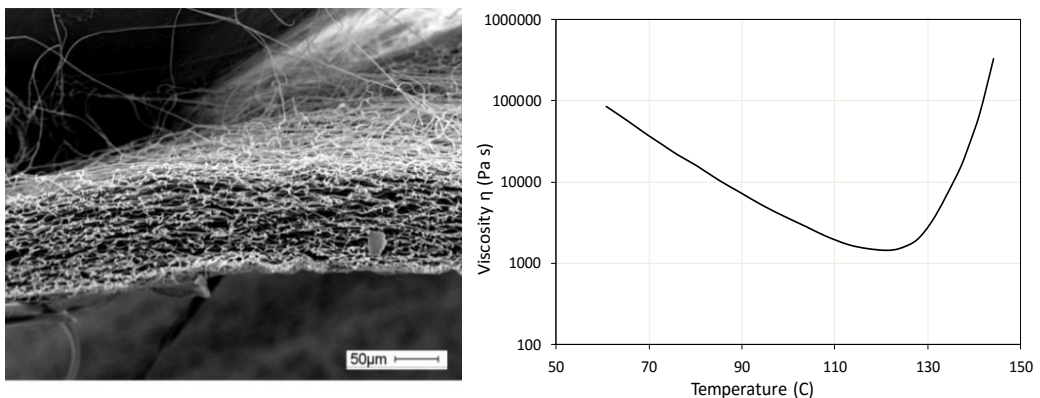
Fig 2-11 (a) Cross section of the porous nanofibrous mat; Evolution of the viscosity as function of the temperature for a heating rate of 3 °C/min of Impregnatex IMP503Z prepreg epoxy resin.

Based on the observations mentioned above, the standard curing cycle of the prepreg was modified in order to facilitate the impregnation of the nanofibrous mat. An initial plateau at 60 °C for 2 h was added to the standard cycle in order to allow the resin to fully penetrate in the porous nano mat before it starts to crosslink. Then, the temperature was raised to the prescribed temperature of 130 °C in order to complete the crosslinking of the resin.
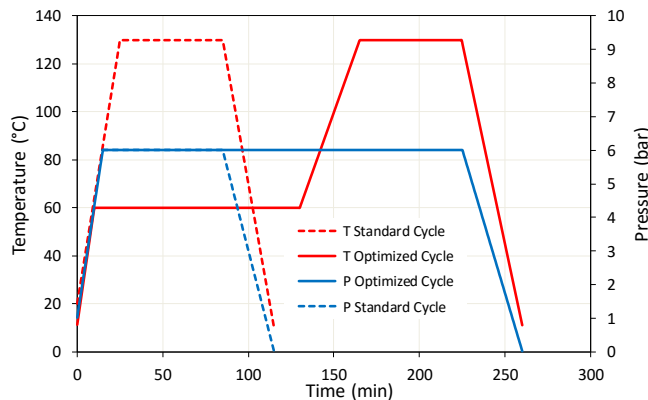
Fig 2-12 Standard prepreg curing cycle and optimized one for nonreinforced laminates

Uniform pressure exerted on the nano interleaved prepreg:

The literature survey on Nylon nanofiber interleaved laminates (see bar graph of Fig 2-9) shows that the results, at crack initiation, for woven laminates are highly scattered compared to the unidirectional ones. The cause is strictly linked to the architecture of the primary reinforcement and can be explained by analyzing the cross section of the nano-interleaved woven laminate, which has given poor results (see micrograph of Fig 2-13 a). The presence of areas with a greater enrichment of the matrix (called resin pockets), caused by the weave of the fabric and by the manufacturing process, can be thick up to 100 μm. In woven laminate, this prevents the thin nanofibrous mat (40μm) to effectively link upper ply to the lower one, and therefore contrast the crack propagation. While, in a unidirectional laminates resin pockets are absent and hence the results are not affected by this issue. The problem was solved by the use of the vacuum bag molding process (see Fig 2-13 b) instead of the press one. In this way, was possible to exert a uniform pressure on the prepreg and the excess of resin (resin pockets) were squeezed out during the curing cycle allowing the nanofibers to effectively link the two adjacent layers.
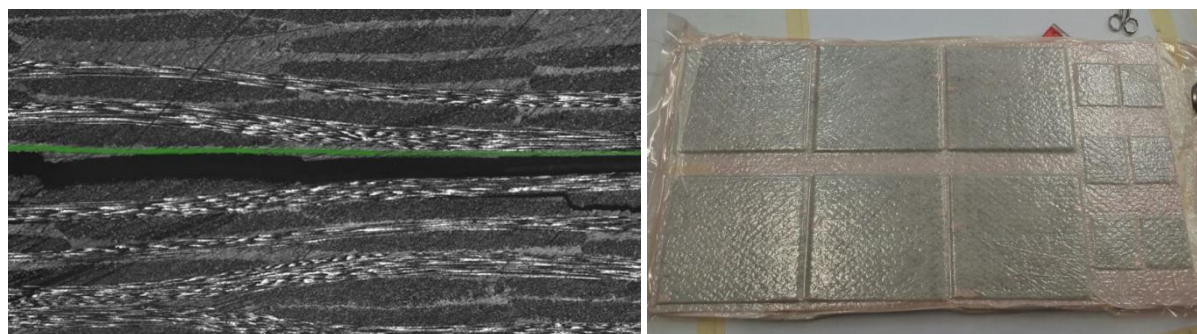
Fig 2-13 a) Micrograph of the cross section of Nylon nano interleaved woven laminates which have given poor fracture toughens enhancement (GIc). (b) Standard and nanomodified samples cured with the vacuum bag technique.

The just described optimized process for the integration of the nanofibrous mat in composite materials has allowed the full expression of the toughening effect by nanofiber interleaving. This has permitted to increase the fracture toughness enhancement in mode I (GIC) from the 20% with the old interleaving process to up 250% with the new one.

2.2.4   Studies on nano reinforced laminates

Once the process was optimized, the author investigated different aspects on the enhance of the interlaminar fracture toughness of composite laminates by nanofiber interleaving. The results of this studies are reported in the following chapters:

- In *Chapter 2* the fracture toughening mechanism and enhancement in composite laminates interleaved with Nylon 6,6 nanofibers was studied. The effect of the nano mat thickness on the primary reinforce architecture (UD and woven) was investigate on mode I and II loading.

- In *Chapter 3* the toughening effect of a different polymer (PVDF) which melted during the curing process was investigated.

- In *Chapter 4* the fatigue behavior to the onset of the delamination and the crack growth rate of woven laminates interleaved with electrospun Nylon 6,6 nanofibers was assessed.

- In *Chapter 5* fiber metal laminates (specifically GLARE), were interleaved at the aluminum-glass interfaces with electrospun nanofibers and their low velocity impact behavior was investigated.

The effect of thickness of Nylon 6,6 nanofibrous mat on Modes I–II fracture mechanics of UD and woven composite laminates

3.1 Introduction

Interleaving composite laminates with polymeric nanofiber is now an established method to reduce the risk of delamination without affecting the in-plane properties of the original laminate [77]. Plenty of research has been done on the topic of composites interleaved with nanofibers, and there is a general agreement that under certain specific conditions of resin-polymer compatibility, size and amount of interleave, and type of material, nanofibers can bring significant benefits to the composite [77]–[85]. However, the results produced by the literature are scattered, because they come from different sources, which have different boundary conditions which focus on a single aspect. Hence, it is missing a clear correlation between the different parameters that involves the nanofiber interleaving technique and their effect on the fracture toughness of the laminate.

This chapter presents an experimental campaign on samples made of unidirectional (UD) and Plain Weave (PW) laminae, aiming to investigate the effect of the thickness of the nanoreinforce and to study the different behaviors of the laminate architecture when interleaved with nanofibers.

Up to now, the only work comparing fracture mechanics behavior of UD and PW nanomodified samples is that of Daelemans et al. [86]. They tested virgin and nanomodified samples under Mode I and Mode II loading condition, using two different density of PA6,6 and PA6,9 nanofibrous veils. Their results showed a large enhancement of mode II energy release rate while poor results were found for mode I crack propagation. The discrepancy in the results was attributed to a less optimal loading of the nanofibers, dependent on the primary reinforcement fabric architecture, and the presence of a carbon fiber bridging zone. Their results, supported by Scanning Electron Microscopy (SEM) pictures of the fractured surfaces, highlight the importance of nanofiber bridging in arresting the crack propagation.

In this chapter, a different outcome will be exposed, as well as a different reinforcing mechanism; micrographs of the crack path taken on the tested specimens will be used to explain the results. Specimens have been tested under double cantilever beam (DCB) and end notched flexure (ENF). The interlaminar fracture toughness, in mode I and II, at initiation (G_C) and propagation (G_R) of the crack have been determined for each configuration to assess the effect of the nano interleave.

3.2   Experimental

3.2.1   Sample preparation

UD samples have been prepared stacking 20 plies of 130 g/m^2 unidirectional carbon/epoxy prepreg (HS15/130DLN2-IMP505L) supplied by Impregnatex Composite Srl (Milan, Italy). PW samples have been prepared stacking 14 plies of 220 g/m^2 plain weave prepreg (GG204P-IMP503Z), supplied by Impregnatex Composite Srl (Milan, Italy).

Nylon 6,6 Zytel E53NC010 provided by DuPont was used for producing nanofibers by means of electrospinning using the process parameters reported in Table 2-1. The nanomodified specimens were interleaved in the mid-plane with the nanofibrous mat following the procedure presented in section 2.2.3. A 30 µm thick PTFE film was also inserted in the mid-interface of all the specimens during the lay-up to create an initial artificial crack. All samples were cured in autoclave, under a pressure of 6 bar, for 2 hours at 60 °C and then for 1 hour at 130°C, as described in section 2.2.3.

From here on, virgin samples will be identified with the character ''V'', and nanomodified ones with the characters ''NY''. In total 6 different configurations have been manufactured as summarized in Table 3-1. For each configuration, a rectangular panel was fabricated, and 6 samples were extracted from each one: half of them where tested under Mode I, the other half under Mode II. No appreciable difference in thickness between V and NY samples has been registered.

Table 3-1 Summary of the tested configurations.

Code	Nanofibers	Mat thickness	Fabric
V $_{UD}$	No	–	UD
V $_{PW}$	No	–	PW
NY$_{40;UD}$	Yes	40 µm	UD
NY $_{90;UD}$	Yes	90 µm	UD
NY $_{40;PW}$	Yes	40 µm	PW
NY $_{90;PW}$	Yes	90 µm	PW

3.2.2 Fracture mechanics tests

Mode I

DCB samples have been prepared according to the ASTM D5528 [87]: 140 mm long, 20 mm wide, initial crack of 45 mm, aluminum blocks glued on the tip for the application of the load. DCB tests have been performed in order to calculate the energy release rate for Mode I loading G_I, using Eq. (3-1), from the Modified Beam Theory (MBT) presented in [87]:

$$G_I = \frac{3F\delta}{2B\alpha}$$ (3-1)

where F, δ, B and α are the force, the displacement of the load head, the specimen width and the crack length respectively.

The tests were carried out in a servo-hydraulic press machine (Instron 8033) equipped with a dedicated in-house designed and manufactured 250 N load cell, under displacement control condition, at a constant crosshead speed of 3 mm/min. A uniball-like feature on the grippers avoided any undesired loads. During each test, the load-displacement curve was recorded and the crack propagation was visually determined by means of a high-resolution camera focusing on the edge of the specimen.

For a better understanding of the results, the crack propagation is split into two stages: the initiation stage, in which the delamination onset starts from the artificial crack (critical energy release rate, G_{IC}) and the propagation stage evaluating the crack between 60 and 80 mm of length (propagation energy release rate, G_{IR}).

Mode II:

No official international standard for ENF tests has been developed so far, therefore the authors followed the guidelines provided in [88], and manufactured specimens 130 mm long, 20 mm wide, with an initial crack of 22 mm. The span between the two supports was 80 mm. From the ENF tests the levels of critical and propagation fracture toughness, $G_{II,C}$ and $G_{II,R}$ respectively, have been determined for each specimen using Eq. (3-2) [88]:

$$G_{II} = \frac{9F\delta a^2}{2B(0.25L^3 + 3a^3)}$$ (3-2)

where L is the span width.

The tests were carried out in a servo-hydraulic press machine (Instron 8033) equipped with a 2 kN load cell, under displacement control condition, at a constant crosshead speed of 1 mm/min. During each test, the load-displacement curve was recorded and the crack propagation was visually determined by means of a high-resolution camera focusing on the edge of the specimens.

3.3 Results and discussion

The next section presents separately the results of the two types of tests, highlighting the different effect of the nanofiber interleaving on the two different types of composite laminate.

3.3.1 DCB

Fig 3-1 shows the force-displacement curves of the representative sample of each configuration. After the first force drop, the delamination propagates in a discontinuous way and the load-displacement curves for PW laminates appear jagged. This behavior is strictly linked to the in-homogeneity of the interlaminar region in woven laminates. The crack, during its propagation, meets alternately zones with different toughness, due to the presence of resin pockets and the fabric texture [89]. The maximum force registered during the tests has been extracted from the charts and presented in Table 3-1. The presence of the nanofiber clearly postpones the crack initiation and increases the maximum force value on both UD and PW laminates.
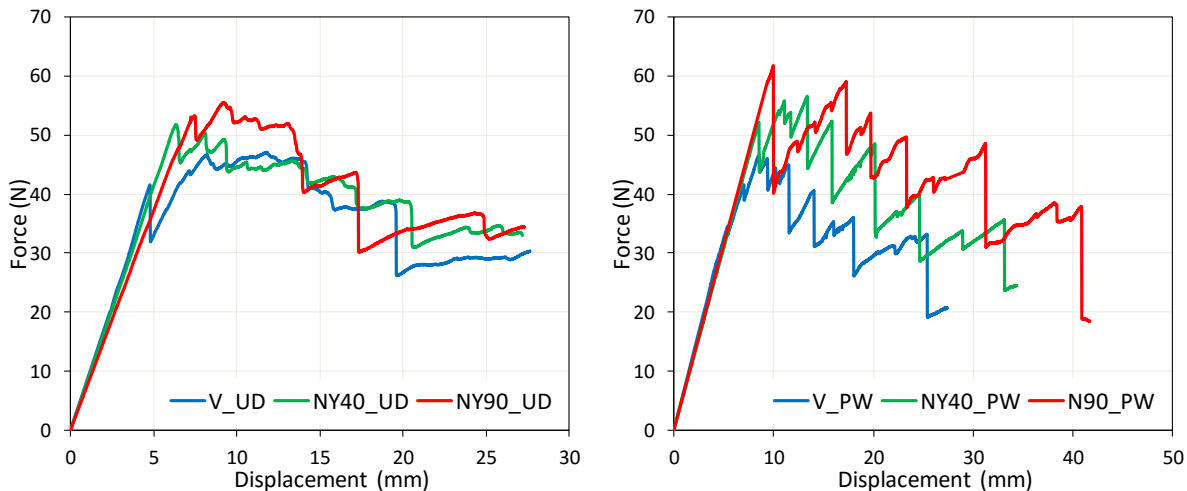
Fig 3-1 Representative DCB force displacement curves.

Table 3-2 Results of DCB test

	F_{max} (N)		G_{IC} (J/m^2)		G_{IR} (J/m^2)	
UD						
	Mean	Δ (%)	Mean	Δ (%)	Mean	Δ (%)
V	45.12 ± 1.77	–	328 ± 39	–	618 ± 62	–
NY$_{40}$	49.47 ± 2.52	+10 ± 7	514 ± 11	+56 ± 12	668 ± 62	+8 ± 14
NY$_{90}$	51.5 ± 3.88	+14 ± 10	484 ± 62	+48 ± 23	687 ± 78	+11 ± 16
PW						
	Mean	Δ (%)	Mean	Δ (%)	Mean	Δ (%)
V	46.63 ± 1.43	–	311 ± 40	–	673 ± 78	–
NY$_{40}$	55.37 ± 2.93	+19 ± 7	718 ± 70	+131 ± 31	938 ± 40	+40 ± 14
NY$_{90}$	62.47 ± 1.69	+34 ± 5	1091 ± 18	+250 ± 35	1496 ± 133	+122 ± 27

As mentioned above, G_I has been calculated several times during the tests, and the resulting R-curves, showing the energy release rates G_{IC} and G_{IR} as function of the crack length, are plotted in Fig 3-2. It can be observed that for all the specimens the values of G_I are minimum at the beginning of the crack propagation and then increase significantly up to they reach a stable value. G_{IC} and G_{IR} have been determined and presented in Fig 3-3 and Table 3-1. Results show a general improvement on both UD and PW samples when the nanofibers are employed. Nevertheless, two different effects can be observed:

- from the R-curves in Fig 3-2, the fracture toughness enhancement, due to the presence of the nanofiber, for woven laminates is registered at both initiation and propagation stages. On the other hand, the fracture toughness increment for UD laminates is only registered at the initiation, while improvement at propagation are negligible;
- the bar graphs in Fig 3-3 show that fracture toughness increases in PW laminates whit the nanofiber mat thickness, while UD laminates are not affected by the nanoreinforce thickness.

The reason for this phenomenon will be clarified by the micro-graph analysis in section 3.3.3.
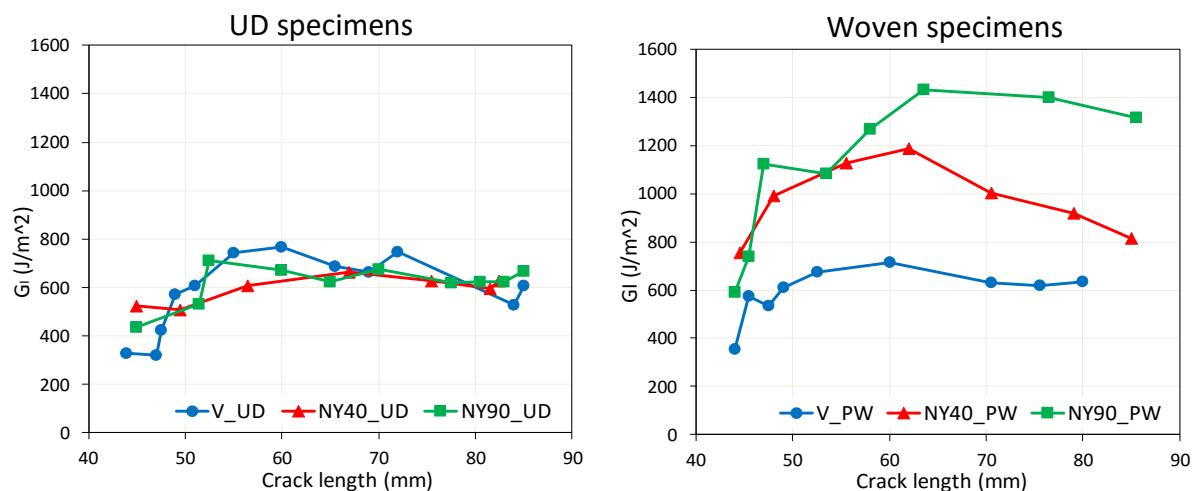
Fig 3-2 Representative R-curve for DCB tests.
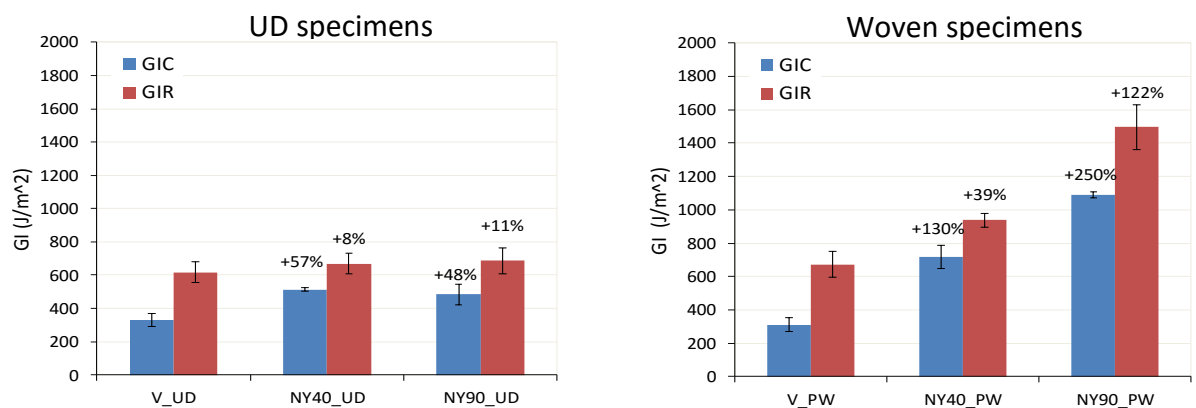
Fig 3-3 Initiation and propagation energy release rate for Mode I loading.

3.3.2   ENF

Fig 3-4 shows the force–displacement curves of the representative samples of each configuration, extracted during ENF tests. The force vs. displacement curves for UD laminates show an abrupt drop of the load associated to a sudden non-stable crack propagation, making the rest of the test useless for the purposes of this paper; on the other hand, in woven laminates the crack propagates stably with a stick–slip behavior. The maximum force registered during the tests has been extracted from the charts and presented in Table 3-3.
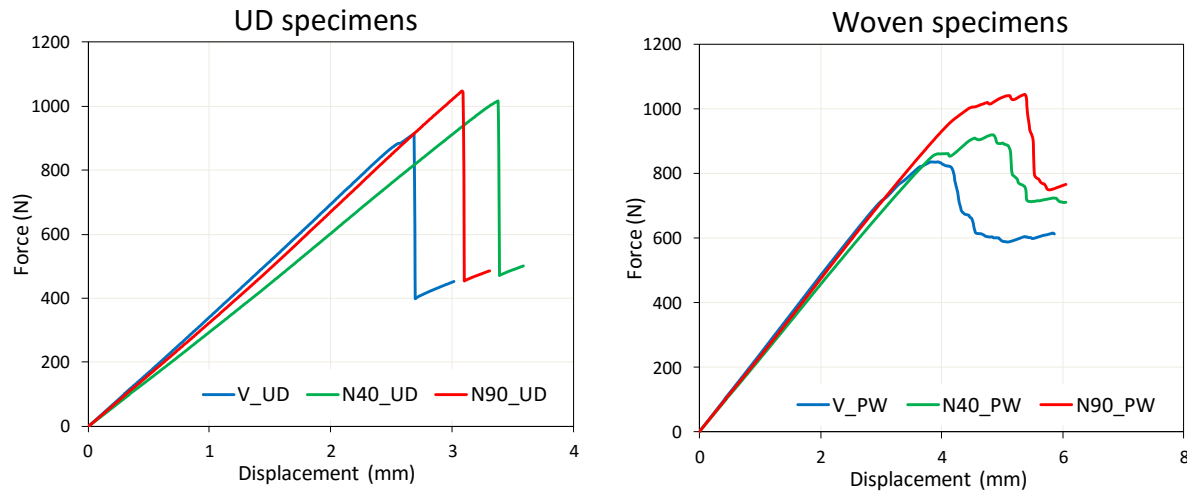
Fig 3-4 Representative ENF force displacement curves

Table 3-3 Results of EFN tests

	F_{max} (N)		$G_{II,C}$ (J/m^2)		$G_{II,R}$ (J/m^2)	
UD						
	Mean	Δ (%)	Mean	Δ (%)	Mean	Δ (%)
V	859 ± 54	–	1211 ± 207	-	N/D	-
NY$_{40}$	962 ± 62	+12 ± 10	1952 ± 127	+61 ± 20	N/D	-
NY$_{90}$	1045± 2	+22 ± 6	1966 ± 80	+62 ± 19	N/D	-
PW						
	Mean	Δ (%)	Mean	Δ (%)	Mean	Δ (%)
V	849± 13	–	1762 ±10	–	3254 ± 189	–
NY$_{40}$	944± 22	+11 ± 4	2536 ± 207	+44 ± 12	3514 ± 337	+34 ± 10
NY$_{90}$	1060 ± 42	+25 ± 5	4359 ± 238	+99 ± 19	4314 ± 137	+32 ± 7

As mentioned above, G_{II} has been calculated several times during the tests, and the results are plotted in Fig 3-5. For the reason explained above, experiments on UD samples allowed to measure fracture toughness only at the initiation stage; tests carried out on PW samples instead have been also completed for propagation stage. Critical and propagation energy release rates are plotted in the charts of Fig 3-6 . Table 3-3 summarizes the increments of G_{II} due to the nanofiber interleaving.

Results show a general improvement on both UD and PW samples when the nanofibers are employed. Similarly to what shown for Mode I, at the initiation stage, fracture toughness

of UD laminates is not influenced by the nanofiber mat thickness, while PW laminates show growing rates of performance with the increase of the mat thickness. Different results can be seen at propagation stage, where PW G_{IIR} is not affected by the nano-mat thickness. Overall, higher increments are registered for Mode I than Mode II.
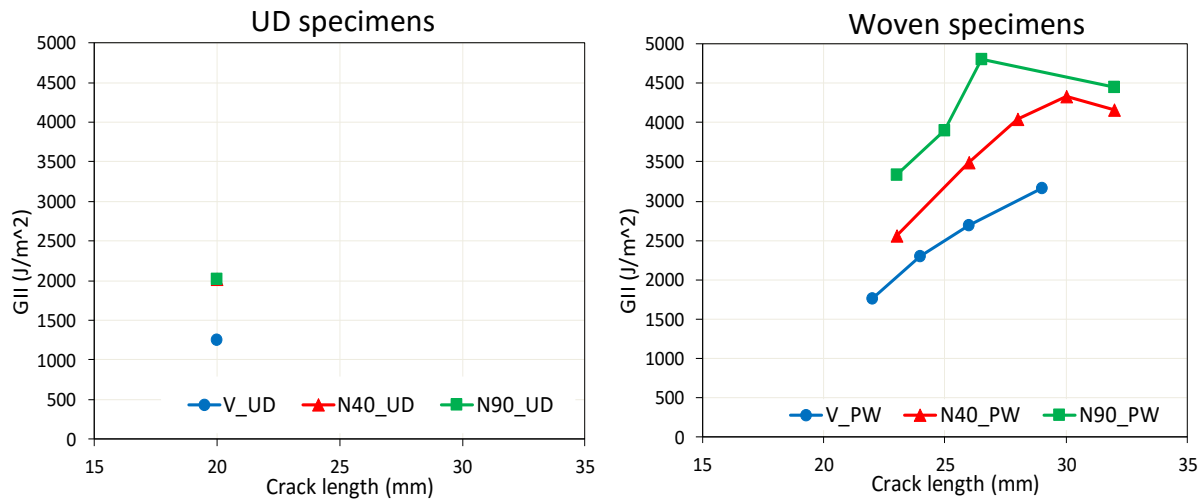

Fig 3-5 Representative R-curve for ENF tests
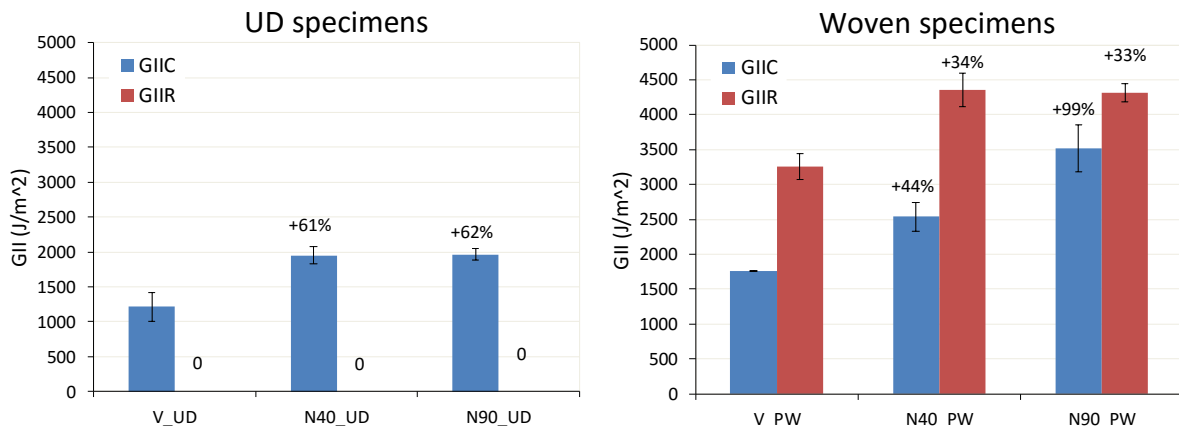
Fig 3-6 Initiation and propagation energy release rate for Mode II loading.

3.3.3   Micrograph analysis of the crack path

The results illustrated in the previous sections can be explained by micrograph analysis. By means of an optical microscope, images of crack paths have been captured to investigate the nanofiber's reinforcement mechanism. Photographs in Fig 3-7 show the crack paths of DCB PW V, NY$_{40}$ and NY$_{90}$ samples. Green lines indicate the nanolayer.

Fig 3-7 a shows the crack following a linear path, with very small deviations from an ideal straight line, and a few small extra fractures on the adjacent layers, as indicated by the purple arrows. Nanomodified samples, shown in Fig 3-7 b and c, instead, show a different behavior: while propagating, the crack deviates from the toughened, nanoreinforced interface, and is

forced to follow a longer, zig-zag shaped path, as pointed by yellow and red arrows. It will cause to break not only a larger amount of matrix, but also some of the carbon fibers belonging to the adjacent layers, thus requiring higher energy to propagate in comparison with pristine specimens. Furthermore, comparing Fig 3-7 b with c, it can be noted that the thicker nanofibrous mat covers almost the entire interlayer, filling also those areas that due to the woven nature of the fabric, present higher matrix content (the so-called resin pockets). The same cannot be said for the thinner interlayer, which only partially cover the interface. The thicker nanolayer can effectively link the two plies in which it is inserted along the entire interface. Therefore, crack propagation in PW NY_{90} specimens is constantly hindered by the nanointerlayer and forced to bifurcate and propagate through the carbon tow of adjacent layers.
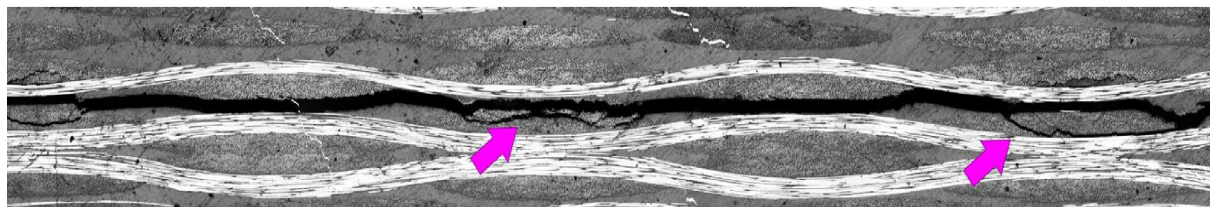
(a) Crack path in a DCB PW V specimen
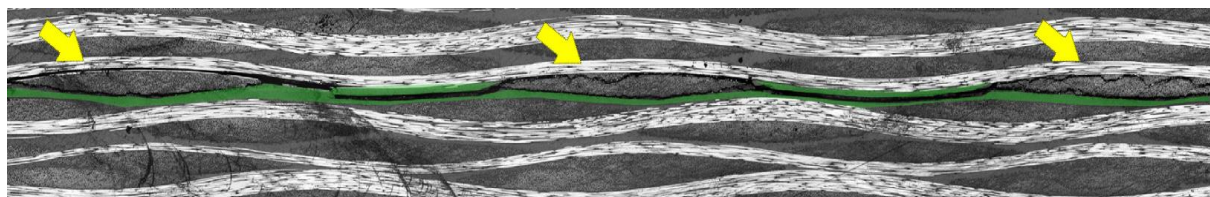
(b) Crack path in a DCB PW N_{40} specimen
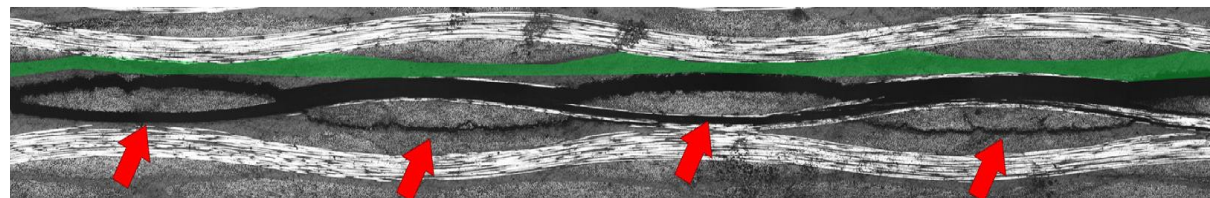
(c) Crack path in a DCB PW $N9_{0}$ specimen

Fig 3-7 Crack paths from DCB PW samples

Photographs in Fig 3-8, top to bottom, right to left, shows the crack paths of DCB virgin and nanomodified UD samples, and two main things can be observed:

- the crack, induced by the Teflon layer, tents to propagate through the nanointerlayer (Fig 3-8b), which allow the reinforcement to play an active role in hindering the crack initiation and increasing the fracture toughness at the onset. On the other hand, during the propagation stage, the crack deviates from the toughened region to the adjacent, not reinforced interlayer, propagating along the direction of the carbon fibers. The same would happen for PW laminates (see Fig 3-7b and c) if it was not for the more complex texture of the woven fabric, which hinder the propagation of the

crack inside the carbon layer and oblige it to stay in the nano-modified interlayer. This explains the ineffectiveness of the nanofibers on crack propagation inside UD laminates and their opposite effect on woven fabric;

- the different influence of the nano-mat thickness on the fracture toughness of UD and PW laminates can be explained comparing the two cross sections in Fig 3-7c and Fig 3-8b: UD laminates, having all the carbon fibers aligned along one direction, create a flat thin interlayer, while the woven nature of PW laminates creates a wavy thick interlayer. It is therefore necessary a thicker nanoreinforce, in PW laminates, to cover all the interface to make it effective against crack propagation.
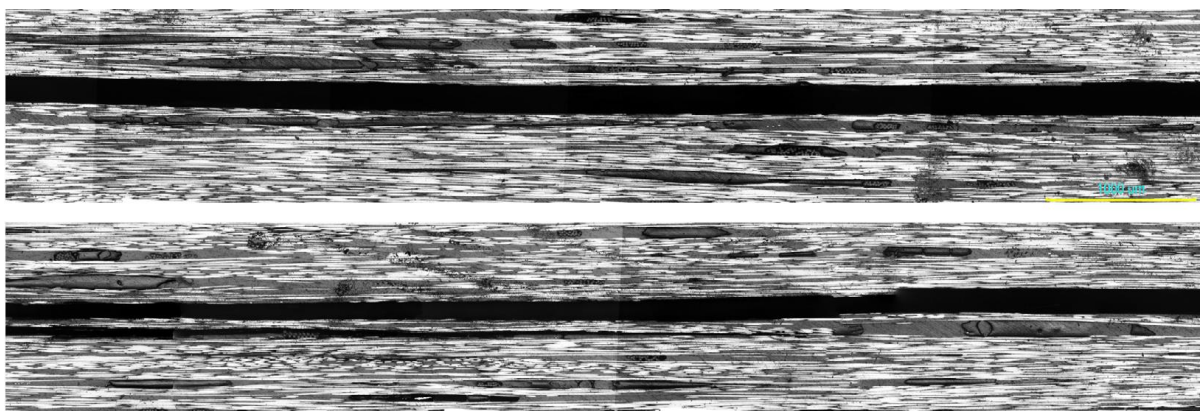
(b) Crack path in a DCB UD specimen
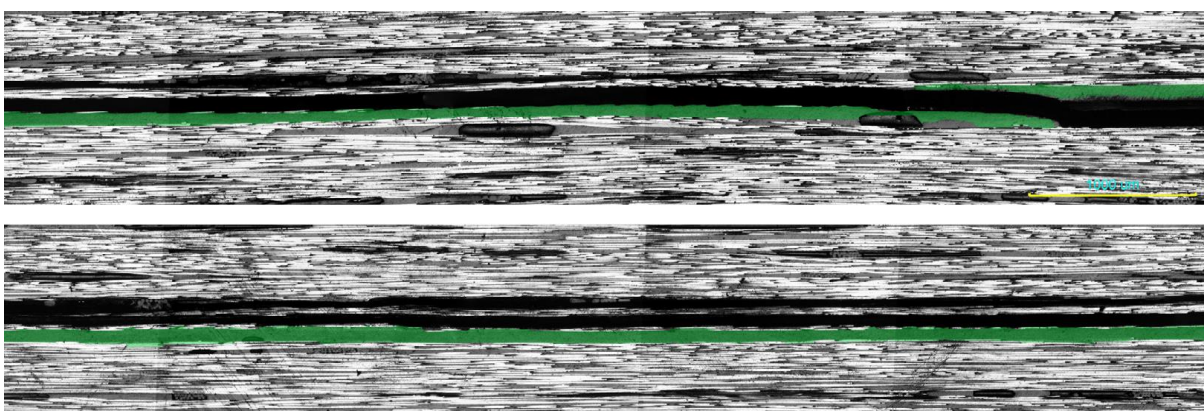
(a) Crack path in a DCB UD specimen

Fig 3-8 Crack paths of DCB UD samples. Crack start top right.

3.4 Conclusions

In this chapter, it has been an experimental study the effect of the thickness of a nanofibrous interlayer into plain wave and unidirectional epoxy-based composite laminates.

The results showed a significant improvement when nanofibers are employed under both DCB and ENF loading conditions for both the UD and PW configurations of laminate. In general better results have been found for PW samples, for DCB loads, and for thicker nano-reinforcement.

The increased critical energy release rates G_{IC} and G_{IIC}, proved that the presence of nanofibers hinder the crack initiation by rein-forcing the matrix. Furthermore, micrographs showed that, during the propagation stage, the crack in nanomodified samples is forced to break a larger amount of matrix and microfiber compared to virgin samples, requiring so higher energy to propagate; moreover the fracture toughness increases with the thickness of the nano-reinforce. UD samples are less affected by nanofibers due to the fact that the crack tends to cross the plies and so does not propagate in the same interface where the nanolayer is interleaved.

Eventually the micrographs explained the mechanical results, suggesting a strong interaction between the nature of the macro reinforcement (UD and woven) and the thickness of the nano reinforcement. In general, the nanoreinforcement increases the fracture toughness at the initiation for all the configurations, while the propagation stage is significantly dependent on the amount of the nano-reinforcement and on the nature of the macro one.

The effect of PVDF nanofibers on mode-I fracture toughness of composite materials

4.1   Introduction

In this study, the fracture behavior of carbon/epoxy laminates interleaved by polyvinylidene fluoride (PVDF) nanofibers is investigated.

So far, various kinds of polymeric nanofibers have been applied to increase the fracture toughness of composite materials: poly-sulfone (PSF) [90], Nylon 6 [83], Phenoxy [91], Nylon 6,6 [92]–[94], poly(e-caprolactone) (PCL) [95], polyvinylidene fluoride (PVDF) [96] and etc. Although several studies have been conducted for many of these nanofibers, only a few research papers have been reported in the literature about the toughening effect of PVDF on epoxy [95]–[97]. Zhang et al. [95] used three different electrospun nanofibers: PCL, PVDF, and PAN between composite layers; they compared their effect and considered their toughening mechanism. Their results showed that only PCL can toughen epoxy. Magniez et al. [96] employed low and high molecular weight PVDF for investigating its efficiency in mode-I and mode-II fracture tough-ness of carbon/epoxy composite materials. They showed that the use of both types of PVDF can increase mode-II fracture toughness but at the same time it slightly decreases fracture toughness in mode-I. Furthermore, they showed that molecular weight slightly affected the PVDF crystal forms and the morphology of the fractured surface; at the same time, it did not significantly affect mode-I and mode-II fracture toughness. The difference of the study of Zhang and that of Magniez is in the curing processes. In the first one [95], specimens were cured at 150 °C and so PVDF did not melt; on the other hand, in [96] the curing temperature was 175 °C, which caused the fibers to melt. Results showed that fracture toughness enhanced as the curing temperature increased and nanofibers melted.

The researchers in [95], [96] used a very thick nanofibrous mat (about 70 μm) and, as mentioned above, the curing temperatures in [95], [96] were below and above the PVDF's melting point, respectively.

Therefore, in this paper, it is shown that, by changing the thickness of the nanofibrous mat, curing and electrospinning process, the fracture toughness in mode-I can be increased by incorporating PVDF nanofibers. The effect of all these parameters is introduced in the following sections. The SEM pictures of the fractured interfaces will then be used to explain the role of the nanofibers in the interface.

4.2 Materials and method

4.2.1 Laminate and nanofiber fabrication

Carbon/epoxy prepreg twill 2/2 240 gsm (GG240-T2-IMP752) supplied by Impregnatex Composite Srl (Milan, Italy) was used as base composite material.

PVDF nanofibers were produced by electrospinning technique setting the process parameters as described in section 2.1.3. The mechanical and thermal properties of PVDF bulk material are reported in Table 2-2. A key point of this experiment is the melting point of PVDF, which is at 170-175 °C. The average fiber diameter was 500 ± 110 nm. Two nanofibrous mats with different thickness were produced: 30 and 60 μm.

The specimens were manufactured stacking 14 plies of prepreg woven fabric. A crack was initiated by inserting a 15μm Teflon sheet in the mid-layer of the specimens; PVDF nanofibers were placed in the same interface, following the procedure described in section 2.2.3. As shown in [96], if nanofibers melt, they are more effective than those which do not. Therefore the curing process should overcome the melting point of the PVDF, which is 165–170 °C, according to the supplier data sheet. For this reason, a prepreg that requires a high temperature curing process was chosen. In particular, the temperature followed a 4-step cycle: (1) from room temperature to 170 °C at 1 °C/min, (2) 1 h at 170 °C, (3) from 170 to 190 °C at 1 °C/min, (4) 20 min at 190 °C.

4.2.2 Mechanical test

The specimen dimensions are given by the ASTM D5528 [89] standard: width B = 20 mm, length L = 140 mm, nominal thickness t = 4.2 mm, and initial crack length a = 60 mm. Energy release rate for mode-I fracture testing (G_I) is obtained from the beam theory presented in section 3.2.2. It should be mentioned that for each configuration (reference and interleaved laminates) three specimens were fabricated and tested.

4.3 Results and discussion

4.3.1 Mechanical test and comparison with literature

Fig 4-1 illustrates the optical microscopy analysis of the side of the cured composite. As seen, the thickness of the nanofibrous membrane decreased significantly after the curing process.

The thickness of nanofibers shrunk from 30 and 60 μm before the curing, to 20 and 42 μm after curing for thin and think membranes respectively due to the high pressure and temperature reached during the curing process.

Fig 4-2 a shows the force-displacement curves of mode-I fracture tests for reference and nanomodified laminates (with thin and thick PVDF membrane). As seen, applying thin nanofibrous mat could increase fracture load in comparison with reference laminate, and the increase is proportional to the mat thickness. The average maximum load enhance is approximately 23% and 40% by interleaving thin and thick membrane of PVDF, respectively.
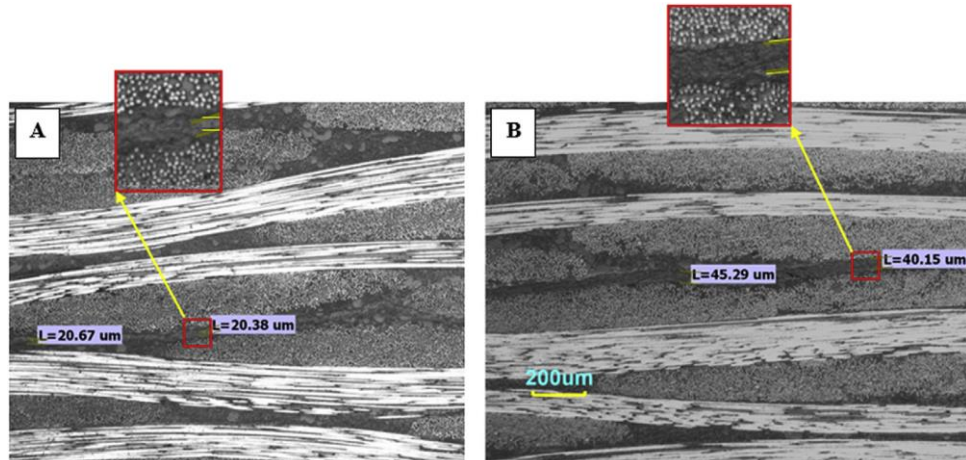
Fig 4-1 Cross section optical images after curing process: (A) modified laminate with thin PVDF membrane (B) modified laminate with thick PVDF membrane.

Fig 4-2 b shows the variation of mode-I fracture toughness during crack propagation for each configuration. For better considering the results, the energy release rate for mode-I fracture is reported in Table 4-1. Both the initiation and the propagation stages have been considered. As expected, the propagation fracture toughness is higher than the initiation one for all the configurations. At initiation stage, the GI increases 42% and 98% by using thin and thick membrane in comparison with the reference laminate respectively, and 36% and 73% in propagation stage respectively.
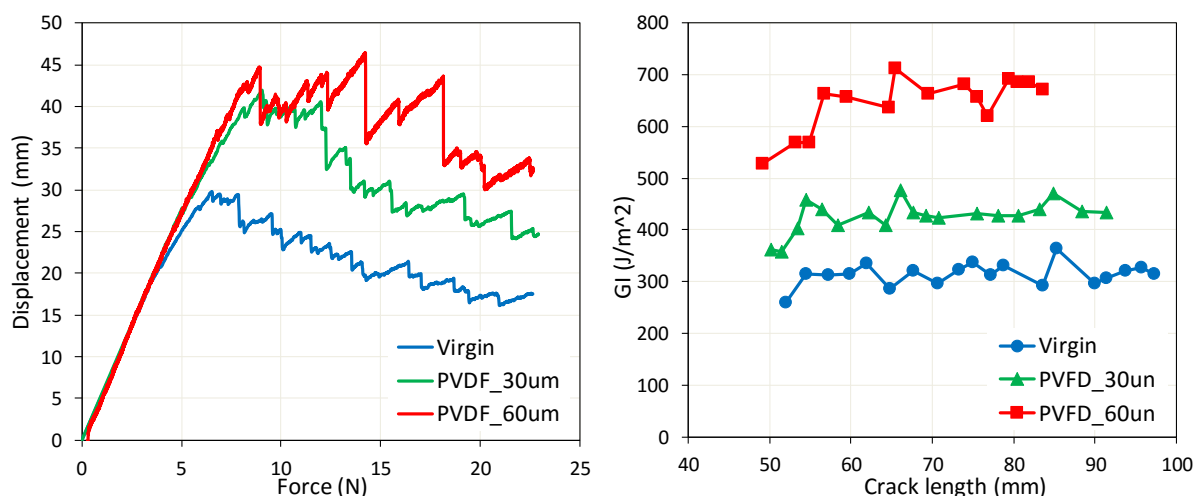
Fig 4-2 (a) Force-displacement and (b) mode-I fracture toughness-crack length curves for non-modified and PVDF thin and thick nano interleaved laminates.

Table 4-1 Fracture parameters obtained from mode-I fracture tests.

	Max Force (N)		G_{IC} (J/m²)		G_{IR} (J/m²)	
	Mean	Δ%	Mean	Δ%	Mean	Δ%.
Virgin	32.2 ± 2	-	254 ± 5	-	307 ± 17	-
PVDF-30 μm	39.5 ± 0.5	+ 23	362 ± 36	+42	418 ± 12	+ 36
PVDF 60 μm	45 ± 1.2	+40	503 ± 42	+98	531 ± 27	+73

These results are in contrast with those presented in Refs. [15,16] which showed that PVDF nanofibers cannot increase mode-I fracture toughness. The factors which play an important role when modifying composite interface with nanofibers are: the curing process and the membrane thickness.

Magniez et al. [96] cured the specimens at 150 °C for 10 min while the melting point of PVDF is about 165–170 °C and so the nanofibers were visible in the morphology of the fractured surface shown in the paper. Zhang et al. [95] used a different curing process: 125 °C for 1.5 h and 175 °C for 2 h, which caused the nanofibers to melt. The thickness of the nanofibrous membrane in both studies was about 70 μm. Correlating the results from literature: by increasing the curing temperature from 150°C (Maginez et. al.) to 175°C (Zhang et. al.), the effect of PVDF nanofibers on fracture toughness changed from -20% to 0% as mentioned above. Hence the curing process temperature should be higher than the melting point of PVDF.

This condition is necessary but not sufficient. Membrane thickness is also an important factor for toughening laminates with PVDF. Since PVDF nanofibers melt during the curing process, the matrix of the adjacent layers may find it difficult to reach each other if thick nanofibrous membranes is used, resulting in weak bonding. An evidence of this is shown by Magniez et al. [96] who considered the effect of PVDF in form of film and nanofibers. It was shown that GI of laminate modified with film is about 90% lower than that modified with nanofibers. This was because the PVDF film, having not porosity, has prevented from mixing the matrix of adjacent layers, while porosity of nanofibers let the resin flow and so during the curing the PVDF melted and mixed with matrix completely and in this way improved the fracture toughness. It can be stated that increasing the thickness over a certain value is not useful for toughening. The thickness of nanofibrous membrane in Refs. [95], [96] was about 70 μm while in this study the maximum thickness, after curing, was about 45 μm.

4.3.2 Fracture surface analysis

The morphology of fractured surface analyzed at the SEM microscope is shown in Fig 4-3. It is possible to highlight two regions: a brittle-fracture morphology on the lower side of the figure, and a ductile fracture region on the upper side. The brittle region is the area where the crack propagates in the fiber-matrix interface region, where there is only matrix; the ductile region, instead, shows that the crack propagated through the blend of melted PVDF and epoxy resin, resulting in plastic deformations. The toughening mechanism and energy absorption during the tests are closely related with plastic deformation [96]. The mechanism

of improving fracture toughness using PVDF nanofibers depends on plastic deformation of the ductile region, while non-modified samples consist only of the brittle fracture (without any or a little plastic deformation) [96]. The plastic constraint at the crack tip in modified laminates absorbed more energy in comparison with the reference laminates during crack propagation; which, it finally leads to an increase of fracture toughness.

An interesting phenomenon that has been observed during the test is the high stability of force-displacement curves in reference and modified laminates with a thin membrane, while the curves are strongly unstable in the laminates with thick membrane (Fig 4-2). Thicker plastic zones absorb higher energy. According to Fig 4-1, when the PVDF membrane thickness increases from 20 mm to 42 mm, it fills the space between fiber tow completely, increasing the size of the plastic zone. The mentioned instability of the measured force during the test for laminates with thick membrane is due to the increased toughness caused by nanofibers. When the plastic zone at the crack tip is big enough, it stops the crack propagation; increasing the force leads to an increasing of the stored energy, until a critical threshold value is reached, at which the crack abruptly propagates causing higher force drops.
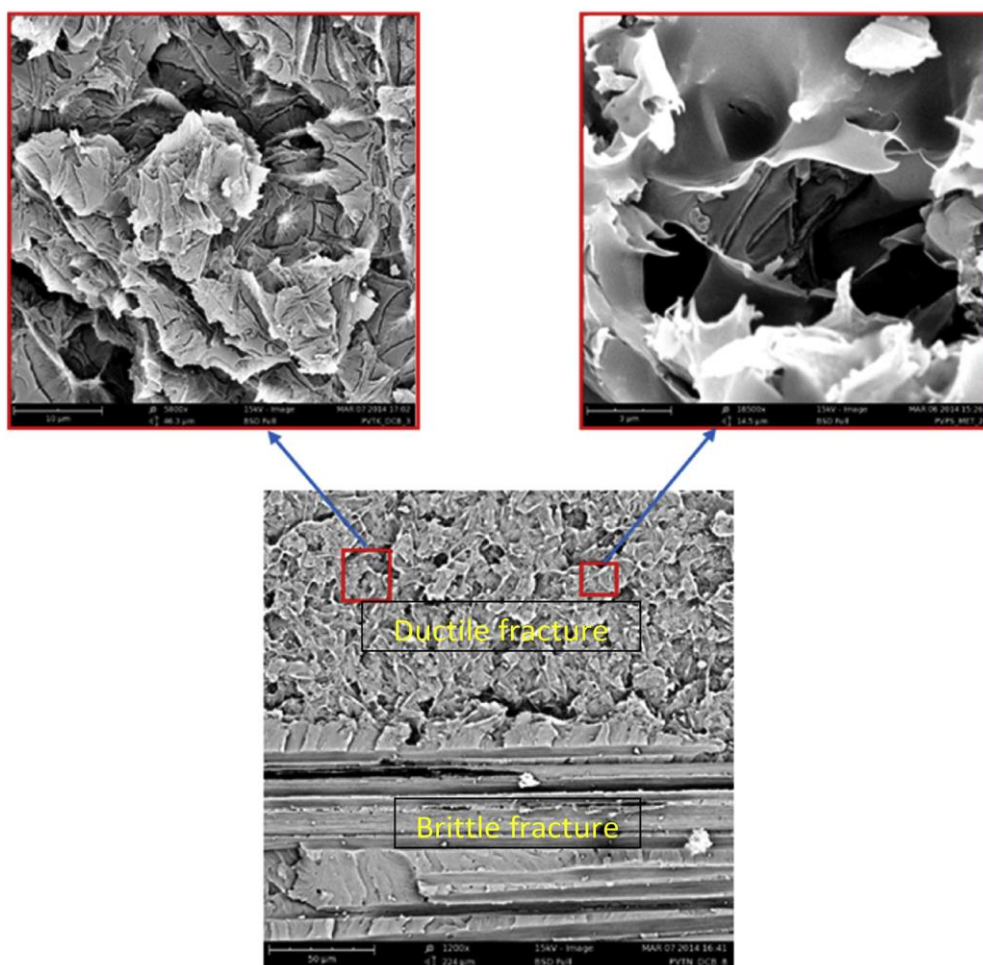
Fig 4-3 Morphology of fractured surface with two magnification (left: 10 mm, right: 3 mm

It is worth mentioning that some marks of nanofibers produced during the curing process can be seen in Fig 4-3. The formation of these marks can be described as follows. As a prepreg was used in this study, the epoxy was partially pre-cured by factory; hence at room temperature the epoxy is in a gel state (called B-stage). During the first curing cycle ramp (from 20 to 170 °C @ 1 °C/min), the epoxy started to be liquid again and so to penetrate the nanofibrous mat. Then during the plateau at 170 °C for 1 h, the epoxy partially crosslinked changing its state irreversibly from liquid to almost solid, while the PVDF nanofibers were still almost solid (PVDF has a melting temperature of 170-175 °C). Increasing the temperature from 170 °C to 190 °C the PDFV nanofiber started to melt and flow, leaving the marks at the position of the melted nanofibers among the solidified (cured) epoxy.

4.4   Conclusion

In this study, electrospun polyvinylidene fluoride (PVDF) nanofibers are used to increase mode-I fracture toughness (G_I) of carbon/epoxy laminates. Previously has been shown in literature that PVDF was not a suitable choice for increasing G_I, but this study proved that PVDF can enhance G_I. SEM pictures of the fractured surface showed that plastic deformation of the matrix and melting of PVDF play the main role in the fracture toughness enhancing process. The following results can be concluded from this study:

- Melting the PVDF nanofibers is an important factor to toughen the epoxy, but is not enough and other factors like thickness of nanofibrous mat should be also considered.
- Increasing the thickness of nanofibrous membrane leads to an enhancement on the toughness of laminates and causes an instability on force and crack propagation during the test. Thin and thick membranes could increase the fracture toughness 42% and 98%, respectively.
- As PVDF nanofibers melt during curing process, the toughening mechanism is due to plastic deformation during crack propagation; which was clarified by SEM micrograph analysis of the fractured surfaces.

Comparing the results obtained in this study with the results described in the previous one, can be drawn some general conclusions. The fracture toughness enhancement, on mode I at propagation stage, obtained by Nylon nanofiber interleaving is similar to the one obtained with PVDF nanofibers:

- PVDF: +42% and +98% for thin (30 μm) and thick (60 μm) nano mat, respectively;
- Nylon: +40% and +122% for thin (40 μm) and thick (90 μm) nano mat, respectively.

Note that the geometrical features of the nano and micro reinforcement are similar:

- the nanofiber diameters are 500 ±110 nm for PVDF vs 350-400 nm for Nylon
- the nano-mat thickness is similar for thin (30 vs 40 μm) and thick (60 vs 90 μm)
- the carbon fiber laminates have both a woven architecture (Twill for PVDF and Plain for Nylon) and similar ply thickness (240 g/m^2 for PVDF vs 220 g/m^2 for Nylon).

Hence the only major difference between the two experiments is the polymeric material of which the nanofibers are made (PVDF vs Nylon), which have different mechanical properties (Table 2-2). What in both experiments has dramatically influenced the enhancement of fracture toughness is the mat thickness. Therefore, it can be speculated that, at least for these two experiments, the key parameter is not the material of which the nanofibers are made but the thickness of the nano-mat. The reason is that thickness has to be higher than a specific value in order to effectively link the upper ply to the lower one, and therefore contrast the crack propagation.

An investigation on the fatigue based delamination of woven carbon-epoxy composite laminates reinforced with polyamide nanofibers

5.1 Introduction

The academic community produced accurate research on nanomodified composites, but some aspects still need to be further investigated: in particular the following experimental study aims to investigate nano interleaved laminates subjected to cycling loads, which is a topic studied by only few papers in literature [33], [98], [99], [100].

Bortz et al. [33] performed axial fatigue tests (tension, compression, tension dominated) on carbon nanofibers (CNFs) interleaved composites, showing for nanomodified samples 150–670% longer lifetime. They addressed their results to an increased interface density and to the damage shielding effect of the reinforce. Arai et. al. [98] also used carbon nano reinforcement, in their case they used multi-walled carbon nanotubes (MWCNTs) and measured propagation rate during Mode I fatigue tests. Their results show that the nanomodified interfaces extended the fatigue life and fracture toughness by 150% and 300% respectively. Similar results have been found by Zhou et al. [99] in both static and fatigue tests. Regarding laminates reinforced by polymeric nanofibers, at the present only Shivakumar et. al. in [100] studied their fatigue behavior at delamination. They used Nylon 6,6 to produce nanofibers instead of carbon, and performed a deep investigation on the effect of the nano interleave on unidirectional (UD) laminates under different loading conditions. On the fatigue side, they showed a significant increase on delamination onset life for nanomodified specimens.

However, the research on the delamination fatigue behavior of composite reinforced by polymeric nanofiber is not complete. There is lack of studies of the effect of the nanofibers on the fatigue behavior of laminates with a woven architecture, which as has been demonstrated in chapter 2 behave differently when are interleaved in laminates with a unidirectional architecture.

Moreover, whilst the fatigue behavior at the onset of the delamination of Nano interleaved UD laminates has been already investigated, there is lack of research on the effect of nanofibrous interleaves on crack propagation rate.

In the present chapter, the effect of interleaving electrospun Nylon 6,6 nanofibers in woven composite laminates is studied and tested under Mode I fatigue loading. The purpose is to assess the fatigue behavior to the onset of the delamination and the crack growth rate for virgin (V) and nanomodified (N) specimens.

5.2   Experimental

5.2.1   Sample preparation:

The international standard ASTM D5528 [89] has been used as reference for DCB specimen dimensions: 14 layers of 220 g/m² plain wave carbon-epoxy prepreg (GG204P-IMP503Z) supplied by Impregnatex Compositi Srl (Milan, Italy) have been stacked to manufacture 130x20 mm^2 specimens, with an initial crack a_0 of 45 mm long artificially created by interleaving a 30 μm thick PTFE film in the mid-interface. Nanofibers of Nylon 6,6 Zytel E53NC010 purchased from DuPont have been produced by electrospinning following the process detailed in Table 2-1. The final nano interleaves had areal density of 18 g/m^2, and were 50 ±10 μm thick; randomly distributed nanofibers had diameter of 520 ± 100 nm. N specimens had a nanofibrous layer in the mid interface. Post-processing and interleaving have been done following the procedures presented in section 2.2.3. Note that for each configuration, hence virgin (V) and nano reinforced (N), all the specimens were extracted from the same panel, both cured in the same batch. Final laminate's thickness was 3.5 ± 0.1 mm with no appreciable differences between V and N configurations. The estimated increase of weight for N samples was 0.34%. The optimized cure cycle presented in Fig 2-12 has been followed for both laminates types. Fig. 1 shows V and N interfaces at a magnitude of 5000x and the nano-fibers in N samples are clearly visible and intact, after the curing cycle.
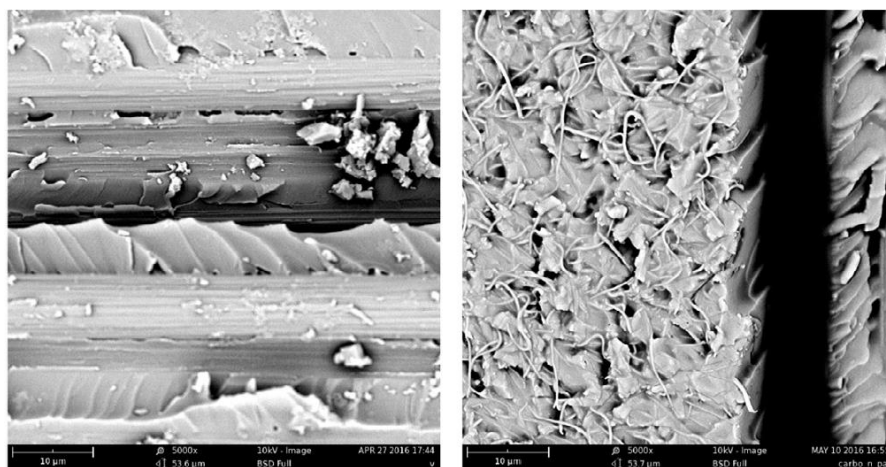
Fig 5-1 V (left) and N (right) interfaces

5.2.2 Static test

Static DCB tests have been performed in order to calculate fracture toughness at crack initiation (G$_C$) and propagation (G$_R$). The Modified Beam Theory (MBT) [89] has been used and the Eq. (5-1) was applied.

$$G_I = \frac{3F\delta}{2B\alpha} \qquad (5\text{-}1)$$

where F is the force, δ the crack opening displacement, B the specimen width, and a the crack length. Similar static test's conditions and results have been already presented in Chapter 1 (for V_PW and N40_PW) and have also been summarized here because the present experimental campaign is directly affected by those results. The initial fracture toughness G_{IC} was evaluated according to the 5% compliance deviation or maximum load point of the loading-displacement curve [89]. The fracture toughness resistance (at propagation stage) G_{IR} was evaluated on the R-curve as average value, when after the initiation, it becomes nearly constant.

5.2.3 Fatigue life test (Wöhler curve like)

The Mode I fatigue delamination growth onset test was carried out, in accordance with the ASTM D6115 [101] standard. All fatigue tests were performed in displacement control, at a frequency of 1 Hz with a fixed loading ratio: $R = \delta_{min,n}/\delta_{max,n} = P_{min,n}/P_{max,n} = 0.3$. At each *n-cycle*, the maximum (minimum) value of the displacement and load, δ_{max} and P_{max} (δ_{min} and P_{min}) were recorded. The use of an uniball-like gripper avoided any undesired in-plane loads (see Fig 5-2).

The imposed displacement limits of the fatigue tests have been set based on the results of the static tests. Having the static and fatigue specimens the same configuration, using the beam theory, the crack opening displacement is obtained by the ratio between the desired initial $G_{Imax,0}$ and the critical static G_{IC}. The formula is shown in Eq. (5-2):

$$\delta_{max} = \sqrt{\frac{G_{Imax,0}}{G_{Ic}}} \left(\frac{a_0}{a_c}\right) \delta_c \qquad (5\text{-}2)$$

where δ_{max} is the maximum crack opening displacement, $G_{max,0}$ is the G_I at which the tests started, a_0 is the initial crack length, and a_c and δ_c are the critical crack length and crack opening displacement respectively, determined from the static tests. The fatigue test was stopped when the compliance of the DCB specimen:

$$C = \frac{\delta_{max,n} - \delta_{min,n}}{P_{max,n} - P_{min,n}} \qquad (5\text{-}3)$$

was increased by 5%. The related fatigue delamination onset life, *N$_{5\%}$* (equal to the cycles number achieved during the test) was then recorded.

The same procedure was repeated for each laminate type on at least 6 specimens at different value of $G_{Imax,0}$, keeping constant the loading ratio *R=0.3=cost*. The results were summarized in a diagram $G_{Imax} - N_{5\%}$ showing the relationship between the cyclic strain energy release rate and the number of cycles to the onset of the delamination growth.
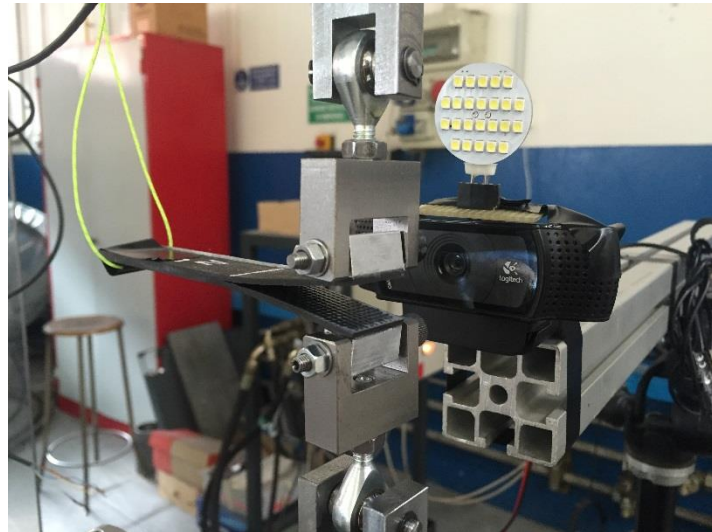
Fig 5-2 Mode I fatigue test setup.

5.2.4 Crack-growth rate test (Paris' law)

In this case, the aim is to determine the crack grow ratio of nano interleaved composites, for an international standard which does not exist. Authors used the international standard ASTM D6115 [101] for fatigue delamination growth onset for composite laminates, and the ASTM E647-15 [102] for the fatigue crack growth rates for homogeneous materials.

In order to evaluate the reinforce effect of the here developed nanofibers, authors consider enough performing three tests for each configuration. This assumption has been confirmed valid by the narrow error margin of the experiments compared to the data range of the experiments (Fig 5-3).

A sharp crack was naturally induced by pre-cracking the specimens at fatigue loading ($R = \delta_{min,n}/\delta_{max,n} = 0.3$ and $G_{Imax,0} = 50\% \, G_{IC}$) until the artificial crack propagated 1 mm. The imposed displacement limits of the fatigue tests have been set on the basis of the results of the static tests.

The tests have been conducted under displacement control, at a load frequency of 3 Hz to avoid any heating, with a loading ratio R equal to 0.3, for 500 k cycles. $G_{Imax,0}/G_{IC}$ has been set equal to 0.85, following other authors' experience [103]; this allows to speed-up and record the complete behavior of crack propagation [104]. The imposed displacement limits δ_{max} of the fatigue tests have been set based on the results of the static tests by using Eq. (2). Different values of δ_{max} have been calculated for each configuration due to different values of G_{IC} for V and N specimens.

For each cycle maximum and minimum load and displacement were registered; crack length was measured with a resolution of 0.5 mm during the test by a high-resolution camera facing the side of the specimens.

Outcome of the dynamic experiments were the da/dN vs. G_{Imax} curves for V and N configurations; where: a is the crack length, da/dN the crack propagation rate and G_{max} the energy release rate of the material calculated at the peak load of each cycle. Researchers have debated the use of G_{Imax}, G_{Imin}, ΔG_I or $\Delta\sqrt{\Delta G_I}$ for fatigue tests of composites [105]. In the cycle range here considered ($N \leq 10^5$), for investigating the effect of interleaved nanoreinforce, G_{Imax} is the most appropriate choice.

The crack propagation rate curves were determined based on compliance C (see Eq. (3)) method proposed in [106]. Images of the crack length were collected throughout the experiment on a logarithmic base: one photograph at each cycle for the first 10 cycles; one photograph every 10 cycles within the following 100 cycles; one photograph every 100 cycles within the following 1000 cycles; one photograph every 1000 cycles for the following 10,000 cycles; finally, a photograph every 10,000 cycles until the end of the test. The relation between the specimen compliance and the crack length has been derived based on the Eulero–Bernulli beam theory [107] and is shown in Eq. (5-4):

$$a/2H = \alpha_0 + \alpha_1(BC)^{1/3} \tag{5-4}$$

where 2H and B are the sample thickness and width, respectively, and α_0 and α_1 are fitting coefficients function of the elastic modulus of the laminate. Each photograph, and therefore each crack length, were related with the corresponding compliance to build the $a/2H$ vs $(BC)^{1/3}$ chart. Then, α_0 and α_1 coefficients for each specimen were obtained by linear regression.

Hence, the crack length at each cycle has been determined by reversing Eq. (5-4). Then, da/dN throughout the tests is evaluated through centered moving average and the result is plotted in Fig 5-3. The energy release rate calculated at the peak value of each cycle (G_{Imax}) is determined using Eq. (1). Results are reported in Fig 5-2. By combining the last two graphs, the da/dN vs G_{Imax} plots can be assembled.

It is worth mentioning that data has been filtered two times during the process to gain smoother results. Data have been divided into 4 groups: group I data from $N \leq 10^3$; group II data from $10^3 \leq N \leq 10^4$; group III data from $10^4 \leq N \leq 10^5$; group 4 data from N $N \geq 10^5$. Compliance and crack length have been evaluated at each cycle and then filtered and reduced using moving centered average with variable span (20, 100, 1000, 10,000 for group I, II, III and IV, respectively). da/dN was then calculated by discrete centered derivation and filtered by a moving centered average with a span of 20.
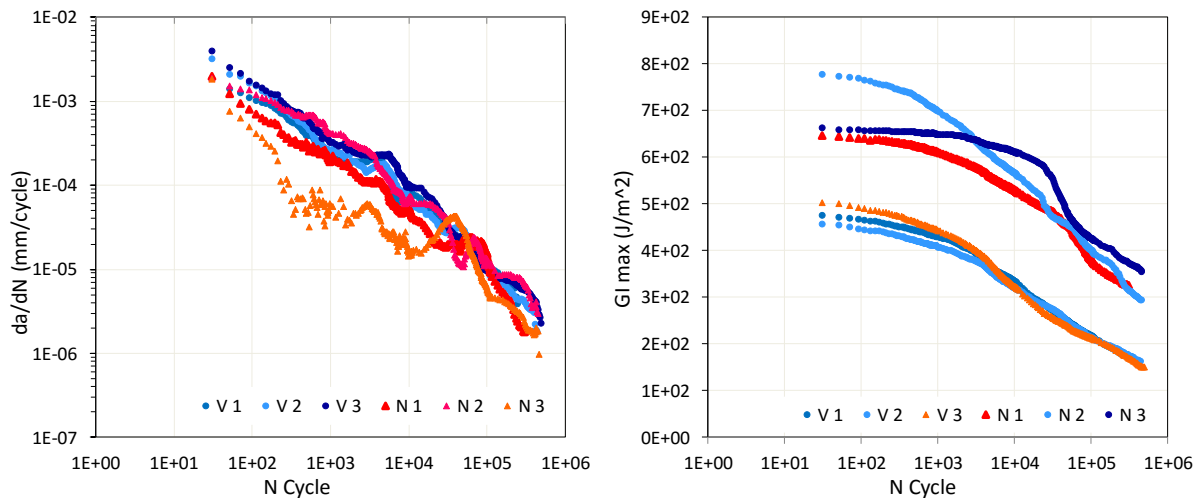
Fig 5-3 Crack growth rate and G_{max} vs N for virgin (V) and nano-modified (N). 1,2 and 3 identify the specimen number.

5.3 Mechanical test results

5.3.1 Quasi-static fracture toughness

Fig 5-3 summarizes the results of the static tests. Force–Displacement curves for each specimen and the resultant R-Curves for each configuration are shown in Fig. 3a and 3b, respectively.
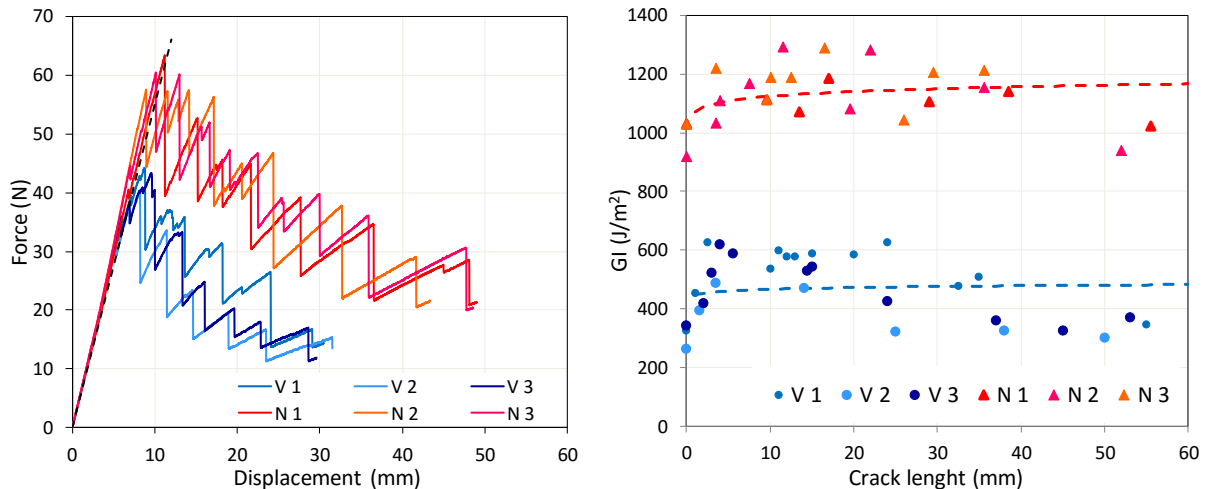
Fig 5-4 (a) load-displacement curves for reference (V) and nano-interleaved (N) DCB specimens; (b) mode I interlaminar fracture toughness as a function of the delamination propagation length (Δa=a-a0) for V and N.

Similar static tests results have been already presented and discussed in Chapter 3, showing a significant improvement in force and energy release rate due to the interleaved nanofibers. The fracture toughness is increased at both crack initiation and propagation ($G_{IC} = +137\%$ and $G_{IR} = +124\%$. respectively), and the crack propagates stably for longer than 50 mm, as shown by the R-Curves of Fig 5-4. Therefore, nanofibers' toughening effect is also detected at crack propagation, anticipating improvement of performances under fatigue loading condition, where the crack propagates for around 1 mm for the fatigue growth onset and longer than 10 mm for the crack-growth ratio test.

As observed in Chapter 3 the same is not possible in UD laminate, where the crack diverges from the toughened interlayer. This can explain why Shivakumar [100] noticed a decrease of the toughening effect at propagation stage (G_{IC}=150% vs G_R=+30%) of Nylon 66 nanofibers, interleaved in unidirectional laminates, which than impacted the fatigue results.

Moreover, the static G_{IC} values have been used into Eq. (2) to set-up fatigue test parameters.

5.3.2   Fatigue life at the onset of the delamination

The fatigue test results are plotted, as points, in the diagram maximum energy release rate G_{Imax} versus delamination onset life $N_{5\%}$ of Fig 5-5. Usually, the stress-fatigue life relationship is described by a power law equation. A similar law, suggested by O'Brien in [108], was found to fit very well with the experimental data of the present work:

$$G_{Imax} = G_{IC} * N^{-m}$$ (5-5)

where G_{IC} is the fracture toughness at initiation, obtained for the quasi-static test. However, the equation expressed in this form does not allow an easy evaluation of the statistic confidence of the model so estimated. Therefore Eq. (5-5) was linearized, by expressing it in logarithmic form:

$$\log N = A + B * \log G_{Imax} \quad or: Y = A + B * X \quad with: Y = \log N \ and \ X = \log G_{Imax}$$ (5-6)

And the experimental data were plotted in a log-log diagram. The curve of Eq. (5-6) was extrapolated by means of the maximum Likelihood method and the confidence bands (at 95% of probability) were computed following the procedure described in ASTM E739 [109]. Then the model, with its confidence bands, was transformed back into the original form of Eq. (5-5) and plotted in the graph of Fig 5-5.
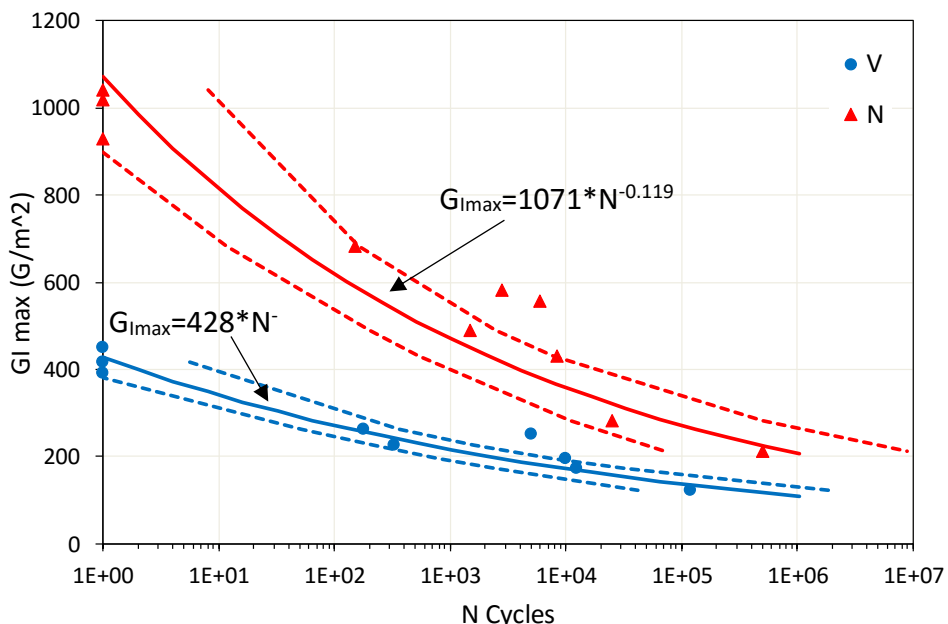
Fig 5-5 DCB Fatigue diagram (G_{Imax}- $N_{5\%}$) at a constant load ratio R=0.3, for virgin (V) and nano-interleaved (N) laminate

It is graphically clear that the model fits very well to the trend of the experimental results. However, the width of the confidence bands is large because of the high scatter of the experimental data, typical of fracture tests conducted on composite material. The fatigue life equations, extrapolated for the virgin and the interleaved laminates, are $G_{Imax}= 428*N^{-0.099}$ and $G_{Imax}= 1071*N^{-0.199}$, respectively. The fatigue curve of the nano-interleaved laminate begins (at $N=0$) from an energy release rate ($G_{Imax}= G_{IC}$) 2.5 times higher than the virgin one, but then it decreases faster (m coefficient of Eq. 2). However, it is clear that the presence of the nanofibers enhances the delamination fatigue onset life. The threshold energy release rate (estimated for $N=10^6$) of the nano-interleaved laminate is 90% higher than the virgin laminate ($G_{th-V}=109$ J/m^2 vs $G_{th-N}=207$ J/m^2).

5.3.3 Crack-growth ratio

The log–log plot in Fig 5-6 shows the crack propagation rate vs. maximum energy release rate outcome of the fatigue tests, determined with the method proposed above for each specimen. The straight lines represent the stable-growth propagation phase of the Paris law and are obtained by a linear interpolation of the da/dN vs G_{max} scatters in a log–log plot. Those lines, straight in the log–log plot, would be power laws in a linear–linear plot, shown in the form shown in Eq. (5-7) [110].

$$\frac{da}{dN} = AG^n_{max} \tag{5-7}$$

where A and n are determined by the curve fitting of the experimental data and have still unclear physical meaning [105].
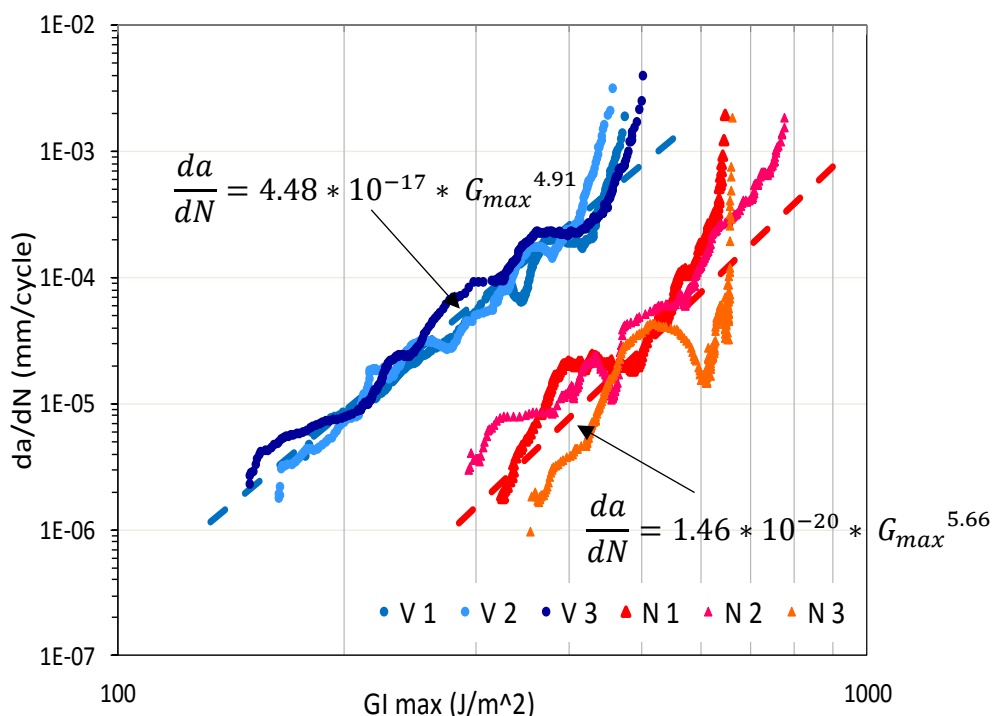
Fig 5-6 da/dN vs G_{max} plots for V and N specimens

The graph shows that for a given stress G_{max}, cracks in nanomodified interfaces propagate slower than in virgin samples, and that for a given propagation rate, nanomodified samples can be loaded with higher stress.

As example, for $da/dN = 5\ 10^5\ mm/cycle$, V and N can be loaded with 287 and 565 J/m^2, respectively, showing that the N load almost doubles that of V samples. In the da/dN range in common between the two configurations, N samples can be loaded with 46–55% higher load. Focusing on solicitation, at $G_{max} = 400\ J/m^2$, the crack propagation rates are 2.4 10^4 7.9 10^6 *mm/cycle* for *V* and *N* samples, respectively; showing that the cracks in N interfaces propagate 30 times slower than those in virgin ones. In the G_{max} range common at the two configurations the ratio among propagation rates spans from 36.4 to 27.2.

5.3.4   Comparison of experimental results with available data in literature

Having assessed the effectiveness of the polymeric nanofiber interlayer for the enhancement the fatigue life to the mode I delamination growth onset and crack-growth ratio, it is interesting to show how this study compares with others within this topic.

Shivakumar [100] performed a deep investigation on Nylon 6,6 nanomodified UD laminates, under mode I static and fatigue loading to the onset of the delamination. The fatigue life curves, presented by Shivakumar, show a completely different trend than the one presented here (see Fig 5-3): in [100] both curves for virgin and nano-modified laminates decrease monotonically and they tends to converge exponentially in the proximity of the fatigue threshold life (10^6 cycles); while the ones presented here decrease asymptotically and remains still well separated at 10^6 cycles. Comparing the results at the fatigue threshold life: Shivakumar reports an increase of 67% by nanofiber interleaving while in the present paper the increase is of 90%. The cause of this discordant behavior at fatigue life is the primary reinforcement architecture of the laminate (unidirectional vs plain woven) previously explained for static loading in Chapter 3.

The only work studying crack propagation of nanointerleaved composite laminates is [98]: authors used MWCNT as interleaving material to increase Mode I fracture toughness, and recorded a ΔG in the range of 104 ÷313 J/m^2, and an increase in G$_R$ comparable to the result of this work. However, they noted a lower reduction of crack propagation rate (10÷2 times vs. the 36÷27 shown here) and also a 1 to 5% increase in specimen's thickness, with the risk of reducing the in-plane mechanical properties of the laminate [111]. Furthermore, their study could not find clear evidence of the reinforcement mechanisms, which is instead shown in section 3.3 and section 3.4 of this study.

5.4 Analysis of the crack path and fracture surfaces

5.4.1 Micrograph analysis of the crack path

Crack path at the delamination growth onset:

A micrographic analysis was performed to better understand the toughening mechanism of the Nylon nanofibers at the delamination growth onset (see Fig 5-7). For both laminates, crack starts from the tip of the Teflon sheet, positioned in the mid-interlayer. Then under the cyclic loading, the crack propagates about 1 mm (which correspond to a compliance increase of 5%). In case of the virgin laminate the crack propagation is constrained by the woven architecture of the adjacent plies to propagate through the non-hindered interlayer. For nano reinforced laminates the crack is forced to propagate through a narrow region between the nano reinforced interlayer (which is tougher then the virgin one) and the adjacent ply (reinforced by the micro reinforcement architecture) and this slows its propagation.
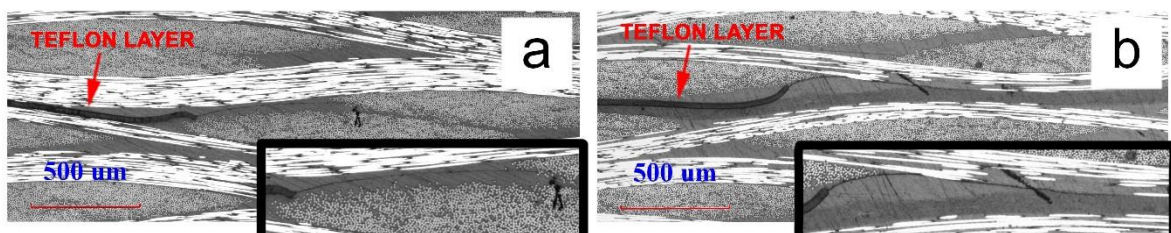
Fig 5-7 Micrograph analysis of the fatigue onset delamination for: (a) Virgin laminates and (b) nano-interleaved laminates.

Crack path development during crack-growth ratio test:

Fig 5-8 shows the crack path in a virgin specimen. It is widely recognized that cracks do not move across plies in traditional laminates with a woven architecture. Accordingly, the crack path in virgin specimens shown in Fig 5-8, has been found to always propagate within the same interface.

Fig 5-9 shows a different scenario for nanomodified interfaces. The micrographs suggest a double-stage reinforce mechanism:

- the image at the top of Fig 5-9 presents the first few millimeters of propagation, at the beginning of the test. At this stage, the crack (identified by green arrows) propagates in the same interface where it has been initiated, as expected, and the nanolayer keeps it confined in a narrow region, between the ply and the nanofibers. The right end of the first image shows that a second crack appears (identified by purple arrows). The nanofibers, reinforcing the interface, encourage the development of a second crack in a lower weaker layer not reinforced by nanofibers. The new crack is initially smaller and thinner compared to the main old one; the second image shows that the old cracks fades away while the new one grows larger. The last image shows that the original crack has arrested and the fracture has continued to propagate in a lower layer of the sample;

- The main image in Fig 5-10 shows a cross-section of the cracked sample: it can be observed that the crack front crosses the tow in several points, and has a complex morphology. Fig 5-9 itself could not explain why the fracture properties of the nanomodified samples increase once the crack propagates in a non-nanomodified interface; Fig 5-10, instead, suggests that the crack crosses different planes at the same time through its width, involving the nanomodified toughened interface, as shown by the red arrows in the two zoomed particulars.

It can be concluded that at the early stage the crack is confined between the toughened nanomodified interlayer and the carbon fibers, bouncing up and down between the two, and requiring higher amount of energy to propagate compared to a V interface; at a later stage, nanofibers force the crack to propagate in different planes, wide and thick wise, hindering the propagation of the fracture.
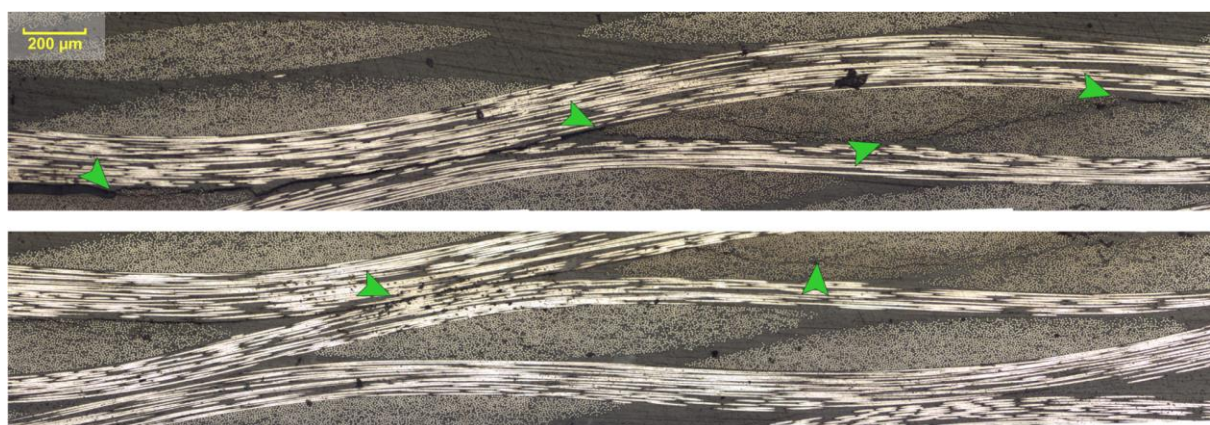
Fig 5-8 Side view of the crack path in a Virgin specimen. Read the figure from left to right, top to bottom.
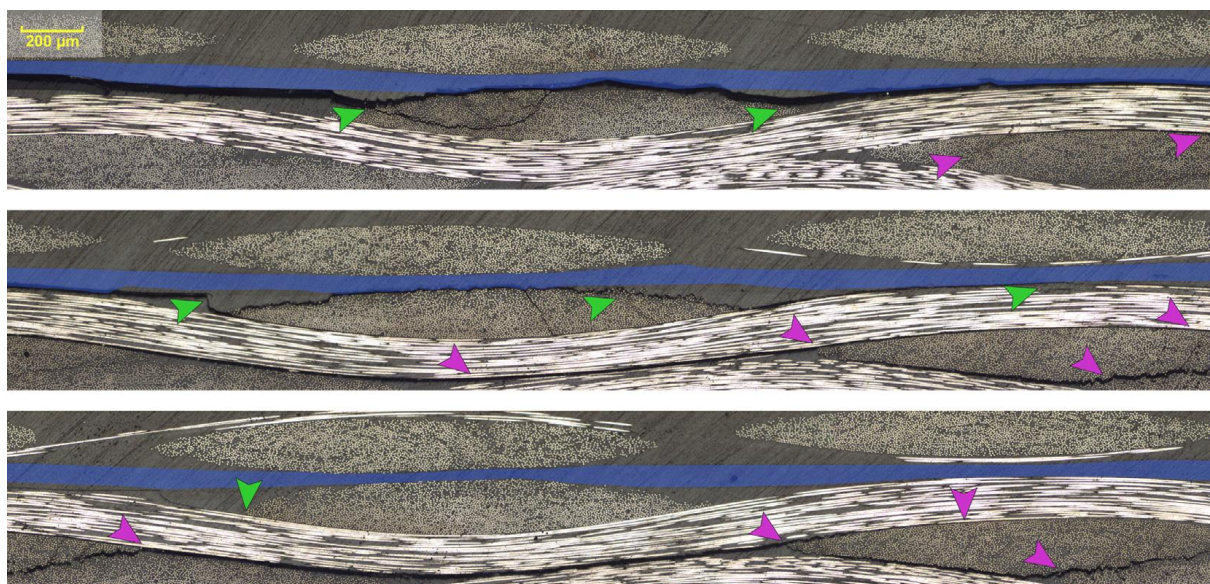
Fig 5-9 Side view of the crack path in a nanomodified specimen. Read the figure from left to right, top to bottom. Nanofibers are highlighted in blue.
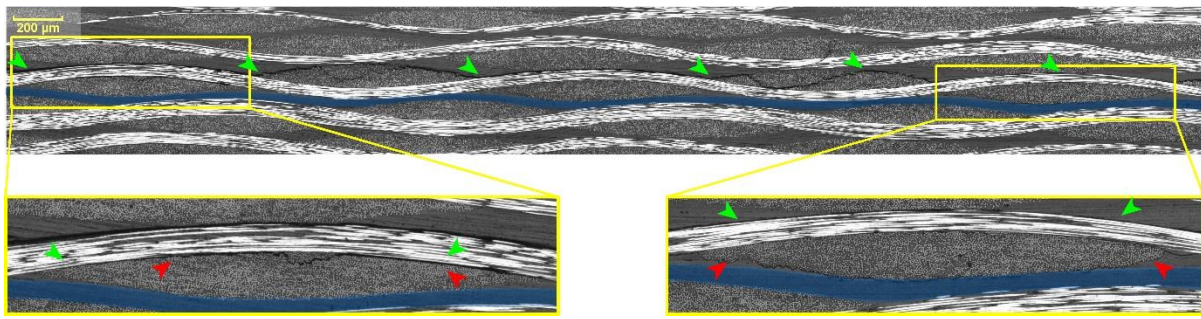
Fig 5-10 Crack front in a N specimen. Nanofibers are highlighted in blue.

5.4.2 SEM analysis of the fracture surfaces:

Fig 5-11 shows the fracture surfaces of the crack-growth ratio specimens, captured with by SEM microscope at two different magnitudes: 300x and 3000x.

SEM images provide evidences to support the thesis of the nanofiber toughening the interface. 300x pictures (Fig 5-11 a and c) present a general view of the fracture surfaces: in V samples the crack appears to propagate mostly through the matrix while in N being the matrix tougher the crack try to propagate at the fiber-matrix interfaces removing completely the matrix form the carbon fibers of the tow. Most importantly the images of V shows a single fracture plane, as the crack propagates linearly in the very same interface. On the contrary, the N surface presents several fracture planes, as the fracture had to move up and down to find the path of minimum resistance, increasing the fracture surface and consequently also the energy spent to propagate.

At a higher magnitude (Fig 5-11 e) nanofibers can be clearly seen. They keep the matrix consolidated, forcing the crack to propagate trough the matrix-carbon fiber interface and then divert in the tow.

SEM images confirmed the fracture mechanisms described above: nanofibers are able to toughen the matrix they are inserted within, hindering the crack propagation. Nanofibers holds the matrix together, avoiding the brittle fracture typical of a non-nanomodified interfaces, forcing the crack to propagate in non-reinforced interfaces.

(a) V at 300x

(b) V at 3000x

(c) N at 300x

(d) N at 3000x
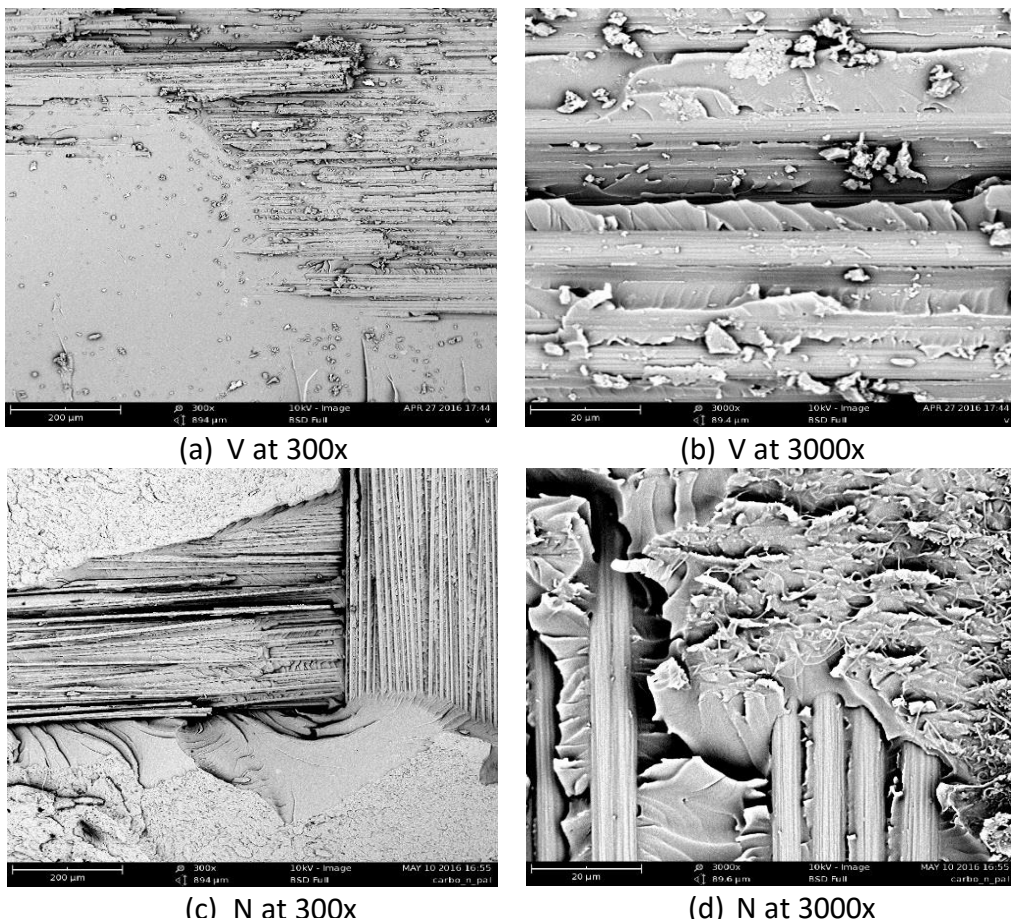
Fig 5-11 Fracture surfaces.

5.5   Conclusion

The Mode I fracture toughness of woven laminates interleaved with Nylon 66 nanofibers was investigated at mode I fatigue loading.

Results show that at fatigue, the presence of the nanofibers enhance the fracture toughness to the onset of the delamination, increasing threshold energy release rate (evaluated at 10^6 cycles) of 90%.

Crack growth ratio tests revealed that nanoreinforced laminates can sustain higher loads for same propagation speed (G_{imax} 96% higher for N at $5*10^5$ mm/cycle). In other words, for a given crack propagation rate, nanomodified samples can withstand much higher loads. Fatigue tests also showed that for values of G_{max} in the considered range, the crack in a nanomodified interface propagates several times slower than in a virgin one (from 27 to 36 times slower).

Micrograph analysis proved that nanofibers act as matrix reinforcement and force the crack to propagate through different interfaces, causing a sensible increase of the energy needed to propagate. SEM images demonstrated that the nanofibers hold the matrix together whilst forcing the crack to move away from the nanomodified interface.

Low Velocity Impact Damage assessment of GLARE fiber-metal laminates interleaved by Nylon 6,6 nanofiber mats

6.1 Introduction

Glass Laminate Aluminum Reinforced Epoxy (GLARE) is a lightweight hybrid composite material consisting of alternating aluminum sheets bonded to glass-epoxy prepreg layers, which belongs to the family of Fiber Metal Laminates (FMLs) developed at Delft University of Technology [112]–[114]. The main aim of producing these advanced composite materials is to have the best properties of both composites and metals, i.e. the superior fatigue and fracture characteristics of fibers and the plastic behavior and durability of metals [115]. Hence, GLAREs are a suitable option for aircraft structures and have been used extensively in recent years. Aerospace structures are frequently exposed to impact loadings which are caused by sources such as: runway debris, hail, maintenance, dropped tools, collisions between service cars or cargo and the structure, bird strikes, etc. [116]. The impact analysis of GLAREs during the design process is therefore important. Due to the dissimilarity between the composite lamina and the metal sheet, the interface properties are the most important issue in GLARE performance. The present study deals with the matrix toughening in the GLARE by interleaving nanofiber mats in order to achieve interface property improvement.

During the last two decades, several attempts have been devoted to the impact response investigation of FMLs subjected to low velocity [117]–[121] and high velocity impact loading [122]. Studies confirm that although GLARE impact damage resistance is better than its individual constituents i.e. aluminum and glass/epoxy composites, the poor strength of the lamina's interfaces causes failure modes such as delamination and debonding [119], [120], [123]–[125]. In order to solve this issue and therefore increase the impact resistance of GLAREs, two different approaches have been adopted by the scientific community: lay-up optimization [119], [120], [125] and matrix renforcement [126].

Regarding the lay-up optimization technique, they concluded that GLARE made of cross-ply orientation provided better impact resistance than GLARE with unidirectional plies. Although this technique sounds promising, the stacking sequence is often constrained by the in-plane loads that the structure must bear.

Hence, when it is not possible to modify the lay-up, another option, to limit the delamination and debonding, is matrix reinforcement. To the best of the authors' knowledge, only one scientific study by Zhang et al. [15] reports the application of this technique on GLAREs. They investigated the influence of multi-walled carbon nanotubes (MWCNTs) on the flexural property and the impact performance of GLAREs, through three-point bending and drop weight impact tests. An increase of 40.3 % of flexural strength and 24.8 % of elastic modulus compared to the plain GLARE was achieved by adding 0.5 wt% of MWCNTs as matrix reinforcement. In addition, in comparison with pure epoxy bonded GLARE, the modified GLAREs generally showed improvement of impact resistance and the improvement was more obvious at low concentration of MWCNT due to better dispersion of nanotubes in the resin. It is noteworthy that the results showed high scatter caused by the non-controlled and non-constant thickness of the laminate which affects the laminate moment of inertia and therefore the flexural strength and elastic modulus measured.

In this research, in order to mitigate the detachment between aluminum sheets and glass/epoxy layers in GLAREs, we proposed the matrix toughening approach by interleaving nanofiber mats between metal sheet and fiber lamina for the first time. This idea is inspired by our previous studies on the positive effect of nanofiber mats to increase the delamination strength on composite laminate [127]–[130].

Morover, Akangah et al. [131] conducted a series of impact tests with impactor velocity ranging from 2.0 to 4.0 m/s to consider the effect of Nylon 6,6 nanofiber interleaving on the impact damage resistance of carbon/epoxy composite laminates. It was shown that Nylon 6,6 nanofiber interleaving reduced the growth rate of impact damage to one-half with respect to height and reduced impact damage growth rate from 0.115 to 0.105 mm^2/N with respect to the impact force. Shivakumar et al. [132] carried out impact and mode I fracture mechanics tests on virgin and nano-modified specimens. It was demonstrated that the nano-modified samples exhibit a significant increase in damping, fracture toughness, delamination strength and a reduction in impact damage size.

According to the literature survey, the impact resistance of GLARE is limited by the interlaminar fracture toughness which causes delamination and debonding damage. In addition, nanofiber interleaving technique is well-known to increase the damage resistance of laminated composites. Hence, in the present work a novel GLARE toughened by interleaving Nylon 6,6 nanofibrous mats is presented to improve interfacial properties of traditional GLARE.

To achieve the purpose, impact tests were carried out on two types of specimen: 1- plain GLARE (virgin) and 2- nano-modified laminates. Impact response and post impact damage assessment of tested specimens are discussed in detail. The results show that interleaving the Nylon 6,6 nanofibrous mats increases the interlaminar shear strength of nano-reinforced samples which causes a significant improvement in damage resistance. It is noteworthy that

to the authors' knowledge, the study of FML's impact property improvement by polymeric nanofibers has not been previously published elsewhere.

6.2   Experimental procedure

6.2.1   Electrospun nanofiber mat

Nanofibers of Nylon 6,6 Zytel E53NC010 purchased from DuPont have been produced by electrospinning following the process detailed in Table 2-1. The final nano mat had areal density of 10 g=m2, and was 40 ±5 µm thick; while the randomly distributed nanofibers had diameter of 470 ± 110 nm.

6.2.2   Lamination

All GLARE panels considered in this study were made of 2024-T3 aluminum alloy sheets with a thickness of 0.4 mm and of unidirectional glass/epoxy prepregs 220 g/m^2 (GF 12/200 DLN-IMP503Z), supplied by Impregnatex Composite Srl (Milan, Italy). To achieve the desirable adhesion between aluminum layers and glass/epoxy laminates, the specimens were pretreated by Lualma Anodica s.r.l. (Imola, Italy) according to the ASTM D2651 [133]. The lamination curing process was accomplished at the Metal T.I.G Company under vacuum in autoclave, maintaining the material for 1 h at 120 °C temperature and 6 bar pressure according to the supplier's specifications. To consider the effect of interleaving Nylon 6,6 nanofiber on the impact damage of GLARE two types of laminates were tested: "Virgin" without nanofiber and "Nano" modified by interleaving the Nylon 6,6 nanofibrous mat. For the samples of the second group, the Nylon 6,6 nanofibrous mat was interleaved between the prepreg lamina and aluminum one on the top and on the bottom of the laminate following the procedure described in Paragraph 2.2.3. The lay-up configuration of the two types of samples is depicted in Fig 6-1. Final thickness was 2.26 ± 0.01 mm for the virgin laminate and 2.28 ± 0.01 for the nano-reinforced one. The increase of thickness due to the interleaving of the 2 nano-mats (20 µm) is lower than their pristine thickness (40x2 = 80 µm), because of their compression during curing in autoclave. From each panel, 12 samples measuring 150 x 100 mm^2 were extracted, in which the laminas with zero angles are oriented along the short edge direction of the sample.
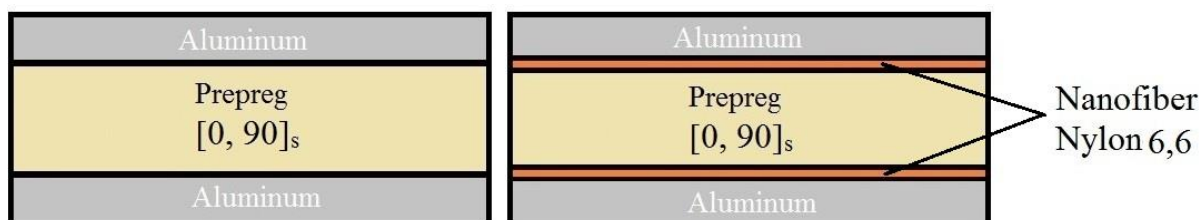
Fig 6-1 Lay-up configuration of (a): virgin-(b): nano-modified GLARE.

6.2.3   Low velocity impact test

Low velocity impact tests were performed following the ASTM D7136 standard [134] using a drop-weight machine as shown in Fig 6-2. A laser device was installed on the machine to capture the pre-impact and post-impact velocity of the impactor and the laser signal was acquired at 100 kHz. To measure the contact force, a piezoelectric load cell (PCB 208C05) was mounted on the tip of the impactor and the signal was acquired at 100 kHz. The impactor had an hemispherical tip made from steel with a diameter of 12.7 mm. The total mass of the impactor was 1.30 kg. Four nominal kinetic energy levels of 6, 12, 18 and 32 J were chosen. For each test case, 3 samples were tested for a total of 24 impact tests. The target was located on the steel fixture cut out with a 125 and 75 mm rectangular opening hole. A four-rubber-tip toggle clamp was used to hold the sample in place. After centering and clamping the specimen to the fixture, the machine was set to the desired impact height. The impactor velocity and its displacement are calculated by integrating the contact force versus time output data as follows [135]:

$$v\left(t\right) = v_i + gt - \int_0^t \frac{F\left(t\right)}{m}\, dt \tag{6-1}$$

$$s\left(t\right) = s_i + \int_0^t v(t)\, dt \tag{6-2}$$

where $v(t)$, $s(t)$ and $F(t)$ are the impactor velocity, position and the measured contact force over time, respectively; g is the gravity acceleration, v_i and s_i are, respectively, the initial impactor velocity and its initial position, when the impact starts. The absorbed energy versus time is calculated as follows [135]:

$$E_a(t) = \frac{1}{2} m\left(v_i^2 v(t)^2\right) + mgs(t) \tag{6-3}$$
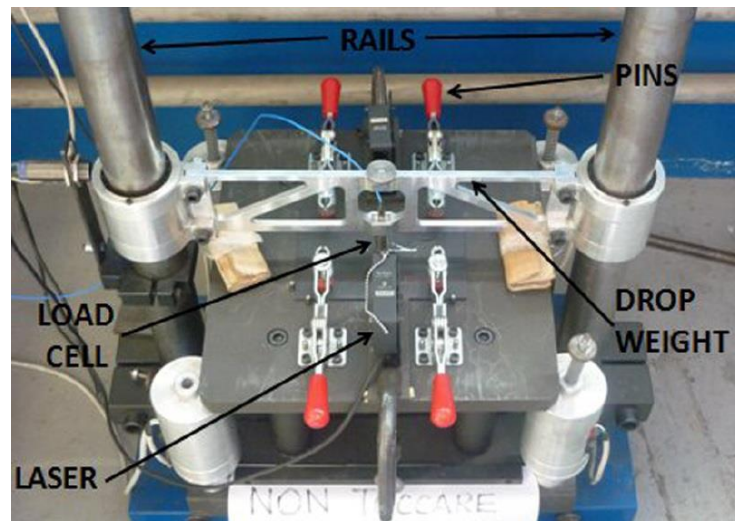
Fig 6-2 Drop-weight machine

The destructive cross sectional technique was employed to investigate the post impact damage in detail. Therefore, after impact testing, the samples were removed from the fixture, sectioned, polished and then observed under optical microscope in order to elucidate the failure mechanisms that occurred during the impact process.

6.3   Results and discussion

The results corresponding to impact tests and post-impact damage assessment are discussed in detail in this section.

6.3.1   Impact response

As mentioned in section 6.2.3, the impact test was conducted using a drop-weight machine at four energy levels for two types of samples: 1- plain GLARE (virgin) and 2- GLARE interleaved by nanofiber mats (nano-modified).

The impact responses of both virgin and interleaved Nylon 6,6 GLARE subjected to E= 6.0, 12.0, 18 and 32.0 J impact energy are shown in Fig 6-3 and Fig 6-4. Graphs (a) and (b) of Fig 6-3 report the contact force and kinetic energy curves in terms of time, while in graph of Fig 6-4 the force is expressed in terms of impactor displacement. Moreover, the main impact data of both virgin and nano-modified laminates are summarized Table 6-1.

The contact force history was almost sinusoidal (Fig 6-3) which represents the domination of the first mode of vibration. The total contact time between the two consecutive zero impact forces represents the contact duration (T_0). The impact force increases continuously to maximum contact force (P_{max}) and then decreases to zero.

According to the law of energy conservation during impact, the impactor energy is transferred from the impactor to the laminate. It increases from zero to a maximum E_{max}, and then drops to E_a, which is the energy absorbed mostly to form the damage. The difference between E_{max} and E_a is the residual or rebound energy E_R.
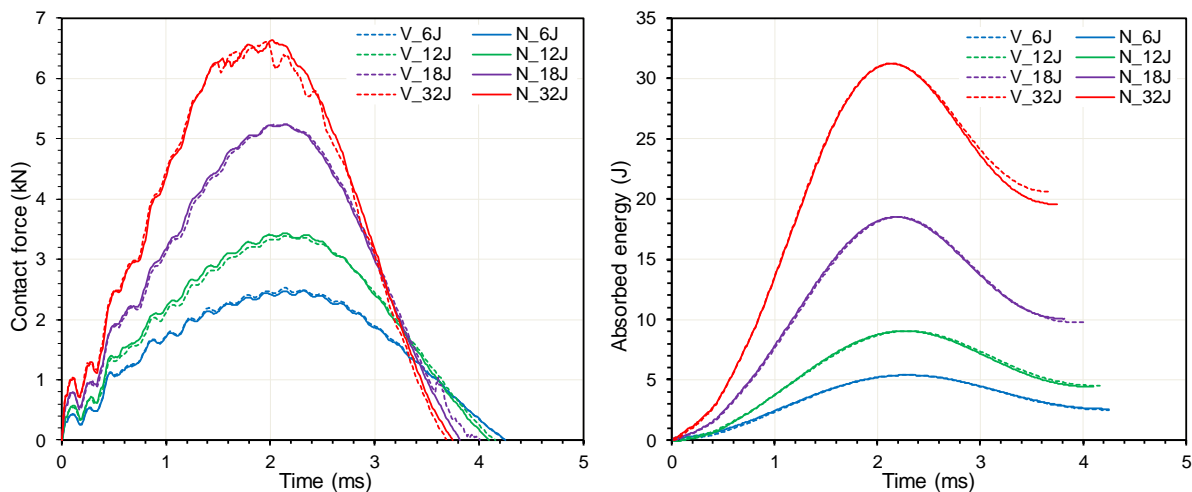
Fig 6-3 Low velocity impact response of virgin and interleaved Nylon 6,6 GLARE impacted at 6, 12, 18: (a) contact force and energy vs time; (b) energy vs time.

Table 6-1 The impact characteristics of virgin and interleaved Nylon 6,6 GLARE at four impact energy levels.

$E_{i\,th}$ (J)	Sample	P_{max}(kN)	s_{max}(mm)	T_0(ms)	E_a(J)	s_{per}(mm)
6	V	2.5±0.00	4.08±0.02	4.25±0.00	2.5±0.1	1.33±0.04
	N	2.50±0.04	4.05±0.02	4.24±0.01	2.5±0.1	1.33±0.01
12	V	3.46±0.11	5.46±0.10	4.13±0.04	4.7±0.3	2.15±0.08
	N	3.44±0.01	5.39±0.07	4.10±0.01	4.7±0.2	2.13±0.08
18	V	5.25±0.02	7.52±0.01	3.99±0.03	9.8±0.1	2.95±0.08
	N	5.22±0.02	7.42±0.00	3.83±0.01	10.1±0.1	3.46±0.01
32	V	6.64±0.04	9.40±0.03	3.75±0.02	20.6±0.1	4.73±0.05
	N	6.61±0.12	9.37±0.09	3.69±0.05	19.4±0.2	5.11±0.07

Increasing the impact energy leads to higher maximum contact force P_{max}, maximum impactor displacement s_{max}, permanent target deformation s_{per}, absorbed energy E_a and lower contact duration for both target types. For each impact energy, the contact force curves vs displacement in Fig 6-4 present different load-drops which are an indication of target damage. The first failure in GLARE subjected to the low velocity impact loading is matrix cracking which occurred at low contact force value and caused a load-drop in contact force history [136]. The other load drops represent other failure modes such as debonding and delamination. At E =18 J energy level, for virgin laminate during the unloading phase, a force oscillation associated with the release of the accumulated elastic strain of the GFRP laminate after debonding of the deformed aluminum layer was recorded, as observed by T. Parnanen et al. [137]. The claimed phenomenon is supported by micrograph analysis and displacement measurement during impact of the bottom of laminate (reported in section 3.2).
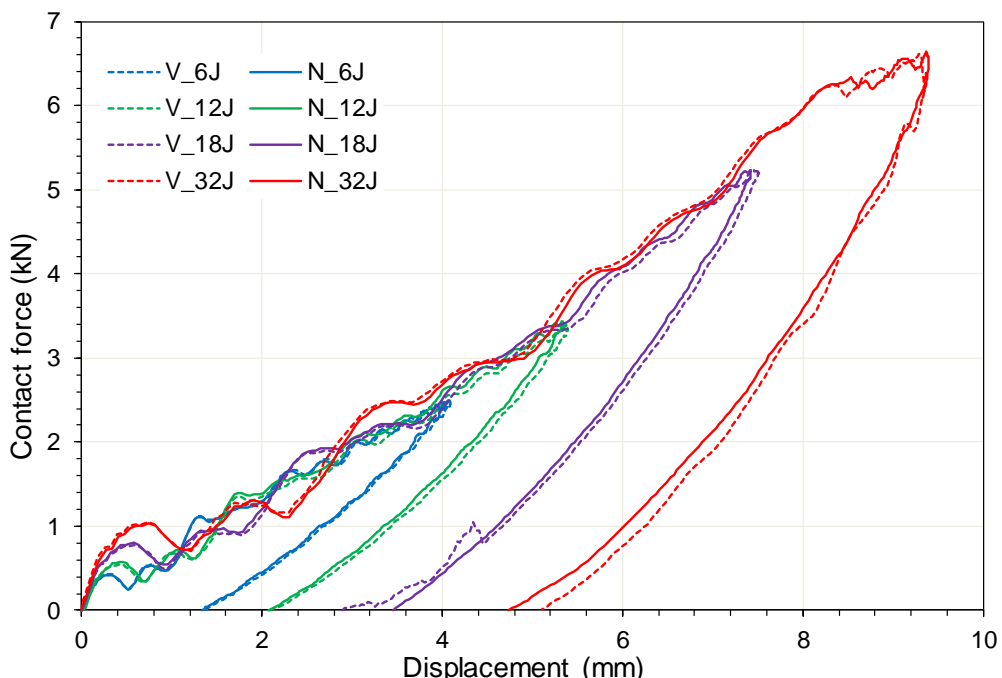
Fig 6-4 Low velocity impact response of virgin and interleaved Nylon 6,6 GLARE impacted at 6, 12, 18: force vs displacement.

Only at E= 32 J energy level, for both virgin and interleaved Nylon 6,6 GLARE, the contact force curves reach a plateau stage which represents the cracking that occurs in the rolling direction of the aluminum lamina on the non-impacted side. Generally, the curves show that interleaving Nylon 6,6 does not have noticeable effects on the dynamic impact response of GLARE as well as the area under the curve of contact force vs displacement. Hence, the absorbed energy is similar for both types of laminates (see Fig 6-4). Only at impact energy of 32 J do nano-modified laminates absorb slightly less energy (- 5%) than virgin ones.

6.3.2   Damage assessment

The damage assessment of impacted specimens was evaluated by micrograph analysis and visual inspection of the surface of the non-impacted side.

Micrograph analysis of the cross section

Fig 6-5 shows the cross section of the impacted laminates, cut along the symmetry axis on the short edge direction of the specimen. Virgin and nano-modified laminates are presented in the first and second column, respectively, and each row represents a different energy level. Only half of the micrograph is reported because the development of the damage along the plane is symmetric respect to the loading axis.

Globally, the laminates present a permanent deformation caused by bending load, while on the centerline of the micrographs the indentation caused by the impactor hemispherical head is visible, with the plastic deformation of the aluminum sheets and the consequent necking of the bottom one (clearly visible at 18 and 32 J). Moreover, during impact, matrix cracks developed through GFRP laminate from top to bottom with a pine tree pattern [138]. The evolution of matrix cracks then induced the delamination at the bottom 0/90 ply interface, the propagation of which increases with the increase of impact energy.

On the contrary, the debonding size of the Al-GFRP interface appears completely different between virgin and nanoreinforced laminates. Virgin laminates, impacted at 6 J, show a delamination of the lower Al-GFRP interface 13 mm long, while nanoreinforced laminates are able to absorb the impact without debonding. At 12 J, nano-reinforced laminates also debond at the lower interface, but the delamination length is lower than virgin ones (17 mm vs 7 mm). For 18 J, the trend is similar with a debonding length of the lower interface of 22 mm and 8 mm for Virgin and Nano-modified laminates respectively; the delamination onset of the upper Al-GFRP interface should also be noted. For 32 J, the debonding length of the lower interface for virgin laminates was almost the same as the ones impacted at 18 J (19 mm) and no significant differences were found with the nanoreinforced ones (18 mm). However, the debonding of the upper interface increases dramatically (31 mm) while for the nanoreinforced ones it is more limited (4.5 mm).

Hence, the micrographs show that interleaving Nylon 6,6 nanofiber mats between the glass/epoxy laminate and the aluminum sheet of GLARE can postpone the debonding onset up to 6J impact energy and drastically reduce the debonding length for higher impact energies.
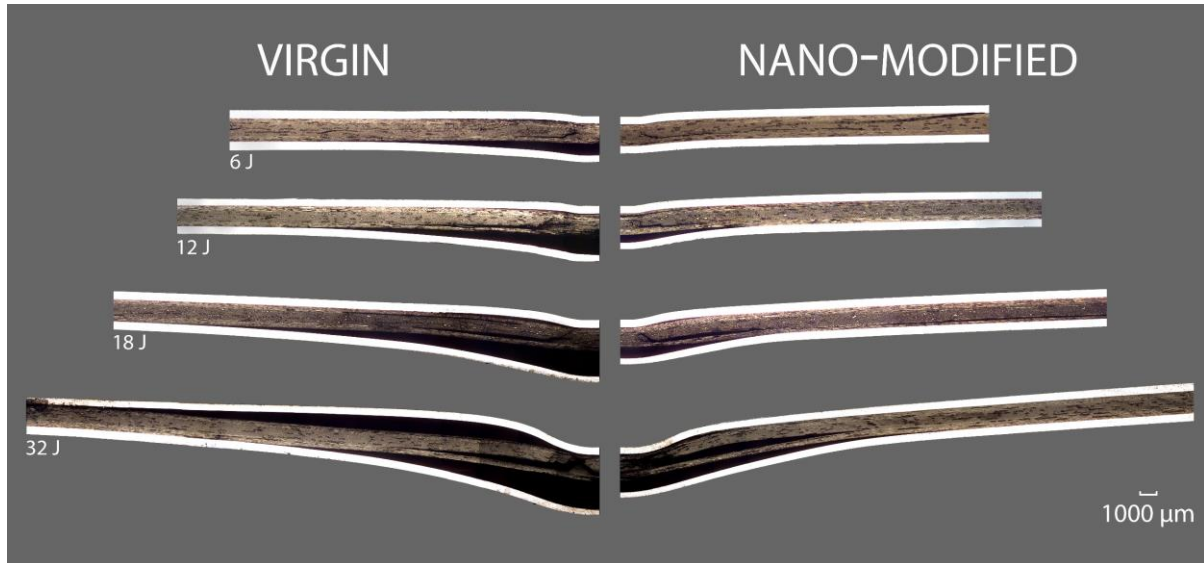
Fig 6-5 Micrograph analysis of post-impacted samples.

However, the different damage extent observed by micrograph analysis, between virgin and nano-modified laminates, is in contrast with the absorbed energy recorded during impact (see 6.3.1). Indeed, the absorbed energy, mostly linked to the damage of the laminate, is almost the same for virgin and nano-reinforced ones.

This phenomenon can be explained in view of the fact that when the GLARE is impacted at high energy levels, during the loading phase, the aluminum layers undergo plastic deformation and maximum target deflection is reached, while the glass fiber lamina still works mostly in the elastic region [139]. Then, when the impactor returns, in the unloading phase, plastic strain remains in the aluminum layers while the glass fiber lamina tends to return to its original flat shape. Therefore, due to the high interlaminar tensions developed between the glass laminate and the lower metal sheet, debonding failure occurs. The extent of debonding can vary, depending on interface strength. Since the plastic deformation is the same for both virgin and nano-modified laminates, according to the maximum displacement recorded during impact, the higher damage resistance of the nano-modified laminate is the result of interlaminar strength improvement by the interleaving nanofibers.

Post-impact displacement of the non-impacted side

In order to better understand the damage mechanism evolution, i.e. the debonding of the lower aluminum sheet during the unloading phase, the impact test at 18 J was replicated adding to the set up a laser transducer pointed at the non-impacted side of the laminate centered with the impact axis. In the graph of Fig 6-6, the filtered displacement recorded by the laser and the impact force is plotted vs time for virgin and nano-reinforced laminates.

While the dynamic response in terms of force is almost the same for both types of laminates, the maximum displacement of the non-impacted side is slightly higher in the case of the virgin laminate (0.15 mm). Then, after the impactor separation, the gap between the two laminates on the non-impacted sides increases to 0.4 mm. This phenomenon indicates that the main damage of the laminate, i.e. debonding of the non-impacted aluminum sheet from the GFRP laminate, occurs during the unloading phase, especially after impactor separation. For this reason, the dynamic response of the GLARE on the impact is not affected by the aluminum debonding.
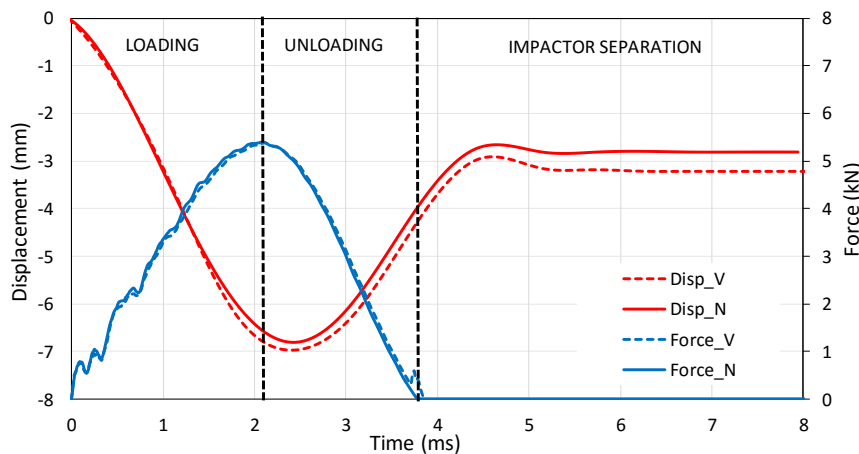
Fig 6-6 Displacement of the non-impacted side and impactor force vs time for virgin and nano-reinforced laminates under 18 J impact energy.

External surface analysis of the non-impacted side

The external damaged surfaces, of the non-impacted side, are shown in Fig 6-7. The surface damage pattern, associated with a rapid change of curvature and related to the internal delamination and debonding of the laminate (as observed by micrograph analysis), is marked with a black line. As expected, the damage area increases as the impactor energy increases. It should be noted that for both cases, the cracking in the rolling direction of the aluminum layer on the non-impacted side was only observed at the highest impact energy, which is due to stretch bending.

The damage pattern for both laminates is similar to a circle at low impact energy, while at higher impact energy it changes from a circle to an elliptic shape only for the nano-modified laminate. A possible explanation may be that the nano-modified laminate compared to the virgin one has higher fracture toughness due to presence of Nylon 6,6 nanofiber mats. As shown before, during impact for both types of laminates, aluminum sheets undergo the same plastic deformation, while the GFRP laminate worked mostly in the elastic region but due to the glass fiber orientation (see Fig 6-1), the GFRP laminate bending stiffness in the long edge direction is less than the short edge stiffness. Hence, when the impactor ascends, lower mode I loading, between the deformed aluminum sheet and the elastic GFRP laminate, will be exerted in the long edge direction compared to the short one.

The Al-GFRP interface of the nano-modified laminate, due to its high fracture toughness, is able to bear the low mode I load exerted along the long edge direction, but not the higher load exerted along the short one. Consequently, delamination propagates more easily in the short edge direction, generating a delamination with an elliptical shape. While in case of virgin laminate, the interlaminar fracture toughness is lower and the delamination can propagate evenly in both directions.
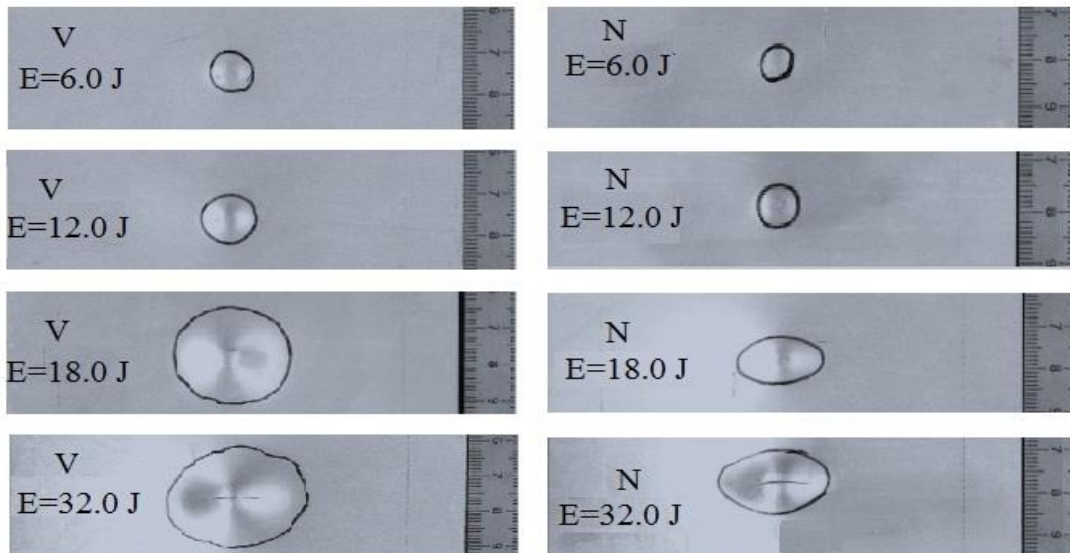
Fig 6-7 Impacted zone of virgin GLARE and interleaved Nylon 6,6 GLARE.

The external damage area for each impact energy level is reported in the bar graph of Fig 6-8. It is noteworthy that for all impact energies, the damage area corresponding to interleaved Nylon 6,6 GLARE is smaller than in the virgin case. Its value ranged from 61 to 685 mm^2 and 35 to 256 mm^2 for virgin and nano-modified cases, respectively. Hence, interleaving Nylon 6,6 can reduce the damage target area of GLARE by 42, 53, 63 and 62 % at impact energy levels of E=6, 12, 18 and 32 J, respectively.
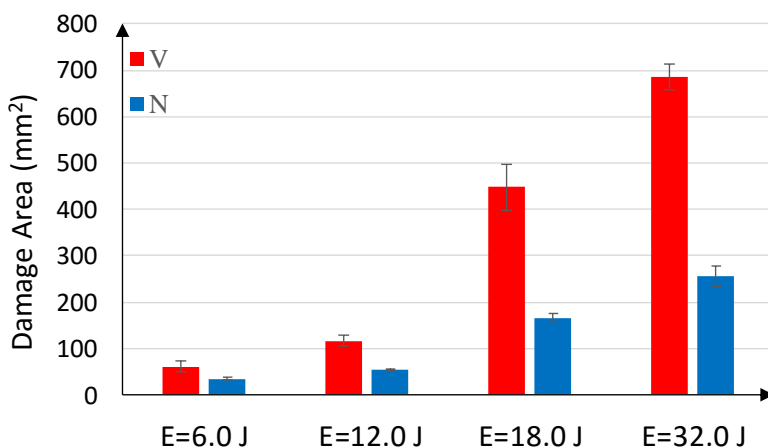
Fig 6-8 Damage area of virgin GLARE and interleaved Nylon 6,6 GLARE.

6.4   Conclusions:

Nylon 6,6 nanofiber non-woven mats were fabricated by electrospinning technique and interleaved between the aluminum sheets and the glass fiber prepreg plies of GLARE laminates. Virgin and Nano-reinforced GLARE were tested at low velocity impact at 4 nominal kinetic energies: 6, 12, 18 and 32 J. The damage was evaluated by micrograph analysis of the impacted zone and visual inspection of the outer surface of the non-impacted side. Experimental results can be summarized as follows:

- Interleaving Nylon 6,6 nanofiber mats does not have a noticeable effect on the dynamic impact response of GLARE: curves force vs displacement appears similar for Virgin and Nano reinforced laminates, as the absorbed energy.
- However, micrograph analysis revealed that interleaving Nylon 6,6 nanofiber mats between the glass/epoxy laminate and the aluminum sheet of GLARE increases their adhesion strength, which reduces the debonding length.
- The discrepancy between the impact dynamic response and the micrograph observations of the damaged zone is explained by debonding of the aluminum lamina after impactor separation.
- The external damage area is reduced by 42, 53, 63 and 62 % at impact energy levels of 6, 12, 18 and 32 J respectively.

Therefore, interleaving Nylon 6,6 nanofibers between the aluminum and the GFRP laminas can generally halve the debonding area of GLARE laminates subjected to impact.

7   Self-healing composite laminates based on core-shell nanofibers

In this chapter, the development of an extrinsic self-healing system for composite laminates based on core-shell nanofibers filled with healing agent is described. The aim is to create a composite material able to self-repair in case of local damage, by miming the human vascular system: the matrix will be integrated with two types of core-shell nanofibers filled with the epoxy pre-polymer and the hardener, respectively; ready to flow by capillarity within the crack induced by the damage; the pre-polymer once it gets into contact with hardener will begin to cross-link healing the crack.
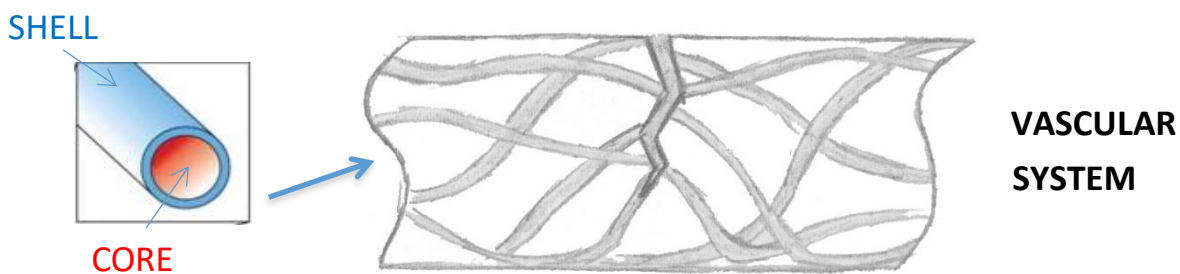
Fig 7-1 Self-healing system based on core-shell nanofiber

Core-shell electrospun nanofibers are a promising method for encapsulation of reactive agents in self-healing composite laminates. The main difference between core-shell as encapsulating system compared to microcapsule and microchannel ones is the dimension, the first are often one or two orders of magnitude smaller than the seconds (see paragraph 1.3.2). Therefore, the integration of the repairing system within the composite laminate shouldn't reduce the inherent mechanical properties of the material as it often happens for micro encapsulation based systems. Indeed, in previous chapters, it has been proven that monolithic nanofibers, which have similar dimension and morphology to the core-shell ones, can even increase the fracture toughness of composite materials. Moreover, the thin polymeric core-shell nanofibers are flexible and the nano-mat is expected to conform the shape of the primary reinforcement architecture at the ply interfaces (e.g. woven). In this way, a dense vascular network is created, which cover the entire weak interlayer of the composite laminate (including resin pockets). Therefore, even the onset of the delamination can be intercepted by the core-shell vascular self-healing system and so be healed before it becomes critical for the composite laminate.

7.1 Progress on self-healing systems based core-shell nanofibers

The first self-healing attempt based on core-shell was made by Jeong-Ho et. al. in 2010 [140], for coating applications. They electrospun on a metal substrate two types of beaded core-shell containing either part A or B of siloxane precursor, encapsulated in a poly(vinylpyrrolidone) shell. Then a polyurethane UV curing resin was spun casted in the nanofiber mat and cured. Then the substrate was scratched and the release of the healing agent was observed at the SEM microscope. After 120 hours of salt water immersion, no rust formation was observed on the self-healing sample while the control sample rapidly corrodes in the scribed region. Later, researchers further investigated with success the use of polydimethylsiloxane (PDMS) as healing agent, encapsulated in core-shell nanofibers, for coating and adhesive applications [141]–[145] (see Table 7-1). PDMS has good chemical barrier performances, however the mechanical ones are low. Hence, it can be suitable only for non-structural materials applications, such as coatings.

Table 7-1 State of art on core-shell based self-healing systems.

Application	Baseline material	CORE (Healing agent)	SHELL	Test	Healing	Ref.
Coating						
	Polyurethane	PDMS	PVP	S-ECC	100 %	[140]
	Epoxy	PDMS	PAN	S-ECC	~ 100 %	[141]
	PDMS	PDMS	PAN	S-CC	100 %	[142]
	Silicone	PDMS	PVA	S-ECC	~ 100	[143]
	PDMS	Epoxy & Thiol	PVDF + PEO	BFT	8 fold	[144]
Adhesive						
	-	PDMS	PAN	BT	110 %	[145]
Bulk material						
	Epoxy	Epoxy (no hardener)	PVP	-	-	[146]
	Epoxy	Epoxy & Ammine	PMMA & PAAm	3PB	95 %*	[147]
	Epoxy	DCPD +Grub	PMMA & PAAm	3PB	95 %*	[147]
	PDMS	PDMS	PAN	TT	140 %	[148]
	PDMS	Epoxy & Thiol	PVDF + PEO	M(T)-SF	100 %*	[149]
	PDMS	Epoxy & Thiol	PVDF + PEO	M(T)-S	150%	[150]
	Not integrated	Epoxy & Amine	PAN	-	-	[151]
	Not integrated	Epoxy & Ammine	PVA	-	-	[152]
Composite laminate						
	CFRP interlayer	DCPD + Grubb's cat.	PAN	3PB-I	80**	[82], [153]

Test type: S-ECC: scratch and electro chemical corrosion; S-CC: scratch and chemical corrosion; BT: blister; BFT: blister fatigue; 3PB-F: three-point bending fatigue; TT: tensile; M(T)-SF middle-crack tension static fatigue; M(T)-S: middle-crack tension static; 3PB-I F: three-point bending interlaminar failure. * Fatigue damage propagation arrested. ** Restore of the pre-damage properties

Xiang-Fa Wu et. al in 2013 [153] interleaved CFRP laminates with core-shell nanofibers filled with dicyclopentadiene, while in the matrix the Grubb's catalysts was dispersed (same healing agent system used by White et. al. in 2001, [50]). A [0°/±45°/90°]s stacking sequence was selected purposely, in order to have large free-edge stresses and induce so delamination at the 0/45 and 45/90 interfaces, where the nanofibrous mats were placed. The laminates where bending loaded up to failure (mainly delamination) and then soon re-tested, later (two hours spent at ambient temperature) the laminates were tested for the third time. The self-healing samples after damage (first cycle) loosed 40 % of its strength, while after healing (third test) they have fully recovered the initial resistance. However, despite the very positive results, it is unlikely that the self-healing system set in this manner will become a commercial reality, because the Grubb's catalysis used as catalyst is extremely expensive (10'000 euros for 100 grams).

A more cost affordable solution is the use of a two-component epoxy system as healing agent. Moreover, the use of epoxy as healing agent ensures fully compatibility with the epoxy matrix of the composite laminate to be healed. This would allow to obtain a completely restore of the initial properties and avoid the formation of a weak interface between healed zone and the surrounding matrix. Recently, researchers have put effort to encapsulate the epoxy prepolymer and the highly reactive hardener in core shell nanofibers, by co-electrospinning.

J. S. M. Zanjani et. al. [147] encapsulated the epoxy pre-polymer and the amine-based hardener in two separated tri-axial core-shells with Poly (methyl methacrylate)-polyacrylamide composite shell. The nanofibrous mat was embedded in a epoxy matrix. The specimens were loaded in three-point bending until reaching a non-linear behavior, which was linked to the onset of microcracks; then, after healing at 70 °C for 24 hours, the samples were retested. For each specimen, the test procedure just described was later repeated other 4 times. The self-healing samples after 4 test cycles reduced their strength of 5 % while the strength of the reference ones, reinforced with allow fibers (without healing agent), was reduced of 12 %. Other researchers [146], [151], [152] report the encapsulation of the epoxy pre-polymer, but the mechanical tests to assess the healing feasibility have not been performed yet. Or, the healing feasibility of the system have been evaluated only in weak PDMS matrix, [148], [149].

7.2   Background on co-electrospinning:

7.2.1   Technique

Co-electrospinning is an effective technique to produce core-shell fibers of nanometer or sub-micrometer diameter, first reported by Sun. et al in 2003 [154]. Generally, co-electrospinning uses two concentric capillaries to form a *core* material encapsulated in a different *shell* material (see Fig 7-2 a). The inner and outer needles are fed separately by the core and shell solutions with the flow rate controlled by two different syringe pumps.
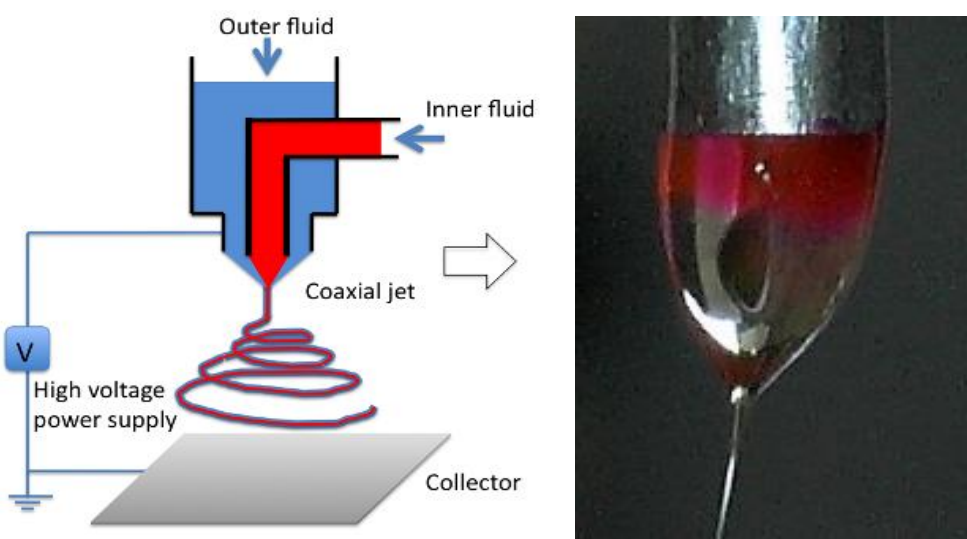
Fig 7-2 (a) Setup for coaxial electrospinning, Ref. [155]; (b) Micrograph of the compound Taylor cone.

The process is in principle similar to conventional electrospinning described in paragraph 2.1.1. When the two-layered drop is charged, by the high applied voltage, the charges may be arrange on the outer surface of the external shell solution [156]. Reached a critical voltage level, the electrostatic forces overcome the surface tensions and a liquid jet emerges from the drop to form a "compound Taylor" cone. The stress generated in the shell solution drag the core solution by shear viscous forces and contact friction at the interface (see Fig 7-3). During the flight toward the collector the compound jet dries and undergoes bending instability which elongate it in a whipped cone shape. Finally, it settles on the grounded collector in the form of core-shell fibers with nano or sub-micron diameter.
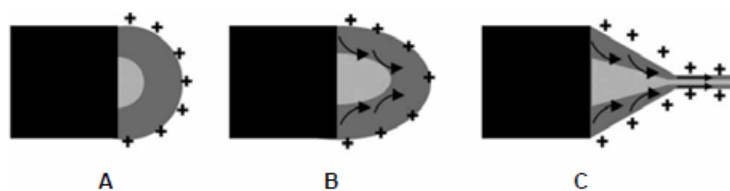
Fig 7-3 Compound Taylor cone formation. A: charge on the on the outer surfaces of the shell solution. B: elongation of the drop and viscous drag forces exerted by the shell solution on the core one. C: eruption of the Taylor cone with the shell solution dragging the core one. Reprinted from ref. [156].

In figure Fig 7-2 b the compound Taylor cone is showed. The micrograph was taken in proximity of the coaxial needle, during the co-electrospinning process in which the core was marked with a red die. Beside the unwanted swelling of the red die on the top of the drop, in the bottom, the formation of a thin shell of the outer solution, which drag the core in the stream, is visible, namely the compound Taylor cone.

7.2.2 Co-electrospinning process parameters

Since the process of co-electrospinning is an evolution of the single variant, all the solution and process parameters, which govern the later, also affect the behavior of the former (see paragraph 2.2). Moreover, during co-electrospinning process the core and shell solutions are in contact for a few seconds inside the drop and then for few millisecond in the jet up to the solvents evaporate. The degree of interaction between them, in physical and chemical terms plays a crucial role on the successful formation of a core-shell structure [156]. Below are described the most important parameters.

Solution miscibility:

The interaction between the core solution and the shell one, is the most critical factor for successful co-electrospinning. Firstly, the solvents of either the core or the shell solutions should not make precipitate the polymer of the other one, when they come into contact at the nozzle tip [157]. Moreover, the interfacial tension should be low enough to ensure a stable compound Taylor cone and allow the shell to drag the core.

Regarding the miscibility of the two solutions, the researcher's opinions diverges. Clearly, a well-defined core-shell structure can be obtain when the core and shell solutions are immiscible, as they will remain phase-separated through the entire co-electrospinning process [158]–[160]. However, several researchers have demonstrated that core-shell structures can be also gained with two miscible shell solutions. Z. Sun et al. [154] produced core-shell nanofibers by using the same solution of PEO in a water-ethanol mixture for both the shell and the core, only by differing the concentration. They postulated that the mixing of the two solutions did not occurred because the diffusion time, of the two solution at the boundaries, was longer than the bending instability time (~1 ms) of the electrospinning process. The assert was also supported by J. H. Yu et al. [161] in a different work with different polymeric solutions. However, it was not considered that during the electrospinning process, the two polymeric solutions stay in contact also in the drop of the capillarity for more than a second, which is longer than the time necessary for the diffusion of the two polymer solutions [160]. The above contrast observations, based on a limited number of works, clearly suggest the need of further investigations on the topic.

Probably, a clearer overview of the problematic can be done, by separating it in two different phenomena: the *miscibility* of the solvents of the two solutions from the *solubility* of one solute (the polymers) with the solvent of the other solution [158]. In this meaner four different cases can be recognized:

- **Miscible – nonsolvent:** the core solvent is miscible with the shell solvent but do not solve the shell polymer.
  - ➢ When the solvents of the two solutions mix in the drop at the capillary tip, the shell polymer *precipitate* out of the solvent mixture. The result is a coagulated, non spinnable solution at the capillary tip.
- **Miscible – solvent:** the core solvent is miscible with the shell solvent and solve the shell polymer (e.g. the core and the shell share the same solvent)
  - ➢ It produce a *reasonable well-defined core shell-structure with few voids and interpenetration* [158], if the two polymers do not make a blend. Moreover, the low interfacial tension between the two solution (same solvent surface tension) facilitate the viscous dragging of the core by the shell.
- **Immiscible – nonsolvent:** core solvent is not miscible with the shell solvent and do not solve the shell polymer.
  - ➢ The immiscibility and solubility of the polymeric solutions guaranty a well phase-separation during the co-electrospinning process due to the local precipitation of the polymers at the interfaces. It produces *a well-defined core-shell structure* (often the best one). However, the interfacial tension has to be reduced by choosing the appropriate solvents or blend of solvents.
- **Immiscible-solvent:** core solvent is not miscible with the shell solvent but solve the shell.
  - ➢ Whereas the core and shell will not mix because of the non-miscibility of the two solvent systems, a solid interface between the two solutions will not form because of the mutual solubility of the polymers by the two solvent systems. This allow the shell to drag easily the core because, due to the good adhesion at the interface, the shear forces can be easily transmitted. However, despite the co-electrospinning process can be smooth, the *score-shell structure is not always perfectly well-defined*.

Solution viscosity:

During co-electrospinning the core solution is dragged by the shell one. Therefore, the viscosity of the shell solution has to be high enough (usually higher than the required for conventional electrospinning), to exert sufficient viscous shear stresses, overcome the interfacial tension between the two solutions and so drag the core [162]. If increasing the viscosity is not enough, another option is to lower the interfacial tension by tuning the solvent systems of the two solutions or using a surfactant.

Moreover, the shell solution should be electrospinnable on its own. While this is not necessary for the core solution, which must only possess a minimum viscosity in order to be dragged continuously by the shell without jet break-up.

Solvent vapor Pressure:

As occurs in conventional electrospinning, if the vapor pressure of the core and shell solvents are too high, the solvents will evaporate to quickly and the solution will dry at the drop of the capillarity tip; if it is too low, the core-shell fiber will reach the collector still wet and will merge forming a film. In general, the solvents of the core and the shell should have similar vapor pressure to avoid the collapse of the shell [163].

Moreover, if the vapor pressure of the core solvent is particularly high compared to the shell one, the core solvent can exert a too high pressure on the surrounding shell solution of the drop, with the risk to break the shell and make the process unstable.

Surface and interfacial tension:

As previously noted the interfacial tension can affect the transmission of the shear stresses between the shell and the core at the interface, which is crucial for the core to be dragged by the shell during co-electrospinning process and have a stable process. The interfacial tension are related to the surface tension of the two solutions, which in turn are mainly a function of the solvent in the solutions and tends to be less sensitive to variation in the polymer concentration [164].

Solution conductivity:

J. H. Yu et al. [161] speculated that if the core solution is more conductive than the shell one, it will be pulled at higher rate by the applied electric field causing a discontinuity in the core-shell structure. Hence, the shell conductivity has to be higher than the core one to drag the later.[165] However, a too high conductive shell solution, will make thinner the core because the shear drag forces exerted by the shell on the core will not be high enough to sustain the pulling electrostatic forces exerted on the shell. It is important to note that also if the core is not conductive and ca not be electrospun by itself, it can be co-electrospun with the conductive shell.

Flow rate:

The flow rate of the shell solution should be higher than the core one (usually in the range of 5 to 20 times), so that the viscous shear forces exerted by the shell solution are enough high to drag and confine the core.

7.2.3   Solution system selection based on Hansen solubility parameters

The selection of the polymer and the solvents suitable for the encapsulation of the healing agent by co-electrospinning, was assisted by a homemade program, based on the Hansen solubility parameters and integrated with useful electrospinning process parameters.

Hansen proposed a compound solubility parameter that provide a quantitative measure of the degree of interaction between the solvent and the polymer. The composed parameter is an evolution of the solubility parameters proposed by Hildebrand, which is defined as square root of the cohesive energy (which keep the molecules of the liquid together), measurable as the total amount of energy required to vaporize the solvent at the onset of the boiling point (energy necessary to win the cohesive forces):

$$\delta = \sqrt{\frac{E}{V}} = \sqrt{\frac{\Delta H - RT}{V}} \qquad (7\text{-}1)$$

where, ΔH is the enthalpy of vaporization, R is the gas constant, T is the absolute temperature and V is the molar volume.

Note that in a liquid the molecules stick together thanks to the cohesive forces, which allow to maintain the microscopic structures such as a water drop. Hence, cohesion is responsible for the surface tension which is also an important parameter in the electrospinning process.

However, the Hildebrand parameter fail to predict the solubility behavior of polar solvents. Hence, Hansen refined the parameter by dividing it in three components, called the Hansen solubility parameters (HSPs): δ_d the atomic London dispersion bond, δ_p the dipolar intermolecular bond and δ_h the molecular hydrogen bond. The Hildebrand parameter can be then defined as:

$$\delta = \sqrt{\delta_d{}^2 + \delta_p{}^2 + \delta_h{}^2} \qquad (7\text{-}2)$$

The HSPs can be also represented as a point in a three-dimensional space, known as the Hansen space. The degree of solubility (miscibility) of two solvents is based on the proximity of the solubility parameters. How the parameters are determined is out of the aim of this dissertation, the explanation together with a complete database can be found in the Hansen book [166].

For a polymer, a fourth parameter (R_0) define the radius interaction of a sphere, with center in $\delta_d{}^2, \delta_p{}^2, \delta_h{}^2$; where R_0 is calculated empirically for each solute. If the Hansen parameters of a solvent or a solvent mixture are located inside the sphere, it is likely that they will solve the polymer. This can be graphically evaluated in the Hansen space or calculated by means of following equation:

$$R_a = \sqrt{4\left(\delta_d^p - \delta_d^s\right)^2 + \left(\delta_p^p - \delta_p^s\right)^2 + \left(\delta_h^p - \delta_h^s\right)^2} \qquad (7\text{-}3)$$

where the subscript p denote the polymer HSPs and subscript s the solvent HSPs. The degree of solubility of a specific polymer by a specific solvent is expressed by the RED number, reflecting the relative energy difference:

$$RED = \frac{R_a}{R_0} : \begin{cases} RED > 1 \rightarrow & \textit{likely not solvent} \\ RED = 1 \rightarrow & \textit{may cause swelling} \\ RED < 1 \rightarrow & \textit{likely solvent} \end{cases}$$

A simplified and practical 2-D representation of the Hansen space can be given by unifying the dispersion δ_d and dipolar δ_p Hansen solubility parameters due to their similar effect compared to the hydrogen one, δ_h (Bagley et. al.[167]). The graph will be used in the next paragraphs to select the most appropriate solvents for the shell and the core, in order to encapsulate the healing agent by co-electrospinning.

7.3   Experimental: encapsulation of the healing agent and embedding

In this section are reported the key steps made to achieve the encapsulation of the healing agent.

7.3.1   Materials: Healing agent system and polymer suitable for the encapsulation

Healing agent system:

An extrinsic self-healing system is autonomous if the healing agent, once triggered by the damage, can react and heal the crack at ambient temperature without any external stimulus (e.g. temperature). To satisfy the requisite, it was chosen a room temperature curing epoxy adhesive based on epoxy-thiol reaction catalyzed by tertiary ammine. Epoxy-thiol reactions accelerated by tertiary ammine are usually used in the standard two-component "5-min curing" epoxy, which can be found in the hardware stores [168]. As can be guessed from the name, the reaction occurs quite fast. Moreover, the desired crosslinking time can be tuned by varying the amount of tertiary amine. The choice of this particular hardener stems also from the fact that, thiol is less hydrophilic than common primary amines. This make it suitable for the encapsulation with polymeric water-based solutions, by means co-electrospinning.

A commercial low viscous (500 mPa s) epoxy resin (EPIKOTE 94908), with a molecular weight per epoxy equivalent unit of 165 g/eq., was used as prepolymer. Pentaerythritol tetrakis (3-mercaptopropionate) with a molecular weight per thiol equivalent unit of 122 g/eq. (Sigma-Aldrich) was used as curing agent in stochiometric proportion with the epoxy prepolymer. 2,4,6-Tris(dimethylaminomethyl) phenol (Sigma-Aldrich) was used as catalysis in 10 phr (parts per hundred of total mixture).

Shell polymer:

In an extrinsic self-healing system, a key requisite for the shell polymer is the capability of storing the healing agent, in its reactive status, for the entire service life of the material in which is integrated, until damage occur. Moreover, the polymer has to be suitable for the encapsulation process, in this case co-electrospinning. Different polymers were experimentally investigated and Polyvinyl alcohol (PVA) was selected as candidate polymer to encapsulate the healing agent, because able to satisfy both the aforementioned requisites. PVA is a water soluble polymer with relative high melting point (180-190 °C, so higher than typical composite curing cycles temperatures), excellent chemical resistance to organic solvents (which are usually employed in epoxy resins to temporally reduce the viscosity [168]) and is not permeable to gasses [169]. Moreover, it is often used as release agent in molds for epoxy-based composite materials. Hence is expected to be suitable for the encapsulation of the epoxy based healing agent.

Poly (vinyl alcohol) 88% hydrolyzed with a molecular weight (Mw) of 88,000 (ACROS ORGANICS) was used as based material.

Solvents were supplied in their pure form Sigma-Aldrich. While as cross linker for PVA was used Poly (acrylic acid) (PAA) in 63 wt% water solution with an average Mw of 2000, supplied from Sigma-Aldrich.

7.3.2   Selection of the solvent system by means of Hansen solubility space

The selection of the solvent systems for the core and the shell suitable for the encapsulation by co-electrospinning was made using the Hansen solubility parameters described in section 7.2.3. In Fig 7-4 the simplified 2-D dimensions the Hansen solubility space is represented for PVA and Epoxy. The electrospinning common solvents are represented by green dots, while solvent blends by purple triangles. The polymer solubility spheres (2-D projected) are defined by a red and blue circle for epoxy and PVA, respectively.
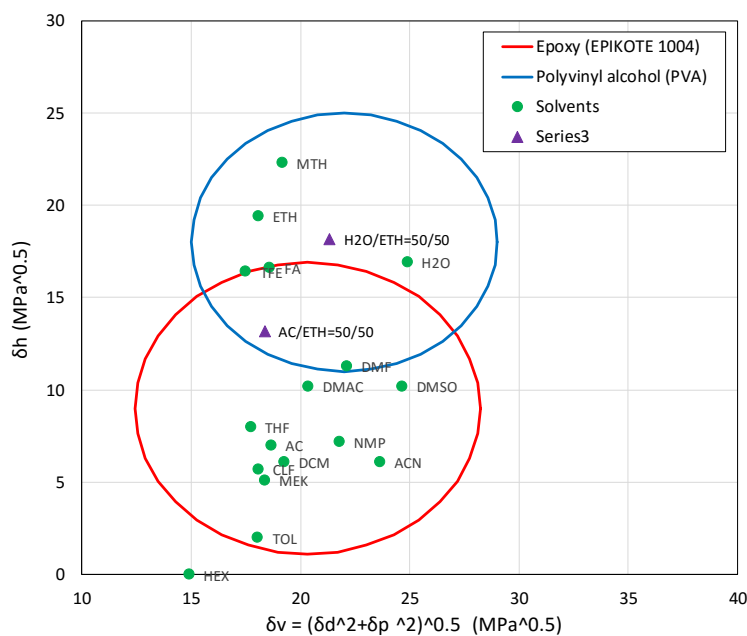
Fig 7-4 2-D Hansen solubility space for Epoxy prepolymer and PVA polymer.

Based on the graph: epoxy is likely to be dissolved by non-polar or polar aprotic solvents, while PVA by polar protic solvents. Different solvent systems were experimentally investigated in order to make the co-electrospinning process feasible and stable based on the suggestion presented in [158]. Below are listed the key ones, which were classified based on the cases identified in paragraph 7.2.2 (for an overview of the cases is suggested to refer to the above Hansen chart):

- **Shell = water** (H2O); **Core = acetone** (AC) -> _miscible non-solvent:_
  - ➤ the shell and the core solvents are miscible, but the core solvent don't dissolve the shell polymer and vice versa;
  - ➤ the result was a coagulated non spinnable solution due to the mixing of the two solutions and consequent precipitation of the two polymers in the drop at the capillary tip. Also the high vapor pressure of core solvent (AC) contributed to make the process unstable.

- **Shell = water** (H$_2$O); **Core = acetone/ethanol=50/50 v/v** (AC/ETH=50/50) -> *miscible non-solvent:*
  - ➢ the shell and the core solvent systems are miscible, but the shell solvent do not dissolve the core, while the core solvent blend is more compatible with the shell;
  - ➢ the drop coagulated less than in the previous case but the core was rarely dragged by the shell, probably because of the high interfacial tension between the two polymeric solutions.
- **Shell = water/ethanol = 98/2** (H$_2$O/ETH); **Core = acetone/ethanol = 50/50v/v** (AC/ETH=50/50) -> *miscible solvent:*
  - ➢ the shell and the core solvent blends are miscible, and both dissolve the polymers of the other one;
  - ➢ the drop did not coagulate and the core was drained in a continuous manner. The low interfacial tension probably facilitated the process.
- **Shell = water/ethanol = 98/2** (H$_2$O/ETH); **Core = Dimethylformamide** (DMF) -> *miscible solvent:*
  - ➢ the shell and the core solvent blends are miscible, and both dissolve the polymers of the other one;
  - ➢ the drop was drained in a continuous manner and the process was more stable than previous, probably due to the low vapor pressure of the core solvent. Moreover the high dielectric constant of DMF facilitated the self spinning of the core by means of the forces exerted by the electric field;

Hence, it can be concluded that the best solvent system combination is the last one, which can guaranty a stable and smooth process.

7.3.3   From beads to continuous core-shell

The main advantage of vascular self-healing systems compared to those based on microcapsules is that they can theoretically supply an infinite amount of healing agent to the damage zone, being fed from peripherical non-damaged zones.

A critical aspect in co-electrospinning is to gain the optimal ratio between the viscosity of the polymeric shell solution and the core one [162]. If the viscosity of the shell solution is low compared to the core one ($\eta_{shell}/\eta_{core}\downarrow\downarrow$), the shear forces exerted by the shell solutions will be not enough to drag the high viscous core and retain it in a continuous meaner during spinning. If, the core solution viscosity is too low compared to the shell ($\eta_{shell}/\eta_{core}\uparrow\uparrow$), the core solution will not have enough viscosity to be stretched without having frequent breakages of the core flow, resulting in small intermittent droplets inside the core-shell drop at the capillary tip. In both aforementioned cases the nanofibers will have a non continuous core-shell beaded structure.

The starting point viscosity ratio of PVA / epoxy solutions based on ref. [146] was found to be in the low regime, which resulted in beaded core-shell nanofibers with non-continuous encapsulation of the healing agent and detrimental effect for the efficiency of the vascular system. In Fig 7-5 a is showed the morphology of first core-shell nanofibers spun with a 10 wt% solution of PVA in solvent mixture of H2O:ETH = 98:2 wt% and a 95 wt% of epoxy solution in a solvent mixture of ETH:AC = 50:50 wt%; where the core was marked with a florescent

blue dye. Cleary the core-shell are bedded and the healing agent is encapsulated in a non-continuous manner. By increasing the concentration of the PVA and hence the viscosity, the beads were elongated giving a quasi-continuous core-shell structure, see Fig 7-5 b. However further increment of the concentration of PVA was not possible due to the high viscosity of the solution which made it not electrospinnable.
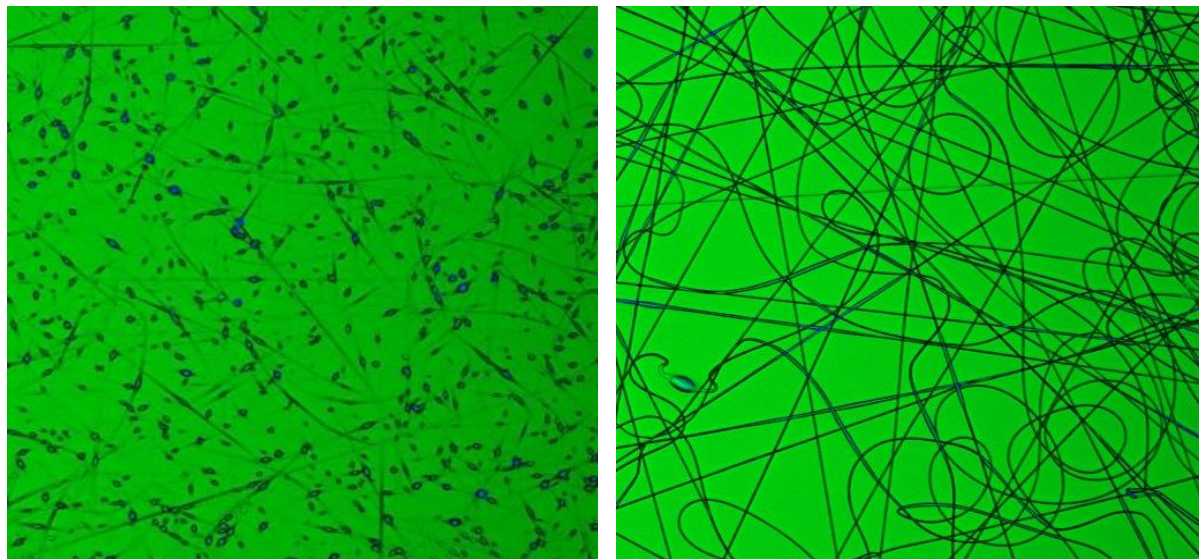
Fig 7-5 Florescent micrograph analysis of PVA-epoxy core-shell nanofibers with different solution viscosity: a) shell: PVA 10 wt% in (H2O:ETH=98:2 wt%) - core: Epoxy 95 wt% in (ETH:AC=50:50 wt%) ; b) shell: PVA 12 wt% in (H2O:ETH=98:2 wt%) - core: Epoxy 95 wt% in (ETH:AC=50:50 wt%).

The optimal morphology was obtained by varying the concentration of ethanol in the shell solution and using DMF as solvent for the core, which probably reduced the interfacial tension allowing so a better transmission of the shear viscous stresses from the shell to the core. In Fig 7-6 a is shown the morphology of the continuous PVA-epoxy core-shell nanofibers so obtained.

Similar tuning process of the electrospinning parameters was made for the encapsulation of the hardener agent (thiol and tertiary amine). The morphology is presented in the florescent micrograph of Fig 7-6 b.
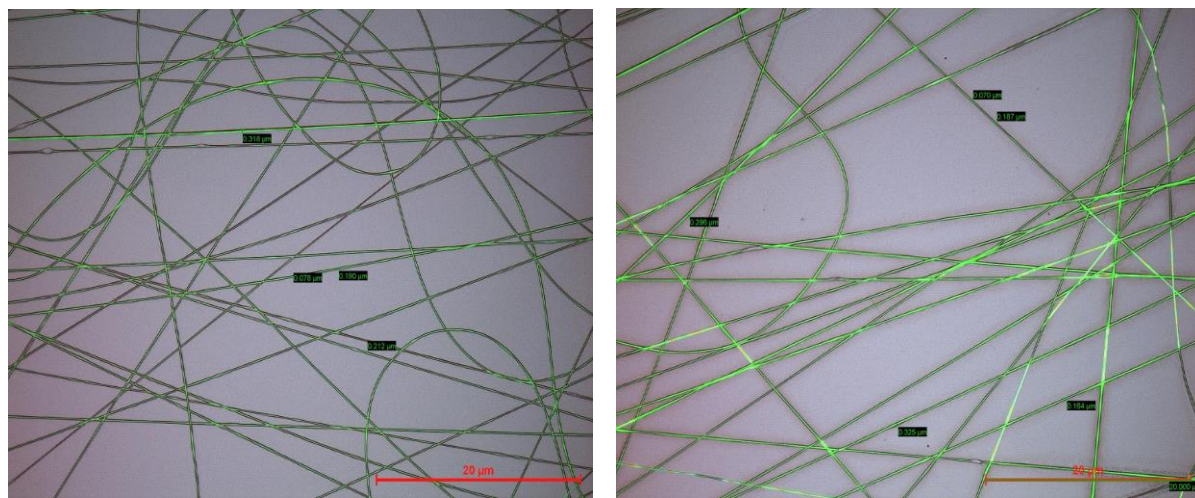
Fig 7-6 Florescent micrograph analysis of the two component optimized core-shell nanofibers: a) shell: PVA 10 wt% in (H2O:ETH=50:50 wt%) - core: Epoxy 98 wt% in DMF; b) shell: PVA 12 wt% in (H2O:ETH=50:50 wt%) - core: (Thiol:3-AM=95:5 wt%) 99 wt% in DMF.

7.3.4   Post crosslinking of PVA:

The encapsulation system in addition to contain the healing agent, must be able to isolate it from the surrounding material in which it is integrated. The Epoxy and the Thiol + tertiary amine after co-electrospinning with the PVA solution were found to be well encapsulated and still in liquid and reactive status. However, when the core-shell were embedded in a common epoxy matrix, during the curing cycle, the reactive primary amine penetrated and reacted with the healing agent (see SEM analysis in the following paragraphs).

In order to make the shell polymer impermeable to the primary amine the PVA was crosslinked. The method described in [170] and [171] of cross linking PVA monolithic nanofibers by means of polyacrylic acid (PAA) was found to be suitable for the present purpose. The crosslinking reaction of PVA with PAA (Fig 7-7) can be triggered, after electrospinning, by curing the nano-mat in hoven in the range of 80-140 °C.
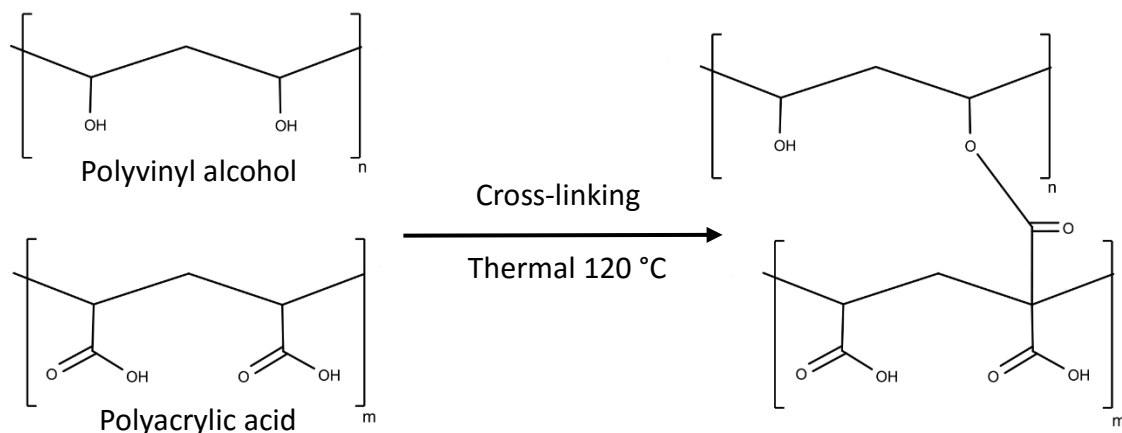
Fig 7-7 Cross-linking reaction of polyvinyl alcohol with polyacrylic acid.

Different shell solutions for electrospinning were prepared by blending the PVA solution with the PAA solution at different out of stochiometric ratios. The best compromise between the swelling of the core-shell nanofibers before cure in hoven (caused by the low molecular weight of PAA) and the degree of crosslinking post-cure was found to be at 50% of stochiometric ratio with excess of PVA. After the co-electrospinning process the nano-mat was cured in hoven at 120 °C for 1 hour.

7.3.5   Combined co-electrospinning

To achieve healing of the damage, once the crack propagates, both healing agent components (epoxy and hardener) must be released in the crack and react in their stoichiometric proportions. Hence, both core-shell A (storing the epoxy) and core-shell B (storing the hardener) must be in the crack's proximity to release the two agents. To satisfy the aforementioned requisite, also in case of micro cracks, core-shell A and B were uniformly mixed, by co-electrospinning them together. For the occasion, was built a specific setup (see fig), composed by a low speed rotating drum collector and two separate coaxial needles fed with core-shell solutions A and B, respectively. The process parameters are reported in Table 7-2. The external and internal diameter of the core-shell nanofibers so obtained was in the 0.6 ± 0.20 µm and 1.5 ± 0.3 µm, respectively.
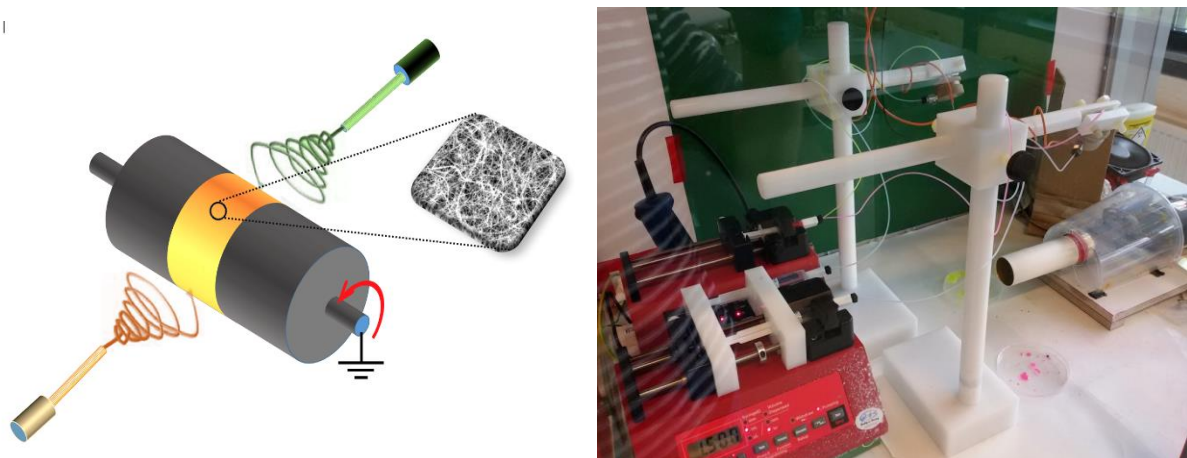
Fig 7-8 Setup made for co-electrospinning together both core-shell A and B: a) diagram; b) photo of the electrospinning chamber.

Table 7-2 Co-electrospinning process parameters.

Type		Polymer	Solvent system	Flow rate (ml/h)	Voltage (KV)	Distance (cm)
Core-shell A					20	24
	Core	99 % Epoxy monomer	DMF	0.12		
	Shell	20 % (PVA:PAA = 55:45 %wt)	H2O:ETH = 50:50 %wt	1.2		
Core-shell B					20	24
	Core	95 % (Thiol:3-AM = 90:10 %wt)	DMF	0.05		
	Shell	20 % (PVA:PAA = 55:45 %wt)	H2O:ETH = 50:50 %wt	1.2		

The electrospinning process was carried out at 24 °C with 50 % of humidity relative humidity (RH). The tangential rotating speed of the drum collector was 0.2 m/s. Both core-shell nanofibers were co-electrospun together and then the nano mat was then immediately cured in hoven for 1h at 120 °C.

7.3.6   Embedding in the epoxy matrix

The core-shell self-healing system was embedded in a common low viscous and curing temperature epoxy system for infusion applications (Sika Biresin CH83-2), with a primary amine based hardener. Three core-shell (A+B) nano mats (each one thick ~ 500 µm) were impregnated in the pre mixed epoxy system and then stacked on a flat mold (wet lay-up). The mold was then enclosed in a vacuum bag with in the middle the release film and the breather to ensure the evacuation of resin excess (vacuum bag molding). The core-shell composite was cured at 55 °C under applied vacuum of 0.7 bar for 15 hours, hence three hours more than prescribed by the supplier to ensure the complete crosslinking of the epoxy matrix and so avoid to invalidate the self-healing results.

7.4   Results:

In this section are described the results of the tests made in order to assess the effectiveness of the developed self-healing system.

7.4.1   Observations of the healing agent release

The morphology of the co-electrospun nano mat containing both core-shell A and B was analyzed by SEM microscopy. To observe the release of the healing agent and the integrity of the shell (no mixing with the core), two types of nano mats were prepared:

- pristine: after the encapsulation process described above it was left untouched;
- washed: after the encapsulation, it was washed in a bath of toluene under stirring for one day (toluene is as solvent for the core but not for the shell).

Both nano mats were then immersed in liquid nitrogen and then cut with a sharp scissor. Has to be mentioned that the mats were stored at least ten days at room temperature before performing the procedure here described.

The SEM micrographs of the cut surfaces for pristine and washed nano mat are presented in Fig 7-9 a and b, respectively.
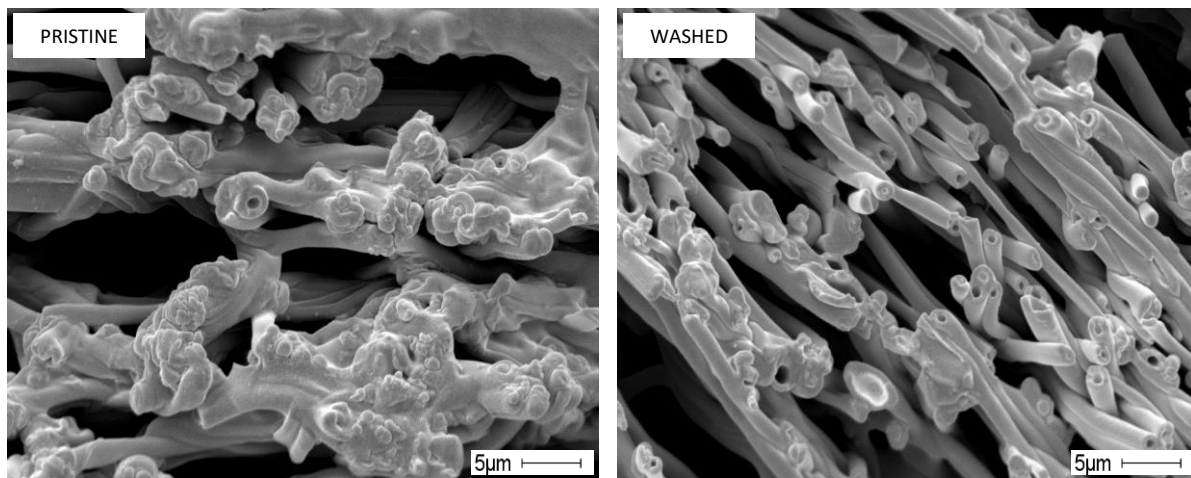
Fig 7-9 SEM micrograph of the cut surfaces of the core-shell (A+B) nano mat: a) pristine, b) washed in toluene.

The pristine mat shows leakage of the healing agent from the core-shell along the cut zone, which clotted at the tip of the sectioned core-shell. It's not clear if the released healing agent has crosslinked or not. Maybe, a further washing in toluene of the sectioned pristine mat could clarify it (if is crosslinked it hardly dissolves in toluene otherwise it will easily dissolve in toluene). Note that the vacuum exerted in the SEM chamber may facilitate the release of the healing agent, but this could be possible only if some gas was entrapped in the core-shell.

The washed mat shows hallow core-shell in which the heling agent was completely removed by the solvent preserving the morphology of the shell.

Hence the micrographs prove that the healing agent was stored in its liquid form (it is soluble and removable by the solvent), it didn't mix with the shell polymer and that can be release upon rupture of the encapsulation system.

For comparison, in Fig 7-10 is showed the morphology of two types of core-shell systems, previously investigated, in which the shell polymer was not able to store the healing agent. The Polyvinylpyrrolidone (PVP) epoxy core-shell nanofibers after washing and cutting shows still the presence of the healing agent inside, which mixed with the shell and formed a non-dissolvable blend. The polyethylene oxide (PEO) core-shell, after washing, show a perforated morphology because of the removal of the epoxy prepolymer which formed previously a two-phase blend with the shell polymer.
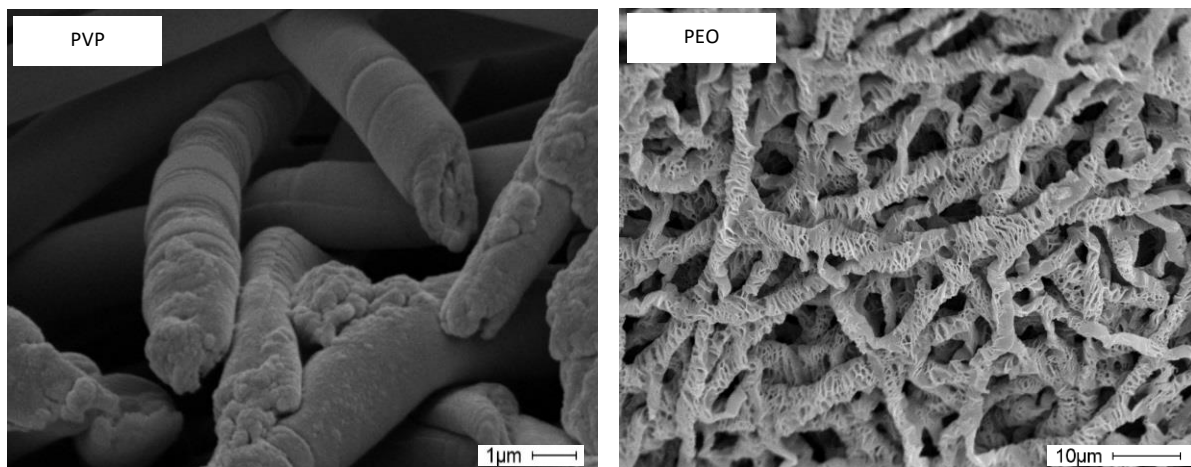
Fig 7-10 SEM micrographs of core-shell were the healing agent was not successfully encapsulated: a) Polyvinylpyrrolidone-epoxy core shell; b) polyethylene oxide core-shell.

7.4.2   Integration of the self-healing system

The co-electrospun nano mat containing both core-shell A and B was embedded in common epoxy matrix with primary amine as hardener, following the procedure described in paragraph 7.3.6. After curing the core-shell reinforced epoxy matrix was washed in a bath of toluene under stirring for two days, to remove the healing agent. Then it was broken and the crack surface was observed at the SEM. In Fig 7-11 a, the core-shell nanofibers with the shell in PVA crosslinked by PAA have a clearly hollow morphology caused by the removal (by washing in toluene) of the still liquid healing agent.

Conversely, the core-shell nanofibers with the shell in neat PVA (Fig 7-11 b) look full, as if they contain another solid nanofiber inside. Perhaps, during curing the matrix, especially the anime, penetrated the shell and crosslinked the contained healing agent. Hence the core was not anymore dissolvable by the toluene bath.
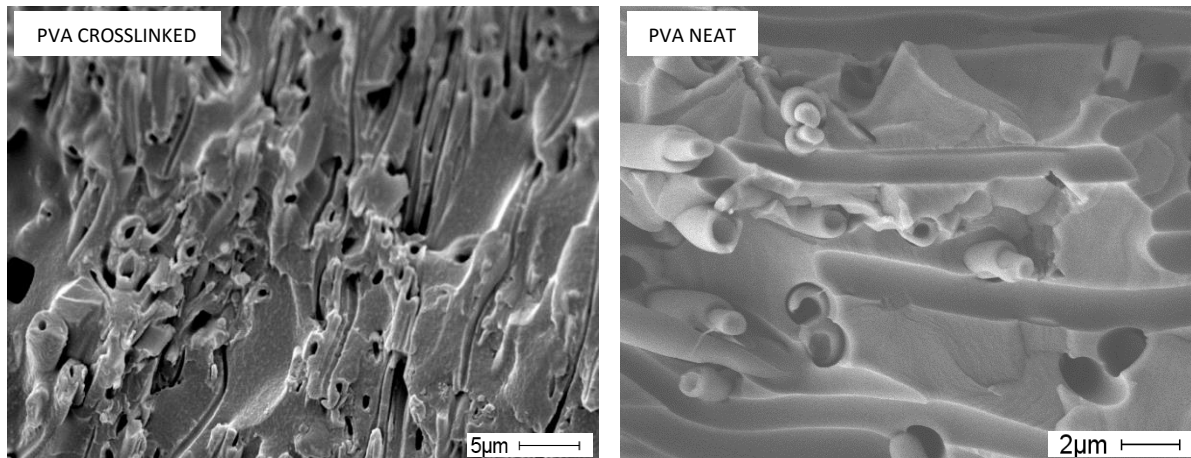
Fig 7-11 SEM micrographs of the core-shell embedded in the epoxy matrix: a) core-shell A+B with shell in PVA crosslinked by PAA; b) core-shell A+B with shell in neat PVA not crosslinked.

7.4.3 Chemical reactivity of the encapsulated healing agent

The chemical reaction between the epoxy and the hardener is exothermic. Hence, to verify the preserved chemical reactivity of the encapsulated healing agent, the nano mats were thermally analyzed by differential scanning calorimetry (DSC). Three type of samples were prepared:

- Neat epoxy mixture: the epoxy prepolymer and the thiol were mixed in the stochiometric proportions with 10 phr of tertiary amine and then immediately tested.
- Core-shell A+B undamaged: the nano mat was left untouched after the encapsulation process.
- Core-shell A+B damaged: the nano mat was chopped with a pair of scissor and grinded with a mortar and then immediately tested.

All the samples were put in a DSC pan crimped with a through lid. The DSC analysis was performed from 0 °C to 150 °C with a heating ratio of 20 °C/min in nitrogen atmosphere. Note that the tests were performed at least ten days after the encapsulation process.
In the graph of Fig 7-12 the DSC plots of the first scan for each sample type are presented.
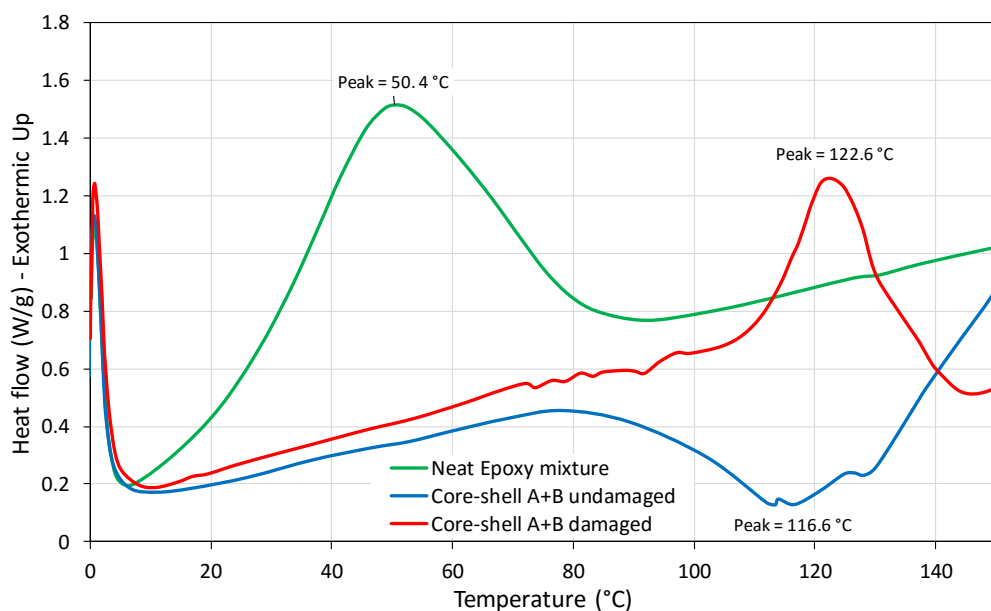
Fig 7-12 DSC thermal analysis of the neat epoxy mixture and of the core-shell A+B nanofiber mat damage and not.

The neat epoxy mixture, as expected, shows a low temperature exothermic peak at 50 °C, generated by the crosslinking reaction of the epoxy+thiol+3-AM system, which is known for curing at low temperatures.

The undamaged core-shell sample shows a broad endothermic peak (with minimum at 116 °C) attributed to the evaporation of the water absorbed by the nanofibers, which disappear in the third DSC scan (not shown in here for brevity). Despite the PVA is cross linked and does not dissolve when soaked in water, it is still highly hygroscopic and the high surface area to volume ratio of the nanofibers dramatically accelerates the moisture absorbing ratio (see Fig

2-10). However, a dehydration through preheating in DSC would invalidate the results of the other samples, hence the pre-heating was not performed.

The damaged core-shell sample shows an exothermic peak at 122 °C which can be attributed only to the cross-linking reaction of the healing agent, as it does not occur in the undamaged one. However, the exothermic peak shows a delay of about 70 °C compared to the neat epoxy mixture. The reason may be that the two components of the healing agent were not mixed in properly and in stoichiometric proportions. Or because the cutting and grinding procedure took longer than the simple mixing of the neat reagents (3 vs 1 minutes) and the reaction was partially carried out before the DSC scan started. Note that the epoxy thiol tertiary amine based systems are usually used for fast room temperature curing reactions in the minute range. Hence, this aspect has to be further investigated.

Nevertheless, through the thermal analysis it was demonstrated that the healing agent is stored in its reactive status and can react and crosslink as result of the damage. Moreover, the encapsulation system is capable of store the two high reactive reagents in close vicinity up to temperatures of 150 °C, which is higher than the normal prepregs curing temperatures.

7.5 Future developments

The next natural step will be to evaluate the effective self-healing system capability of restoring the mechanical properties of the material in which is integrated. The sub-micrometric dimension of the vessels is expected to heal damage with micrometric dimension such as micro cracks and localized delamination, which occur before the damage has reached the critical stage. Therefore, mechanical test which can induce micro cracks and detect their impact on the overall mechanical performance of the sample, will be performed.

References

[1]   K. Mustapha, E. Annan, S. T. Azeko, M. G. Zebaze Kana, and W. O. Soboyejo, "Strength and fracture toughness of earth-based natural fiber-reinforced composites," *J. Compos. Mater.*, vol. 50, no. 9, pp. 1145–1160, 2016.

[2]   R. M. Koide, G. von Z. de França, and M. A. Luersen, "An ant colony algorithm applied to lay-up optimization of laminated composite plates," *Lat. Am. J. Solids Struct.*, vol. 10, no. 3, pp. 491–504, 2013.

[3]   R. Lakes, "Materials with structure hierarchy," *Nature*, vol. 361, pp. 511–515, 1993.

[4]   P. Fratzl and R. Weinkamer, "Nature's hierarchical materials," *Prog. Mater. Sci.*, vol. 52, no. 8, pp. 1263–1334, 2007.

[5]   M. E. Launey and R. O. Ritchie, "On the fracture toughness of advanced materials," *Adv. Mater.*, vol. 21, no. 20, pp. 2103–2110, 2009.

[6]   A. Rafsanjani, D. Derome, F. K. Wittel, and J. Carmeliet, "Computational up-scaling of anisotropic swelling and mechanical behavior of hierarchical cellular materials," *Compos. Sci. Technol.*, vol. 72, no. 6, pp. 744–751, 2012.

[7]   A. K. Kaw and F. Group, *Mechanics of Composite Materials*. 2006.

[8]   H. Corporation, "HexPly Prepreg Technology," *Hexcel Regist. Trademark*, p. 28, 2013.

[9]   E. de Lamotte and A. J. Perry, "Diameter and strain-rate dependence of the ultimate tensile strength and Young's modulus of carbon fibres," *Fibre Sci. Technol.*, vol. 3, no. 2, pp. 157–166, 1970.

[10]   R. O. Ritchie, "The conflicts between strength and toughness," *Nat. Mater.*, vol. 10, no. 11, pp. 817–822, 2011.

[11]   M. F. Ashby, *Materials Selection in Mechanical Design*. Elsevier Ltd, 2011.

[12]   T. L. Anderson, *Fracture Mechanics*. Taylor & Francis, 2005.

[13]   N.J. Pagano, "Interlaminar response of composite materials," in *Composite materials series*, vol. 5, Elsevier, 1989.

[14]   R. Byron Pipes and N. J. Pagano, "Interlaminar Stresses in Composite Laminates Under Uniform Axial Extension," *J. Compos. Mater.*, vol. 4, no. 4, pp. 538–548, 1970.

[15]   T. K. O'Brien, "Delamination of Composite Materials," in *Composite Materials Series*, vol. 4, 1991, pp. 181–198.

[16]   R. Talreja and C. Veer Singh, *Damage and Failure of Composite Materials*. Cambridge University Press, 2012.

[17]   K. L. Reifsnider, "Fatigue of composite materials," in *Composite materials series*, vol. 4, 1991.

[18]   K. . Reifsnider, *Fatigue of Composite Materials*, vol. 4. Elsevier, 1991.

[19]   V. V. Silberscmidt, Ed., *Dynamic Deformation, Damage and Fracture in Composite Materials and Structures (reinforcement pg 38)*. Elsevier, 2016.

[20]   S. Abrate, *Impact on composite structures*. Cambridg university press, 1998.

[21]   X. Zhang, "Impact damage in composite aircraft structures-experimental testing and numerical simulation," *Proc. Inst. Mech. Eng. …*, vol. 212, pp. 245–259, 1998.

[22]   G. Jeronimidis, "The fracture behavior of wood and the relation between toughness and morphology," *Proc R. Soc L.*, 1980.

[23]   S. Chand, "Carbon fibers for composites," *J. Mater. Sci.*, vol. 35, no. 6, pp. 1303–1313, 2000.

[24]   N. J. Pagano and R. B. Pipes, "The Influence of Stacking Sequence on Laminate Strength," *J. Compos. Mater.*, vol. 5, no. 1, pp. 50–57, 1971.

[25]   A. P. Mouritz, K. H. Leong, and I. Herszberg, "A review of the effect of stitching on the in-plane mechanical properties of fibre-reinforced polymer composites," *Compos. Part A Appl. Sci. Manuf.*, vol. 28, no. 12, pp. 979–991, 1997.

[26]   A. P. Mouritz, P. Chang, and M. D. Isa, "Z-pin composites: aerospace structural design considerations,"

References

J. Aerosp. Eng., vol. 24, no. 4, pp. 425–432, 2010.

[27] I. Y. Chang and J. K. Lees, "Recent Development in Thermoplastic Composites: A Review of Matrix Systems and Processing Methods," *J. Thermoplast. Compos. Mater.*, vol. 1, no. 3, pp. 277–296, 1988.

[28] J. W. He, M Y; Hutchinson, "Interlaminar fracture toughness and toughening of laminated composite materials : a review," *J. Appl. Mech.*, vol. 111, no. 5, pp. 270–78, 1989.

[29] M. F. Hibbs, K. Ming, and W. L. Bradley, "Interlaminar Fracture Toughness and Real Time Fracture Mechanisms of Some Toughened Graphite/Epoxy Composites," *Toughened Compos. ASTM STP 937*, pp. 115–130, 1987.

[30] F. Klaus, *Application of Fracture Mechanics to Composite Materials*, vol. 6. Elsevier, 1989.

[31] B. B. Johnsen, A. J. Kinloch, R. D. Mohammed, A. C. Taylor, and S. Sprenger, "Toughening mechanisms of nanoparticle-modified epoxy polymers," *Polymer (Guildf).*, vol. 48, no. 2, pp. 530–541, 2007.

[32] S.-U. Khan and J.-K. Kim, "Impact and delamination failure of multiscale carbon nanotube-fiber reinforced polymer composites: A review," *Int. J. Aeronaut. Sp. Sci.*, vol. 12, no. 2, pp. 115–133, 2011.

[33] D. R. Bortz, C. Merino, and I. Martin-Gullon, "Augmented fatigue performance and constant life diagrams of hierarchical carbon fiber/nanofiber epoxy composites," *Compos. Sci. Technol.*, vol. 72, no. 3, pp. 446–452, 2012.

[34] I. Guseva Canu *et al.*, "Human exposure to carbon-based fibrous nanomaterials: A review," *Int. J. Hyg. Environ. Health*, vol. 219, no. 2, pp. 166–175, 2016.

[35] S. van der Zwaag, *Self Healing Materials An Alternative Approach to 20 Centuries*. Springer, 2007.

[36] S. J. Garcia, "Effect of polymer architecture on the intrinsic self-healing character of polymers," *Eur. Polym. J.*, vol. 53, no. 1, pp. 118–125, 2014.

[37] N. Zhong and W. Post, "Self-repair of structural and functional composites with intrinsically self-healing polymer matrices: A review," *Compos. Part A Appl. Sci. Manuf.*, vol. 69, pp. 226–239, 2015.

[38] X. Chen, "A Thermally Re-mendable Cross-Linked Polymeric Material," *Science (80-.).*, vol. 295, no. 5560, pp. 1698–1702, 2002.

[39] E. B. Murphy, E. Bolanos, C. Schaffner-Hamann, F. Wudl, S. R. Nutt, and M. L. Auad, "Synthesis and characterization of a single-component thermally remendable polymer network: Staudinger and stille revisited," *Macromolecules*, vol. 41, no. 14, pp. 5203–5209, 2008.

[40] E. Amendola, S. Dello Iacono, A. Pastore, M. Curcio, M. Giordano, and A. Iadonisi, "Epoxy Thermosets with Self-Healing Ability," *J. Mater. Sci. Chem. Eng.*, no. 3, pp. 162–167, 2015.

[41] D. B. V. Parker, "Self-healing systems based on disulfide-thiol exchange reactions," *Polym. Chem.*, 2013.

[42] U. Lafont, H. Van Zeijl, and S. Van Der Zwaag, "Influence of cross-linkers on the cohesive and adhesive self-healing ability of polysulfide-based thermosets," *ACS Appl. Mater. Interfaces*, vol. 4, no. 11, pp. 6280–6288, 2012.

[43] J. Canadell, H. Goossens, and B. Klumperman, "Self-healing materials based on disulfide links," *Macromolecules*, vol. 44, no. 8, pp. 2536–2541, 2011.

[44] F. Herbst, D. Döhler, P. Michael, and W. H. Binder, "Self-Healing Polymers via Supramolecular forces.pdf," pp. 203–220.

[45] P. Cordier, F. Tournilhac, C. Soulié-Ziakovic, and L. Leibler, "Self-healing and thermoreversible rubber from supramolecular assembly.," *Nature*, vol. 451, no. 7181, pp. 977–80, 2008.

[46] R. P. Sijbesma *et al.*, "Reversible polymers formed from self-complementary monomers using quadruple hydrogen bonding.," *Science*, vol. 278, no. 5343, pp. 1601–4, 1997.

[47] K. Gosh, *Self-healing Materials*. Wiley-vch, 2009.

[48] D. Y. Wu, S. Meure, and D. Solomon, "Self-healing polymeric materials: A review of recent developments," *Prog. Polym. Sci.*, vol. 33, no. 5, pp. 479–522, 2008.

[49] T. J. Swait *et al.*, "Smart composite materials for self-sensing and self-healing," *Plast. Rubber Compos.*, vol. 41, no. 4–5, pp. 215–224, 2013.

[50] S. R. White *et al.*, "Autonomic healing of polymer composites," *Nature*, vol. 409, no. 6822, pp. 794–797, 2001.

[51] E. N. Brown, S. R. White, and N. R. Sottos, "Retardation and repair of fatigue cracks in a microcapsule toughened epoxy composite - Part II: In situ self-healing," *Compos. Sci. Technol.*, vol. 65, no. 15–16 SPEC. ISS., pp. 2474–2480, 2005.

[52] M. R. Kessler, N. R. Sottos, and S. R. White, "Self-healing structural composite materials," *Compos. Part A Appl. Sci. Manuf.*, vol. 34, no. 8, pp. 743–753, 2003.

[53] A. J. Patel, N. R. Sottos, E. D. Wetzel, and S. R. White, "Autonomic healing of low-velocity impact damage in fiber-reinforced composites," *Compos. Part A Appl. Sci. Manuf.*, vol. 41, no. 3, pp. 360–368, 2010.

[54] C. M. Dry and N. R. Sottos, "Passive smart self-repair in polymer matrix composite materials," *1993 North*

References

Am. Conf. Smart Struct. Mater., vol. 1916, pp. 438–444, 1993.

[55] C. Dry, "Procedures Developed for Self-Repair of Polymeric Matrix Composite Materials," *Compos. Struct.*, vol. 35, pp. 263–269, 1996.

[56] J. W. C. Pang and I. P. Bond, "A hollow fibre reinforced polymer composite encompassing self-healing and enhanced damage visibility," *Compos. Sci. Technol.*, vol. 65, no. 11–12, pp. 1791–1799, 2005.

[57] R. S. Trask, G. J. Williams, and I. P. Bond, "Bioinspired self-healing of advanced composite structures using hollow glass fibres.," *J. R. Soc. Interface*, vol. 4, no. 13, pp. 363–71, 2007.

[58] R. S. Trask and I. P. Bond, "Biomimetic self-healing of advanced composite structures using hollow glass fibres," *Smart Mater. Struct.*, vol. 15, no. 3, pp. 704–710, 2006.

[59] R. S. Trask, C. J. Norris, and I. P. Bond, "Stimuli-triggered self-healing functionality in advanced fibre-reinforced composites," *J. Intell. Mater. Syst. Struct.*, vol. 25, no. 1, pp. 87–97, 2014.

[60] A. M. Coppola, P. R. Thakre, N. R. Sottos, and S. R. White, "Tensile properties and damage evolution in vascular 3D woven glass/epoxy composites," *Compos. Part A Appl. Sci. Manuf.*, vol. 59, pp. 9–17, 2014.

[61] J. Doshi and D. H. Reneker, "Electrospinning process and applications of electrospun fibers," *J. Electrostat.*, vol. 35, pp. 151–161, 1995.

[62] J. F. Cooley, "Apparatus for electrically dispersing fluids," US692631 A, 1902.

[63] W. J. Morton, "Method of dispersing fluids," US 705691 A, 1902.

[64] J. Gatford, "A diagram of the electrospinning process showing the onset of instability," 2008. .

[65] UNIBO, "RGE Research group on electrospinning," 2010. .

[66] L. Zhenyu and C. Wang, *One-Dimensional Nanostructures Electrospinning Technique and Unique Nanofibers*. 2013.

[67] C. Zhang, X. Yuan, L. Wu, Y. Han, and J. Sheng, "Study on morphology of electrospun poly(vinyl alcohol) mats," *Eur. Polym. J.*, vol. 41, no. 3, pp. 423–432, 2005.

[68] A. Koski, K. Yim, and S. Shivkumar, "Effect of molecular weight on fibrous PVA produced by electrospinning," *Mater. Lett.*, vol. 58, no. 3–4, pp. 493–497, 2004.

[69] L. Zhenyu and C. Wang, "Effects of Working Parameters on Electrospinning," in *One-Dimensional nanostructures*, Springer Berlin Heidelberg, 2013, pp. 15–28.

[70] A. Arinstein, M. Burman, O. Gendelman, and E. Zussman, "Effect of supramolecular structure on polymer nanofibre elasticity," *Nat. Nanotechnol.*, vol. 2, no. 1, pp. 59–62, 2007.

[71] Y. A. Dzenis, "Delamination resistant composites prepered by small fiber reninforcement at ply interfaces," WO 99/62705, 1999.

[72] L. Liu, Z. M. Huang, C. L. He, and X. J. Han, "Mechanical performance of laminated composites incorporated with nanofibrous membranes," *Mater. Sci. Eng. A*, vol. 435–436, pp. 309–317, 2006.

[73] A. Zucchelli, M. L. Focarete, C. Gualandi, and S. Ramakrishna, "Electrospun nanofibers for enhancing structural performance of composite materials," *Polym. Adv. Technol.*, vol. 22, no. 3, pp. 339–349, 2011.

[74] R. H. A. G. Schoenmaker BD, Heijden SV, Moorkens S, "Effect of nanofibers on the curing characteristics of an epoxy matrix," *Compos. Sci. Technol.*, vol. 79, pp. 35–41, 2013.

[75] M. Di Filippo, S. Alessi, G. Pitarresi, M. A. Sabatino, A. Zucchelli, and C. Dispenza, "Hydrothermal aging of carbon reinforced epoxy laminates with nanofibrous mats as toughening interlayers," *Polym. Degrad. Stab.*, vol. 126, pp. 188–195, 2016.

[76] B. De Schoenmaker, S. Van der Heijden, S. Moorkens, H. Rahier, G. Van Assche, and K. De Clerck, "Effect of nanofibers on the curing charecteristics of an epoxy matrix," *Compos. Sci. Technol.*, vol. 79, pp. 35–41, 2013.

[77] K. N. Shivakumar and R. Panduranga, "Interleaved polymer matrix composites - A review," *Collect. Tech. Pap. - AIAA/ASME/ASCE/AHS/ASC Struct. Struct. Dyn. Mater. Conf.*, no. April, pp. 1–13, 2013.

[78] R. Palazzetti, "Flexural behavior of carbon and glass fiber composite laminates reinforced with Nylon 6,6 electrospun nanofibers," *J. Compos. Mater.*, vol. 49, no. 27, pp. 3407–3413, 2015.

[79] H. Saghafi, R. Palazzetti, A. Zucchelli, and G. Minak, "Influence of electrospun nanofibers on the interlaminar properties of unidirectional epoxy resin/glass fiber composite laminates," *J. Reinf. Plast. Compos.*, vol. 34, no. 11, pp. 907–914, 2015.

[80] F. Moroni, R. Palazzetti, A. Zucchelli, and A. Pirondi, "A numerical investigation on the interlaminar strength of nanomodified composite interfaces," *Compos. Part B Eng.*, vol. 55, pp. 635–641, 2013.

[81] H. Saghafi, R. Palazzetti, A. Zucchelli, and G. Minak, "Impact response of glass/epoxy laminate interleaved with nanofibrous mats," *Eng. Solid Mech.*, vol. 1, no. SEPTEMBER, pp. 85–90, 2013.

[82] X. F. Wu and A. L. Yarin, "Recent progress in interfacial toughening and damage self-healing of polymer composites based on electrospun and solution-blown nanofibers: An overview," *J. Appl. Polym. Sci.*, vol. 130, no. 4, pp. 2225–2237, 2013.

References

[83] B. De Schoenmaker, S. Van Der Heijden, I. De Baere, W. Van Paepegem, and K. De Clerck, "Effect of electrospun polyamide 6 nanofibres on the mechanical properties of a glass fibre/epoxy composite," *Polym. Test.*, vol. 32, no. 8, pp. 1495–1501, 2013.

[84] V. Koissin, L. L. Warnet, and R. Akkerman, "Delamination in carbon-fibre composites improved with in situ grown nanofibres," *Eng. Fract. Mech.*, vol. 101, pp. 140–148, 2013.

[85] K. Molnár, E. Košťáková, and L. Mészáros, "The effect of needleless electrospun nanofibrous interleaves on mechanical properties of carbon fabrics/epoxy laminates," *Express Polym. Lett.*, vol. 8, no. 1, pp. 62–72, 2014.

[86] L. Daelemans, S. van der Heijden, I. De Baere, H. Rahier, W. Van Paepegem, and K. De Clerck, "Nanofibre bridging as a toughening mechanism in carbon/epoxy composite laminates interleaved with electrospun polyamide nanofibrous veils," *Compos. Sci. Technol.*, vol. 117, pp. 244–256, 2015.

[87] "ASTM D5528. Standard Test Method for Mode I Interlaminar Fracture Toughness of Unidirectional Fiber-Reinforced Polymer Matrix Composites," *Am. Soc. Test. Mater.*, no. Mode I, pp. 1–13, 2001.

[88] "Protocol No 2 for interlaminar fracture toughness testing of composites: Mode II," 1993.

[89] ASTM, "ASTM D5528 Standard Test Method for Mode I Interlaminar Fracture Toughness of Unidirectional Fiber-Reinforced Polymer Matrix Composites," *Am. Soc. Test. Mater.*, no. Mode I, pp. 1–13, 2014.

[90] G. Li *et al.*, "Inhomogeneous toughening of carbon fiber/epoxy composite using electrospun polysulfone nanofibrous membranes by in situ phase separation," *Compos. Sci. Technol.*, vol. 68, no. 3–4, pp. 987–994, 2008.

[91] K. Magniez, T. Chaffraix, and B. Fox, "Toughening of a carbon-fibre composite using electrospun poly(hydroxyether of bisphenol A) nanofibrous membranes through inverse phase separation and inter-domain etherification," *Materials (Basel).*, vol. 4, no. 11, pp. 1967–1984, 2011.

[92] H. Saghafi, A. Zucchelli, R. Palazzetti, and G. Minak, "The effect of interleaved composite nanofibrous mats on delamination behavior of polymeric composite materials," *Compos. Struct.*, vol. 109, no. 1, pp. 41–47, 2014.

[93] R. Palazzetti, A. Zucchelli, and I. Trendafilova, "The self-reinforcing effect of Nylon 6,6 nano-fibres on CFRP laminates subjected to low velocity impact," *Compos. Struct.*, vol. 106, pp. 661–671, 2013.

[94] S. Alessi *et al.*, "Effects of Nylon 6,6 Nanofibrous Mats on Thermal Properties and Delamination Behavior of High Performance CFRP Laminates," *Polim. Compos.*, 2015.

[95] J. Zhang, T. Yang, T. Lin, and C. H. Wang, "Phase morphology of nanofibre interlayers: Critical factor for toughening carbon/epoxy composites," *Compos. Sci. Technol.*, vol. 72, no. 2, pp. 256–262, 2012.

[96] K. Magniez, C. De Lavigne, and B. L. Fox, "The effects of molecular weight and polymorphism on the fracture and thermo-mechanical properties of a carbon-fibre composite modified by electrospun poly(vinylidene fluoride) membranes," *Polymer (Guildf).*, vol. 51, no. 12, pp. 2585–2596, 2010.

[97] J. K. Kim and R. E. Robertson, "Toughening of thermoset polymers by rigid crystalline particles," *J. Mater. Sci.*, vol. 27, no. 1, pp. 161–174, 1992.

[98] M. Arai, J. I. Hirokawa, Y. Hanamura, H. Ito, M. Hojo, and M. Quaresimin, "Characteristic of mode I fatigue crack propagation of CFRP laminates toughened with CNF interlayer," *Compos. Part B Eng.*, vol. 65, pp. 26–33, 2014.

[99] Y. Zhou, S. Jeelani, and T. Lacy, "Experimental study on the mechanical behavior of carbon/epoxy composites with a carbon nanofiber-modified matrix," *J. Compos. Mater.*, vol. 48, no. 29, pp. 3659–3672, 2014.

[100] K. N. Shivakumar, S. Lingaiah, H. Chen, P. Akangah, G. Swaminathan, and L. Russell, "Polymer Nanofabric Interleaved Composite Laminates," *AIAA J.*, vol. 47, no. 7, pp. 1723–1729, 2009.

[101] ASTM, "ASTM D 6115 Standard test method for mode I fatigue delamination growth onset of unidirectional fibre-reinforced polymer matrix composites," *Am. Soc. Test. Mater.*, vol. 15.03, no. Reapproved, pp. 1–6, 2001.

[102] ASTM, "ASTM E647-15 Standard Test Method for Measurement of Fatigue Crack Growth Rates," vol. 3, pp. 1–43, 1999.

[103] K. N. Shivakumar, H. Chen, F. Abali, D. Le, and C. Davis, "A total fatigue life model for mode i delaminated composite laminates," *Int. J. Fatigue*, vol. 28, no. 1, pp. 33–42, 2006.

[104] M. Olave, I. Vara, H. Usabiaga, L. Aretxabaleta, S. V. Lomov, and D. Vandepitte, "Mode I fatigue fracture toughness of woven laminates: Nesting effect," *Compos. Struct.*, vol. 133, pp. 226–234, 2015.

[105] J. A. Pascoe, R. C. Alderliesten, and R. Benedictus, "Methods for the prediction of fatigue delamination growth in composites and adhesive bonds - A critical review," *Eng. Fract. Mech.*, vol. 112–113, pp. 72–96, 2013.

104

References

[106] N. Sato, M. Hojo, and M. Nishikawa, "Intralaminar fatigue crack growth properties of conventional and interlayer toughened CFRP laminate under mode i loading," *Compos. Part A Appl. Sci. Manuf.*, vol. 68, pp. 202–211, 2015.

[107] K. Kageyama, K. Kimpara, I. Osawa, and M. Hojo, "Damage tolerance estimation of advanced composite materials (1st report: Study on interlaminar fracture toughness test)," *J. Soc. Nav. Archit. Japan*, vol. 168, pp. 497–506, 1990.

[108] T. K. O. Brien, "Towards a Delamination Fatigue Methodology for Composite Materials," *16th Int. Conf. Compos. Mater.*, pp. 1–5, 2007.

[109] ASTM, "ASTM E 739 DStandard Practice for Statistical Analysis of Linear or Linearized Stress-Life and Strain-Life Fatigue Data," *Annu. B. ASTM Stand.*, vol. i, no. Reapproved, pp. 1–7, 2012.

[110] P. Paris, M. Gomez, and W. Anderson, "A rational analytic theory of fatigue," 1961.

[111] J. Zhang, T. Lin, and X. Wang, "Electrospun nanofibre toughened carbon/epoxy composites: Effects of polyetherketone cardo (PEK-C) nanofibre diameter and interlayer thickness," *Compos. Sci. Technol.*, vol. 70, no. 11, pp. 1660–1666, 2010.

[112] C. A. J. R. Vermeeren, "An Historic Overview of the Development of Fibre Metal Laminates," *Appl. Compos. Mater.*, vol. 10, no. 4–5, pp. 189–205, 2003.

[113] A. Vlot and J. W. Gunnink, *Fibre Metal Laminates: An Introduction*. Dordrecht, Netherland: Kluwer Academic Publishers, 2001.

[114] A. Vlot, L. B. Vogelesang, and T. J. De Vries, "Towards application of fibre metal laminates in large aircraft," *Aircr. Eng. Aerosp. Technol.*, vol. 71, pp. 558–570, 1999.

[115] J. Remmers, "Discontinuities in materials and structures: a unifying computational approach," Delft University of Technology, 2008.

[116] M. Sadighi, R. C. Alderliesten, and R. Benedictus, "Impact resistance of fiber-metal laminates: A review," *International Journal of Impact Engineering*, vol. 49. Elsevier Ltd, pp. 77–90, Nov-2012.

[117] A. Vlot, "Impact loading on fibre metal laminates," *intenational J. impact Eng.*, vol. 18, no. 3, pp. 291–307, 1996.

[118] A. Vlot, E. Kroon, and G. La Rocca, "Impact Response of Fiber Metal Laminates," *Key Eng. Mater.*, vol. 141–143, pp. 235–276, 1998.

[119] A. S. Yaghoubi, Y. Liu, and B. Liaw, "Stacking Sequence and Geometrical Effects on Low-Velocity Impact Behaviors of GLARE 5 (3/2) Fiber-Metal Laminates," *J. Thermoplast. Compos. Mater.*, vol. 25, no. 2, pp. 223–247, Jul. 2011.

[120] J. F. Laliberté, P. V. Straznicky, and C. Poon, "Impact Damage in Fiber Metal Laminates, Part 1: Experiment," *AIAA J.*, vol. 43, no. 11, pp. 2445–2453, 2005.

[121] H. Zarei, M. Fallah, G. Minak, H. Bisadi, and A. Daneshmehr, "Low velocity impact analysis of Fiber Metal Laminates (FMLs) in thermal environments with various boundary conditions," *Compos. Struct.*, vol. 149, pp. 170–183, 2016.

[122] H. Zarei, M. Sadighi, and G. Minak, "Ballistic analysis of fiber metal laminates impacted by flat and conical impactors," *Compos. Struct.*, vol. 161, pp. 65–72, 2017.

[123] F. D. Morinière, R. C. Alderliesten, and R. Benedictus, "Modelling of impact damage and dynamics in fibre-metal laminates – A review," *Int. J. Impact Eng.*, vol. 67, pp. 27–38, May 2014.

[124] G. B. Chai and P. Manikandan, "Low velocity impact response of fibre-metal laminates – A review," *Compos. Struct.*, vol. 107, pp. 363–381, Jan. 2014.

[125] Y. Liu and B. Liaw, "Effects of Constituents and Lay-up Configuration on Drop-Weight Tests of Fiber-Metal Laminates," *Appl. Compos. Mater.*, vol. 17, no. 1, pp. 43–62, Dec. 2009.

[126] H. Zhang, S. W. Gn, J. An, Y. Xiang, and J. L. Yang, "Impact Behaviour of GLAREs with MWCNT Modified Epoxy Resins," *Exp. Mech.*, vol. 54, no. 1, pp. 83–93, 2014.

[127] R. Palazzetti *et al.*, "Influence of electrospun Nylon 6,6 nanofibrous mats on the interlaminar properties of Gr-epoxy composite laminates," *Compos. Struct.*, vol. 94, no. 2, pp. 571–579, 2012.

[128] R. Palazzetti, A. Zucchelli, and I. Trendafilova, "The self-reinforcing effect of Nylon 6,6 nano-fibres on CFRP laminates subjected to low velocity impact," *Compos. Struct.*, vol. 106, pp. 661–671, 2013.

[129] H. Saghafi, T. Brugo, G. Minak, and A. Zucchelli, "The effect of PVDF nanofibers on mode-I fracture toughness of composite materials," *Compos. Part B Eng.*, vol. 72, pp. 213–216, 2015.

[130] H. Saghafi, A. Zucchelli, R. Palazzetti, and G. Minak, "The effect of interleaved composite nanofibrous mats on delamination behavior of polymeric composite materials," *Compos. Struct.*, vol. 109, no. 1, pp. 41–47, 2014.

[131] P. Akangah, S. Lingaiah, and K. N. Shivakumar, "Effect of Nylon-66 nano-fiber interleaving on impact damage resistance of epoxy/carbon fiber composite laminates," *Compos. Struct.*, vol. 92, no. 6, pp.

References

1432–1439, 2010.

[132] K. Shivakumar, S. Lingaiah, H. Chen, P. Akangah, G. Swaminathan, and L. Russell, "Polymer Nanofabric Interleaved Composite Laminates," *AIAA J.*, vol. 47, no. 7, pp. 1723–1729, 2009.

[133] "ASTM D2651-Standard Guide for Preparation of Metal Surfaces for Adhesive Bonding 1," 2012.

[134] "ASTM D7136-Standard Test Method for Measuring the Damage Resistance of a Fiber-Reinforced Polymer Matrix Composite to a Drop-Weight Impact Event," 2005.

[135] E. Poodts, D. Ghelli, T. Brugo, R. Panciroli, and G. Minak, "Experimental characterization of a fiber metal laminate for underwater applications," *Compos. Struct.*, vol. 129, pp. 36–46, 2015.

[136] K. Iqbal, S.-U. Khan, A. Munir, and J.-K. Kim, "Impact damage resistance of CFRP with nanoclay-filled epoxy matrix," *Compos. Sci. Technol.*, vol. 69, no. 11–12, pp. 1949–1957, Sep. 2009.

[137] T. Pärnänen, A. Vänttinen, M. Kanerva, J. Jokinen, and O. Saarela, "The Effects of Debonding on the Low-Velocity Impact Response of Steel-CFRP Fibre Metal Laminates," *Appl. Compos. Mater.*, 2016.

[138] S. Abrate, *Impact on Composite Structures*. Cambridge University press, 1998.

[139] M. Hoo Fatt, C. Lin, D. M. Revilock, and D. a. Hopkins, "Ballistic impact of GLARE™ fiber–metal laminates," *Compos. Struct.*, vol. 61, no. 1–2, pp. 73–88, Jul. 2003.

[140] J. H. Park and P. V. Braun, "Coaxial electrospinning of self-healing coatings," *Adv. Mater.*, vol. 22, no. 4, pp. 496–499, 2010.

[141] M. W. Lee, S. An, C. Lee, M. Liou, A. L. Yarin, and S. S. Yoon, "Hybrid Self-Healing Matrix Using Core – Shell Nano fi bers and Capsuleless Microdroplets," *Appl. Mater. Interfaces*, vol. 6, pp. 10461–10468, 2014.

[142] M. W. Lee, S. An, C. Lee, M. Liou, A. L. Yarin, and S. S. Yoon, "Self-healing transparent core–shell nanofiber coatings for anti-corrosive protection," *J. Mater. Chem. A*, vol. 2, no. 19, pp. 7045–7053, 2014.

[143] T. Q. Doan, L. S. Leslie, S. Y. Kim, R. Bhargava, S. R. White, and N. R. Sottos, "Characterization of core-shell microstructure and self-healing performance of electrospun fiber coatings," *Polym. (United Kingdom)*, vol. 107, pp. 263–272, 2016.

[144] M. W. Lee, S. S. Yoon, and A. L. Yarin, "Solution-Blown Core-Shell Self-Healing Nano- and Microfibers," *ACS Appl. Mater. Interfaces*, vol. 8, no. 7, pp. 4955–4962, 2016.

[145] M. W. Lee, S. An, H. S. Jo, S. S. Yoon, and A. L. Yarin, "Self-healing Nanofiber-Reinforced Polymer Composites. 2. Delamination/Debonding and Adhesive and Cohesive Properties," *ACS Appl. Mater. Interfaces*, vol. 7, no. 35, pp. 19555–19561, 2015.

[146] T. J. Mitchell and M. W. Keller, "Coaxial electrospun encapsulation of epoxy for use in self-healing materials," *Polym. Int.*, vol. 62, no. 6, pp. 860–866, 2013.

[147] J. S. Monfared Zanjani, B. S. Okan, I. Letofsky-Papst, Y. Menceloglu, and M. Yildiz, "Repeated self-healing of nano and micro scale cracks in epoxy based composites by tri-axial electrospun fibers including different healing agents," *RSC Adv.*, vol. 5, no. 89, pp. 73133–73145, 2015.

[148] M. W. Lee, S. An, H. S. Jo, S. S. Yoon, and A. L. Yarin, "Self-Healing Nanofiber-Reinforced Polymer Composites. 1. Tensile Testing and Recovery of Mechanical Properties," *ACS Appl. Mater. Interfaces*, vol. 7, no. 35, pp. 19546–19554, 2015.

[149] M. W. Lee, S. Sett, S. S. Yoon, and A. L. Yarin, "Fatigue of Self-Healing Nanofiber-based Composites: Static Test and Subcritical Crack Propagation," *ACS Appl. Mater. Interfaces*, vol. 8, no. 28, pp. 18462–18470, 2016.

[150] M. W. Lee, S. Sett, S. S. Yoon, and A. L. Yarin, "Self-healing of nanofiber-based composites in the course of stretching," *Polym. (United Kingdom)*, vol. 103, pp. 180–188, 2016.

[151] R. E. Neisiany *et al.*, "Encapsulation of epoxy and amine curing agent in PAN nanofibers by coaxial electrospinning for self-healing purposes," *RSC Adv.*, vol. 6, no. 74, pp. 70056–70063, 2016.

[152] A.-C. Bijlard *et al.*, "Dual-compartment nanofibres: separation of two highly reactive components in close vicinity," *RSC Adv.*, vol. 5, no. 118, pp. 97477–97484, 2015.

[153] X. F. Wu *et al.*, "Electrospinning core-shell nanofibers for interfacial toughening and self-healing of carbon-fiber/epoxy composites," *J. Appl. Polym. Sci.*, vol. 129, no. 3, pp. 1383–1393, 2013.

[154] Z. Sun, E. Zussman, A. L. Yarin, J. H. Wendorff, and A. Greiner, "Compound Core-Shell Polymer Nanofibers by Co-Electrospinning," *Adv. Mater.*, vol. 15, no. 22, pp. 1929–1932, 2003.

[155] L. Fengyu, Y. Zhao, and S. Yanlin, "Core-Shell Nanofibers: Nano Channel and Capsule by Coaxial Electrospinning," in *Nanofibers*, INTECH, 2010.

[156] F. Elahi, W. Lu, G. Guoping, and F. Khan, "Core-shell Fibers for Biomedical Applications-A Review," *Bioeng. Biomed. Sci. J.*, vol. 3, no. 1, pp. 1–14, 2013.

[157] J. E. Díaz, A. Barrero, M. Márquez, and I. G. Loscertales, "Controlled encapsulation of hydrophobic liquids in hydrophilic polymer nanofibers by co-electrospinning," *Adv. Funct. Mater.*, vol. 16, no. 16, pp. 2110–

106

References

2116, 2006.

[158] T. J. Longson, R. Bhowmick, C. Gu, and B. A. Cruden, "Core-shell interactions in coaxial electrospinning and impact on electrospun multiwall carbon nanotube core, poly(methyl methacrylate) shell fibers," *J. Phys. Chem. C*, vol. 115, no. 26, pp. 12742–12750, 2011.

[159] D. Li and Y. Xia, "Direct fabrication of composite and ceramic hollow nanofibers by electrospinning," *Nano Lett.*, vol. 4, no. 5, pp. 933–938, 2004.

[160] Z. Kurban *et al.*, "A solution selection model for coaxial electrospinning and its application to nanostructured hydrogen storage materials," *J. Phys. Chem. C*, vol. 114, no. 49, pp. 21201–21213, 2010.

[161] H. J. Yu, S. V. Fridrikh, and G. C. Rutledge, "Production of submicrometer diameter fibers by two-fluid electrospiiming," *Adv. Mater.*, vol. 16, no. 17, pp. 1562–1566, 2004.

[162] S. K. Tiwari and S. S. Venkatraman, "Importance of viscosity parameters in electrospinning: Of monolithic and core-shell fibers," *Mater. Sci. Eng. C*, vol. 32, no. 5, pp. 1037–1042, 2012.

[163] D. Li, A. Babel, S. A. Jenekhe, and Y. Xia, "Nanofibers of conjugated polymers prepared by electrospinning with a two-capillary spinneret," *Adv. Mater.*, vol. 16, no. 22, pp. 2062–2066, 2004.

[164] Y. Yang, Z. Jia, Q. Li, and Z. Guan, "Experimental investigation of the governing parameters in the electrospinning of polyethylene oxide solution," *IEEE Trans. Dielectr. Electr. Insul.*, vol. 13, no. 3, pp. 580–584, 2006.

[165] a. K. Moghe and B. S. Gupta, "Co-axial Electrospinning for Nanofiber Structures: Preparation and Applications," *Polym. Rev.*, vol. 48, no. 2, pp. 353–377, 2008.

[166] C. M. Hansen, *HANSEN SOLUBILITY PARAMETERS A User's Handbook*. CRC Press, 1998.

[167] D. W. Van Krevelen and K. T. Nijenhuis, *Properties of Polymers*. 2009.

[168] E. M. Petrie, *Epoxy Adhesive formulations*. McGraw-Hill, 2006.

[169] M. L. Hallensleben, "Polyvinyl Compounds, Others," *Ullmann's Encycl. Ind. Chem.*, vol. 29, p. 6.5-621, 2012.

[170] J. Zeng, H. Hou, J. H. Wendorff, and A. Greiner, "Electrospun poly (vinyl alcohol)/ poly (acrylic acid) fibres with excellent water-stability," no. 78, pp. 1–8, 2004.

[171] J.-C. Park *et al.*, "Electrospun poly(vinyl alcohol) nanofibers: effects of degree of hydrolysis and enhanced water stability," *Polym. J.*, vol. 42, no. 3, pp. 273–276, 2010.

Summary

Fiber reinforce plastics laminates are a well-known class of composite materials obtained by combining high stiff and strong fibers with a weaker polymeric matrix, whose resulting mechanical and physical properties are designed to be superior to those of their individual constituents. The most performing ones are made by stacking plies with long fibers, disposed in different directions as a function of their application.

They present important advantages compared to conventional monolithic materials, mainly because for equal stiffness and strength they have a weight up to four times lower. However, due to the ply-by-ply nature of the composite laminates, the susceptibility to delamination along interlaminar planes is an intrinsic and severe problem of these materials, whose propagation bring the structure to rapid catastrophic failure.

The aim of this thesis was to increase the service life of composite laminates, by exploring two different approaches:

- prevent the delamination by toughening the interlayer through nanofiber interleaving
- confer to the material the self-repair capability through core-shell nanofibers filled with the healing agent

In *Chapter 1* a special manufacturing process for the integration of the nanofibrous mat in the composite laminate was developed, by tailoring the lamination technique and the curing cycle. By interleaving the nanofibrous mat with the developed process, the mode I interlaminar fracture toughness of woven laminates was enhanced up to 250%, compared to 10-20% of the standard method.

Once the interleaving process was optimized, in *Chapter 2* the effect of thickness of Nylon 66 nanofibrous mat on Modes I–II fracture mechanics of UD and woven composite laminates was investigated. The experimental results showed a significant improvement when nanofibers were employed, under both mode I and II loading conditions for both UD and woven reinforcements architectures. However, in general better results were found for woven laminates loaded in mode I. Micrographs analysis showed that, the crack in nanomodified samples is forced to break a larger amount of matrix and microfiber compared to virgin samples, requiring so higher energy to propagate. Eventually, the micrographs explained the mechanical results, suggesting a strong interaction between the nature of the macro reinforcement (UD and woven) and the thickness of the nano one. In general, the nano

reinforcement increases the fracture toughness at the initiation for all the configurations, while the propagation stage is significantly dependent on the amount of the nano-reinforcement and on the nature of the macro one.

In *Chapter 3*, a different polymer, polyvinylidene fluoride (PVDF), was employed as nanofibrous reinforcement. Contrary to the results reported in literature, was proved that PVDF nanofibers, if properly integrated, can enhanced the mode I fracture toughness of woven interleaved composite laminates. However, despite the different mechanical properties of PVDF, compared to Nylon 66 and the different mode of integration with the matrix, the results of the mechanical test were quite similar. Suggesting that the key parameter for fracture toughening by nanofiber interleaving is not the employed material but the thickness of the nano-mat; which it is strongly dependent on the architecture of the macro reinforcement.

The fatigue behavior to the onset of the delamination and the crack growth rate for woven laminates interleaved with Nylon 66 nanofibers was investigated in *Chapter 4,* for the first time in literature. Results show that at fatigue, the presence of the nanofibers enhances the fracture toughness at the onset of the delamination, increasing the mode I threshold energy release rate (evaluated at 10^6 cycles) of 90%. Crack growth ratio tests revealed that nano reinforced laminates can sustain higher loads for same propagation speed (G_{imax} 96% higher for N at $5*10^5$ mm/cycle). Fatigue tests also showed that for values of G_{max} in the considered range, the crack in a nanomodified interface propagates several times slower than in a virgin one (from 27 to 36 times slower). SEM images showed that the nanofibers hold the matrix together whilst forcing the crack to move away from the nanomodified interface.

Glass Laminate Aluminum Reinforced Epoxy (GLARE) are a special class of hybrid composite materials consisting of alternating aluminum sheets bonded to glass-epoxy prepreg layers. They are known for the superior impact resistance compared to conventional composite laminates. However according to literature, their impact performances are limited by the interlaminar fracture toughness which causes delamination and debonding. Hence, in *Chapter 5*, GLARE aluminum – glass/epoxy interfaces were interleaved with electrospun Nylon 66 nanofibrous mats. Despite nano reinforcement did not have any noticeable effect on the dynamic impact response of GLARE as the absorbed energy, the micrographs analysis of the impacted zone revealed a completely different behavior. Nylon 6,6, by increasing the adhesion between the aluminum sheet and the glass/epoxy, has reduced the delamination area of 42, 53, 63 and 62 % at impact energy levels of 6, 12, 18 and 32 J, respectively.

In Chapter 6, the research activity was dedicated to exploring the possibility of increasing the service life of composite materials by giving them the ability of self-repair in the event of local delamination. An extrinsic self-healing system based on core-shell nanofibers filled with a two-component liquid epoxy system was developed in *Chapter 6*. The selection of the polymers and the solvents system, suitable for the encapsulation of the healing agent by co-electrospinning technique, was assisted by a homemade program based on Hansen solubility

parameters. Different polymers for the shell were investigated and polyvinyl alcohol (PVA) was found to be suitable for the encapsulation and storing of the high reactive healing agent. The self-healing potential of the developed system was proved by SEM observation of the healing agent release as result of breaking of the core-shell. The chemical reactivity and stability of the stored healing agent was verified by thermal analysis (DSC) of the dual core-shell nanofibrous mat. No exothermic reaction was detected up to 150C if the core-shell nanofibers were untouched, proving so the thermal stability of the self-healing system. While as result of a mechanical induced damage on the core-shell, the healing agent was released and an exothermic reaction, linked to the crosslinking of the epoxy system, was detected.

Tommaso Maria Brugo, 2017

Acknowledgements

I would like to express my sincere gratitude to all those, who have given me the possibility to finalize the works of this thesis.

Firstly, I would like to express my gratitude to my advisor Professor Andrea Zucchelli for making me discover the magical world of science and giving me the opportunity and lots of freedom to fulfill this PhD project. I would like to thanks professor Giangiacomo Minak for the continuous scientific stimulus and pragmatic advices on science and life. To both of them for their insightful comments and encouragement, but also for the hard tasks which have incited me to widen my research activity from various perspectives. I also thank Chiara Gualandi, my mentor on Electrospinning and chemistry.

I would like to express my gratitude to the NovAM research group at the Aerospace faculty of TU Delft for introducing me in the world of self-healing materials and especially Santiago Garcia Espallargas for the profitable meetings.

A big hug to all my colleagues for the useful discussions and for making funny the work. My deepest thanks go to Emmanuelle for encouraging me in the hard periods of this research project, but even more important for making my life beautiful. I have to thanks all my historical group of friends to remind me that there is not only the research in the life and keep me always young. A special thanks to my family who supported me in the decision to undertake this project and he gave me a solid background to face the life.

Tommaso Maria Brugo, 2017

List of Publications

_____ INTERNATIONAL JOURNALS_____

H. Zarei, T. M. Brugo, J. Belcari, H. Bisadi, G. Minak, A. Zucchelli. *Low Velocity Impact Damage Assessment of GLARE fiber-metal laminates Interleaved by Nylon 6,6 Nanofiber Mats*. Composite Structures, vol 167, pp. 123-131, (2017).

T. Brugo, G. Minak, A. Zucchelli, X.T. Yan, J. Belcari, H. Saghafi, R. Palazzetti. *Study on Mode I fatigue behaviour of Nylon 6,6 nanoreinforced CFRP laminates*. Composite Structures, vol. 164, pp. 51–57, (2017).

Živković, I., Fragassa, C., Pavlović, A., Brugo, T. *Influence of moisture absorption on the impact properties of flax, basalt and hybrid flax/basalt fiber reinforced green composites*. Composites Part B: Engineering vol. 111, pp. 148-164, (2017).

T. M. Brugo and R. Palazzetti. *The effect of thickness of Nylon 6,6 nanofibrous mat on Modes I–II fracture mechanics of UD and woven composite laminates*. Composite Structures. vol. 154, pp. 172-178, (2016).

H. Saghafi, S. Ghaffarian, T. M. Brugo, G. Minak, A. Zucchelli and H. A. Saghafi. *The effect of nanofibrous membrane thickness on fracture behaviour of modified composite laminates: A numerical and experimental study*. Composites Part B, vol. 101, pp. 116-123, (2016).

M Fotouhi, H Saghafi, T Brugo, G Minak, C Fragassa, A Zucchelli, M Ahmadi. *Effect of PVDF nanofibers on the fracture behavior of composite laminates for high-speed woodworking machines*. J Mechanical Engineering Science, 1–13 (2016).

T. Brugo, R. Palazzetti, S. Ciric-Kostic, X.T. Yan, G. Minak, A. Zucchelli. *Fracture mechanics of laser sintered cracked polyamide for a new method to induce cracks by additive manufacturing*. Polymer Testing 50 301-308 (2016).

H. Saghafi, T. Brugo, G. Minak, A. Zucchelli. *The effect of PVDF nanofibers on mode I fracture toughness of composite materials*. Composites: Part B: 72 213–216 (2015).

M. Palanca, T. M. Brugo, L. Cristofolini. *Use of the Digital Image Correlation to investigate the biomechanics of a vertebra*. Journal of Mechanics in Medicine and Biology: Vol. 15 No. 2 1540004 (2015).

E. Poodts, D. Ghelli, T. M. Brugo, R. Panciroli, G. Minak. *Experimental characterization of a fiber metal laminate for underwater applications*. Composite Structures: 129 36–46 (2015).

_____**CONFERENCES**_____

Mazzocchetti, L., D'angelo, E., Benelli, T., (...), Zucchelli, A., Giorgini, L. *Poly-m-aramid nanofiber mats: Production for application as structural modifiers in CFRP laminates*. AIP Conference Proceedings, 1736, 4949591, (2016).

F. Musiari, A. Pirondi, F. Moroni, G. Giuliese, J. Belcari, A. Zucchelli, T. M. Brugo, G. Minak, C. Ragazzini. *Feasibility study of adhesive bonding reinforcement by electrospun nanofibers*. Procedia Structural Integrity 2, pp. 112-119 (2016).

T. M. Brugo, G. Minak, A. Zucchelli, H. Saghafi, M Fotouhi. *An investigation on the fatigue based delamination of woven carbon-epoxy composite laminates reinforced with polyamide nanofibers*. Procedia Engineering: 109 65–72 (2015).

H. Saghafi, T. Brugo, G. Minak, and A. Zucchelli*. Improvement the impact damage resistance of composite materials by interleaving Polycaprolactone nanofibers.* Engineering Solid Mechanics 3 21-26 (2015)

H. Saghafi, T. Brugo, G. Minak, A. Zucchelli. The effect of pre-stress on impact response of concave & convex composite laminates. International Symposium on Dynamic Response and Failure of Composite Materials, Ischia, Italy (2014).

Magnani, T. M. Brugo. Experimental analysis of the variation of the clamping force in a bolted joint hybrid composite aluminum. 43° Conference Associazione Italiana per l'Analisi delle Sollecitazioni, Rimini, Italy (2014).

H. Saghafi, G. Minak, T. Brugo, A. Zucchelli. The influence of pre-stress and curvature on impact response of curved composite laminates. 16th European Conference on Composite Materials, ECCM, Seville, Spain (2014).

T. M. Brugo, R. Panciroli, C. Cerretani. Validation of a shape-sensing measurement system based on optical fiber bragg grating by comparison with measurements of digital image correlation. 43° Conference Associazione Italiana per l'Analisi delle Sollecitazioni, Rimini, Italy (2014).

F. Bovicelli, H. Saghafi, T. M. Brugo, J. Belcari, A. Zucchelli, G. Minak. *On consideration the mode I fracture response of CFRP composite interleaved by composite nanofibers*. Procedia Material Science V. 3, Page 1316–1321 (2014).

T. M. Brugo, G. A. Kokubu, R. Palazzetti E. Poodts. Long fiber composite coil spring for lightweight application. 13th Youth Symposium on Experimental Solid Mechanics, Prague, Czech Republic (2014).

T. M. Brugo, S. Ćirić-Kostić, E. Poodts, G. Minak. Fracture mechanics by selective laser sintering. 30th Danubia-Adria Symposium, Primosten, Croatia (2013).

T. M. Brugo, R. Panciroli, G. Minak. Study of the dynamic behavior of plates immersed in a fluid. 11th Youth Symposium on Experimental Solid Mechanics, Brasov, Romania (2012).

T. M. Brugo, R. Panciroli. Study of the dynamic behavior of plates immersed in a fluid. 41° Conference Associazione Italiana per l'Analisi delle Sollecitazioni, Vicenza, Italy (2012).